U.PORTO
FACULDADE DE CIÊNCIAS
UNIVERSIDADE DO PORTO

universidade de aveiro

FACULDADE DE CIÊNCIAS E TECNOLOGIA
UNIVERSIDADE NOVA DE LISBOA

Carbon materials for catalysis and perovskite-based solar cells

Bruno Miguel Magalhães Jarrais

PhD thesis submitted to
Faculdade de Ciências da Universidade do Porto,
Departamento de Química da Universidade de Aveiro,
Faculdade de Ciências e Tecnologia da Universidade de Lisboa,
Chemistry

2017

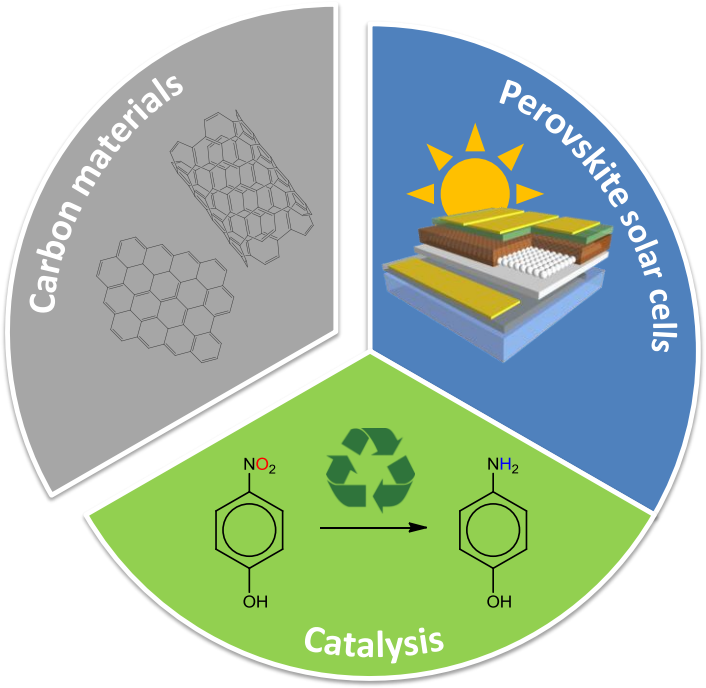

Carbon materials for catalysis and perovskite-based solar cells

Bruno Jarrais
Doutoramento em Química Sustentável
Departamento de Química e Bioquímica
2017

Supervisor
Ana Cristina Freire, Full Professor
Faculdade de Ciências da Universidade do Porto

Acknowledgments

To Fundação para a Ciência e Tecnologia (FCT), for my PhD Grant with reference SFRH/BD/90015/2012.

To Departamento de Química e Bioquímica, Faculdade de Ciências, Universidade do Porto, for providing me the facilities for the development of my project.

To my supervisor, Professsor Cristina Freire, for the opportunity to develop this project, and for the valuable lessons and advices.

To Professor Fernando Pereira and Doctor Inês Rocha from Laboratório de Catálise e Materiais, Departamento de Engenharia Química, Faculdade de Engenharia, Universidade do Porto, for providing me access to their laboratory equipment.

To Doctor Lifeng Liu, from International Iberian Nanotechnology Laboratory, for providing me access to his facilities.

To Professor Alexandra Guedes, from Departamento de Geociências, Ambiente e Ordenamento do Território, Faculdade de Ciências, Universidade do Porto, for the assistance with the Raman measurements.

To all my colleagues from the laboratory, for the ready assistance and helpful advices.

To my parents, for the constant confidence in all my decisions.

To Ângela, for her everlasting support and confort…

Abstract

The present thesis is focused on the development of modified carbon materials for catalytic applications and on the fabrication of carbon-doped perovskite solar cells.

Multi-walled carbon nanotubes (MWCNT) and graphene flakes (GF) were modified through three different oxidation procedures: (i) nitric acid treatment; (ii) nitric acid followed by thermal treatment at 400 ˚C; (iii) gas phase oxidation with O_2. The oxidized materials showed an overall increase in the materials oxygen content and revealed that the different oxidation procedures promoted different surface oxygen groups compositions and structural properties. The catalytic studies showed that all the materials were active catalysts in the selective oxidation of *cis*-cyclooctene and that the modifications introduced in the pristine materials, through nitric acid followed by thermal treatment at 400 ˚C, originated catalysts with superior activity and selectivity. Reusability experiments revealed no loss of catalytic activity up to three catalytic cycles.

MWCNT and GF were doped with heteroatoms, namely N, P, B, and S, through simple ball milling procedures with adequate precursors - melamine, triphenylphosphine, boric acid, and sulfur - respectively, followed by thermal treatments. The materials surface composition was evaluated and the nature of the introduced heteroatoms was assessed, as well as their textural and structural properties. The catalytic studies showed that all the doped carbon materials outperformed their pristine counterparts in the reduction of 4-nitrophenol. (4-NP) Reusability experiments revealed no loss of catalytic activity up to three catalytic cycles for the doped carbon nanotubes, whereas the graphene flake materials showed some deterioration of catalytic performance.

Within the perovskite solar cells framework, mesoscopic mixed halide perosvkite based solar cells doped with graphene flakes in the electron transport layer (ETL) and in the hole transport layer (HTL), were prepared. Pristine devices with stable power to current efficiency (PCE) were successfully prepared, and used as a benchmark for the doped devices. Graphene flakes were introduced in the ETL through two different strategies: the doping of the ETL through method A resulted in devices with efficiencies below 1 %, which was attributed to extensive exciton quenching, whereas method B resulted in devices that revealed an overall inferior PCE, due to changes in charge carrier extraction efficiency at the carrier-selective contact. The device doped with GF in the HTL showed a great decrease PCE, which was attributed to the overextension of

the oxidized state of spiro-OMeTAD. Stability studies of the pristine solar cells revealed a significant increase in PCE after 100 days of desiccant exposure in the dark.

Keywords: Carbon nanomaterials, Multi-walled carbon nanotubes, Graphene flakes, Heteroatom doping, Carbocatalysts, Perovskite solar cells.

Resumo

A presente tese é centrada no desenvolvimento de materiais de carbono modificados para aplicação em catálise e na fabricação de células solares baseadas em perovesquites.

Foram modificados nanotubos de carbono de parede múltipla (MWCNT) e flocos de grafeno (GF) segundo três diferentes processos de oxidação: (i) tratamento com ácido nítrico; (ii) tratamento com ácido nítrico seguido de tratamento térmico a 400 ˚C; (iii) oxidação em fase gasosa com O_2. Os materiais oxidados mostraram um aumento generalizado na quantidade de oxigénio presente e revelaram que os diferentes processos de oxidação deram origem a diferentes composições de grupos de oxigénio superficiais, bem como diferentes propriedades estruturais. Os estudos catalíticos revelaram que todos os materiais são activos na reacção de oxidação seletiva do *cis*-cicloocteno e que as modificações introduzidas pelo tratamento com ácido nítrico seguido de tratamento térmico a 400 ˚C, deram origem a catalisadores com superior actividade catalítica e seletividade. As experiências de reutilização realizadas mostraram que não houve perda de atividade durante três ciclos catalíticos.

MWCNT e GF foram dopados com heteroátomos, nomeadamente N, P, B, and S, através de um processo simples de moagem de bolas com precursores adequados - melamina, trifenilfosfina, ácido bórico e enxofre - respetivamente, seguido de tratamentos térmicos. A composição superficial dos materiais preparados foi estudada de modo a avaliar os diferentes modos de ligação dos heteroátomos, bem como as diferentes propriedades texturais e estruturais. Os estudos catalíticos realizados revelaram que os materiais dopados com heteroátomos possuem uma maior actividade catalítica do que os materiais iniciais, na reação de redução do 4-nitrofenol. Os ensaios de reutilização revelaram que os nanotubos de carbono dopados não perderam actividade durante três ciclos catalíticos, enquanto que os flocos de grafeno mostraram alguma diminuiação da sua actividade catalítica.

No enquadramento das células solares baseadas em perovesquites, foram fabricadas células mesoscópicas de perovesquites mistas dopadas com flocos de grafeno na camada condutora de eletrões e na camada transportadora de lacunas. Dispositivos estáveis não-dopados foram preparados com sucesso, e usados como referência para os dispositivos dopados. Os flocos de grafeno foram introduzidos na camada condutora de eletrões segundo dois métodos diferentes: a dopagem pelo método A deu origem a dispositivos com eficiências abaixo de 1 %, o que foi atribuído à existência de um elevado grau de extinção de excitões, enquanto o método B

resultou em dispositos com uma eficiência inferior generalizada, relativamente às células de referência, devido a alterações na eficiência de extração de carga no contacto seletivo. O dispositivo dopado com GF na camada transportadora de lacunas, revelou uma elevada diminuição de eficiência, o que foi atribuído à extensão do grau de oxidação do condutor de lacunas spiro-OMeTAD. Estudos de establidade das células de referência revelaram uma aumento de eficiência significativo após 100 dias de exposição a um exsicante e sem iluminação.

Palavras-chave: Nanomaterias de carbono, Nanotubos de carbono de parede múltipla, Flocos de grafeno, Dopagem com heteroátomos; Células solares baseadas em perovesquites.

Contents

List of Figures

List of Tables

List of Abbreviations and Symbols

A_0	Absorbance at t=0
A_t	Absorbance at time t
a.u.	Arbitrary units
BET	Brunauer-Emmet-Teller
CCD	Charge-coupled device
CCG	Chemically converted graphene
CNT	Carbon nanotubes
CVD	Chemical vapour deposition
C_{60}SAM	C_{60} self-assembled monolayer
DSSC	Dye-sensitized solar cell
DMF	Dimethylformamide
E_c	Conduction band energy
EDS	Energy-dispersive x-ray spectroscopy
E_F	Fermi energy level
E_g	Bandgap energy
ETL	Electron transport layer
ETM	Electron transport material
E_v	Valence band energy
e^-	Electron
FF	Fill factor
FLG	Few-layer graphene
FTIR	Fourier transformed infrared spectroscopy
FTO	Fluoride tin oxide
FWHM	Full width at half maximum
GC	Gas chromatography
GF	Graphene flakes
GO	Graphene oxide
GQD	Graphene quantum dots
HTL	Hole transport layer
HTM	Hole transport material
h^+	Hole
I_D	Intensity of the Raman D band
I_G	Intensity of the Raman G band
I_{SC}	Short circuit current
I-V	Current-voltage
k	Reaction rate
L	Average crystallite size
LiTFSI	Bis(trifluoromethane)sulfanimide lithium salt
MeCN	Acetonitrile
MS	Mass spectrometry
m-TiO_2	mesoporous TiO_2
MWCNT	Multi-walled carbon nanotube
NMP	N-methylpyrrolidone
ORR	Oxygen reduction reaction
PCE	Power-to-current efficiency
PMMA	Poly(methyl methacrylate)
PSC	Perovskite solar cell
PV	Photovoltaic
P3HT	Poly(3-hexylthiophene)
rGO	Reduced graphene oxide
S	Ground state
S_{BET}	Specific surface area
SC	Solar cell
SEM	Scanning electron microscopy
spiro-OMeTAD	2,2',7,7'-Tetrakis-(N,N-di-4-methoxyphenylamino)-9,9'-spirobifluorene
ss-DSSC	Solid-state DSSC
STP	Standard temperature and pressure
SWCNT	Single wall carbon nanotube
S^*	Excited state
S^+	Oxidized state
TBHP	*Tert*-butylhydroperoxide
t-BP	4-*tert*-butylpyridine
TCO	Transparent conductive oxide
TEM	Transmission electron microscopy
TOF	Turnover frequency
TON	Turnover number
TPD	Temperature programmed desorption
UPS	Ultraviolet photoelectron spectroscopy
UV-Vis	Ultraviolet-visible spectroscopy
V_{OC}	Open circuit voltage
XPS	X-ray photoelectron spectroscopy

XRD	X-ray diffraction
4-AP	4-aminophenol
4-NP	4-nitrophenol
5-AVA	5-ammoniumvaleric acid
$\beta_{1/2}$	Line broadening at FWHM, in radians
θ	Bragg angle
λ	Wavelength

Chapter 1

Introduction

1

Introduction

1.1 Carbon materials

1.1.1 Background

The sixth element in the periodic table is among the most important ones. With about 180 ppm, carbon is only 17th on the list of terrestrial elements frequency, situated even after barium or sulfur. In comparison, the second most frequent element, silicon, is about 1300 times as abundant as carbon. However, carbon is essential for the assembly of all organic matter and the very existence of life on Earth. It is predestined for this central role especially due to its mid position in the periodic system and its associated ability to form stable substances with more electropositive and more electronegative atoms. In this thesis, however, the underlying organic chemistry resulting from these various bonding possibilities will only be mentioned when employed in the modification of the carbon materials, as the elemental forms of carbon are the focus of this work.

Elemental carbon in different forms played a role in human history long before the term “element” even existed. Charcoal and soot have been known and utilized for various metallurgic processes since ~ 5000 BC.

The first application of graphite is documented from the late central European Iron Age and employed to blacken pottery. Further examples of carbon being used for artistic purposes include pigment black from charcoal for cave painting. The term “graphite” reflects its use as a pigment: it is derived from the Greek word *graphein*, meaning to write. Pencils in the Middle Ages, were made from graphite, and ancient Egyptians used ink made from soot. Carbon in the shape of medicinal charcoal has long been known by its degassing and adsorbing effects and employed to treat gastrointestinal diseases. Charcoal is also a constituent of black powder.

Another carbon form, diamond, whose name is derived from the Greek words *diaphanes* (translucent) and *adamas* (invincible), was first discovered in India around 4000 BC.

In the 19th century, the exploration of the element took a steep progress, and many important insights were obtained. Shortly after Berzelius made a distinction between inorganic and organic matter in 1807, it became obvious that carbon played a

central role in organic substances, and laid the path for extensive research that largely influenced the development of bonding theories for complex molecules.[1]

August Kékulé interpreted benzene to be a cyclic entity in 1865 (Figure 1.1a). The concept of carbon as a tetrahedrally, four-fold coordinated atom was presented independently by J. H. van t'Hoff and J. A. Le Bel in 1874 and revolutionized the interpretation of the elements chemical activity (Figure 1.1b).

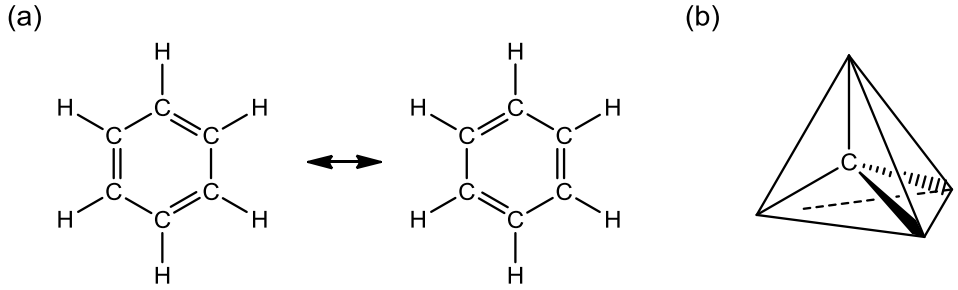

Figure 1.1 Kékulé's benzene structure model (a); van t´Hoff and Le Bel tetrahedral carbon model (b).

Since then, fundamental discoveries on carbon chemistry multiplied. L. Mond and co-workers published the first metal carbonyls in 1890, and in 1891, E. G. Acheson for the first time achieved artificial graphite via intermediate silicon carbide.[1] From 1985 on, the research on carbon gained a new momentum from the first observation of fullerenes by Kroto *et al.*,[2] and in 1991, carbon nanotubes (CNTs) were presented by Iijima as another new allotrope form.[3] More recently, in 2004, Novoselov *et al.* introduced the two-dimensional material graphene to the world.[4]

In fact, the phase diagram of carbon has grown out to be rather complex, with a multitude of allotrope modifications which in their turn are surrounded by additional high pressure and high temperature phases. All of them have distinct, and even opposite properties, which put carbon among the most versatile elements in materials science. This diversity is related to its electronic configuration ($1s^2\ 2s^2\ 2p^2$). In the vast majority of its compounds, carbon is tetravalent. The preferred tetravalence is explained with the hybridization between 2s and 2p orbitals, which the energy difference is rather low compared to the energy involved in covalent bonding, making it possible for the wavefunctions of these orbitals to mix and form equivalent hybridized orbitals. Figure 1.2 depicts six of the most notorious carbon allotropes, in which different hybridization states of carbon orbitals take place. The sp^3 orbitals are directed toward the four corners of a tetrahedron in diamond, whereas the $2s^2$ orbitals give rise to planar structures in fullerenes, nanotubes, graphite, and graphene.

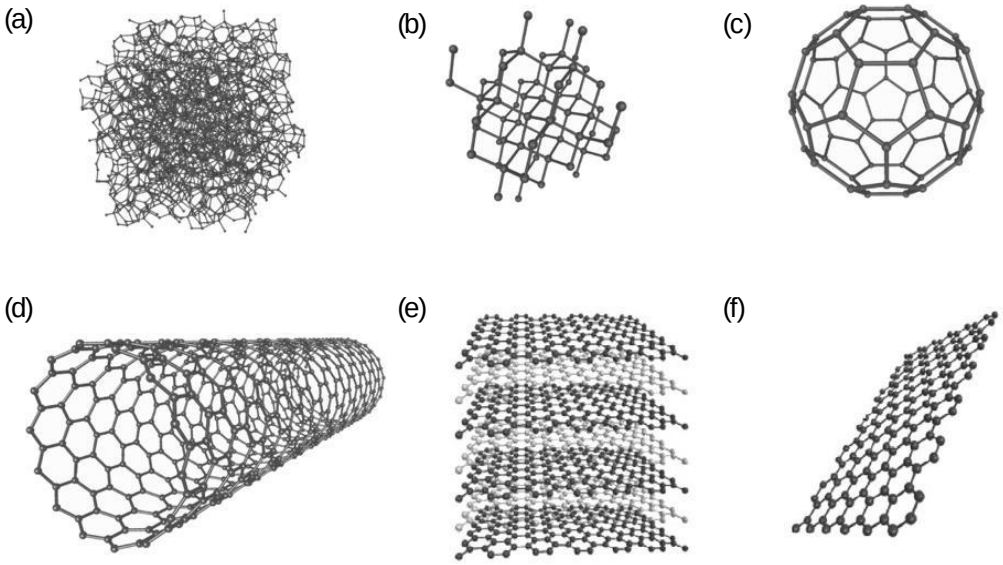

Figure 1.2 Schematic illustration of carbon allotropic forms: amorphous (a), diamond (b), fullerene (c), single-wall carbon nanotube (d), graphite (e), and graphene (f).

In addition to the allotropic forms of carbon shown in Figure 1.2, many others exist, such as activated carbons, carbon fibers, carbon blacks, carbon aerogels, etc. Impure carbon in the form of charcoal (from wood) and coke (from coal) is used in metal smelting. It is particularly important in the iron and steel industries. Graphite is used in pencils, to make brushes in electric motors and in furnace linings. Activated charcoal is used for purification and filtration. It is found in respirators and kitchen extractor hoods. Carbon fiber is finding many uses as a very strong, yet lightweight, material, and is currently used in high performance composites, such as in the automotive, aeronautical, and aerospacial industries. Industrial diamonds are used for cutting rocks and drilling. Activated carbons and carbon fibers are the most common materials used as adsorbents and catalyst supports.[5] The most recent discovery of carbon nanotubes, other fullerenes and atom-thin sheets of graphene promises to revolutionize in the electronics industry and in nanotechnology generally.[6] Despite this myriad of carbon forms and applications, focus will be given to carbon nanotubes and graphene, as these are the core materials of this thesis.

1.1.2 Carbon nanotubes

The structure of a CNT can be conceptualized by wrapping a graphene sheet into a seamless cylinder (Figure 1.3).

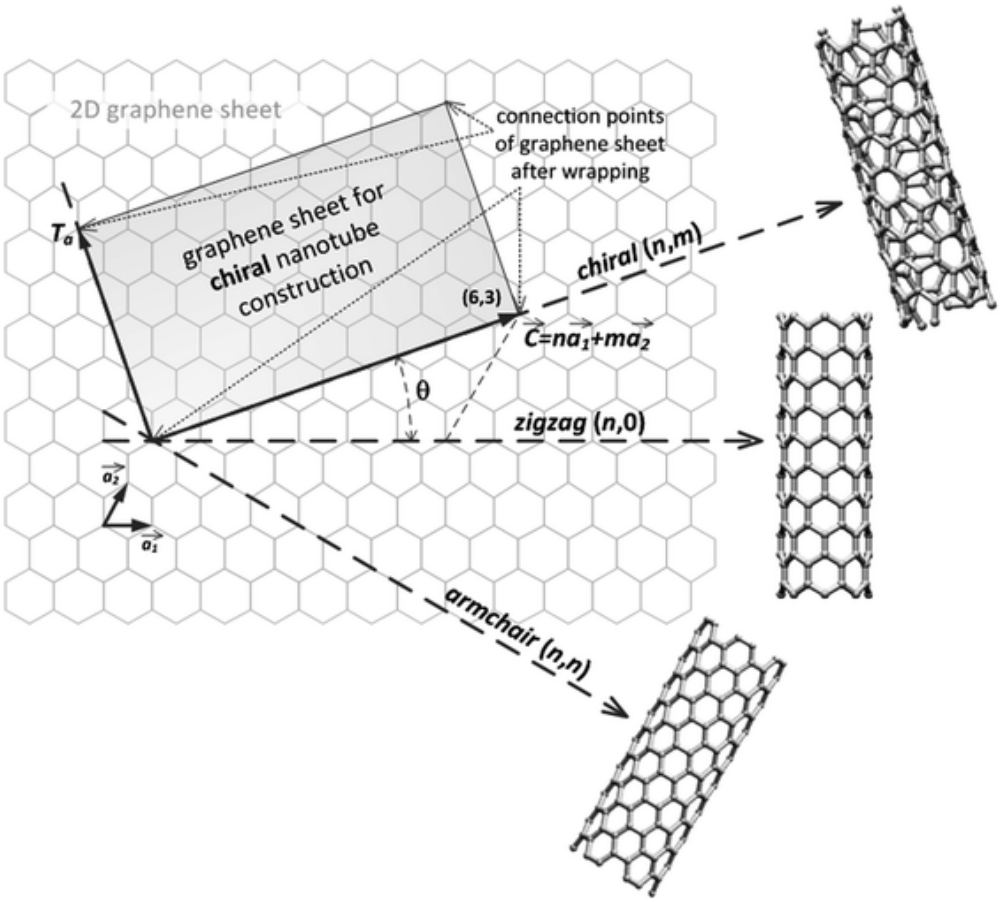

Figure 1.3 The principle of CNT construction from graphene sheet along the chiral vector $\vec{C}$. Adapted from Ref. [6].

The way the graphene is wrapped along the honeycomb graphene structure is given by chiral vector $\vec{C}$ which is a result of a pair (*n,m*) of integers that correspond to graphene vectors a_1 and a_2. There are two standard types of CNTs constructions from a single graphene sheet according to integers (*n,m*). The (*n,*0) structure is called ‘‘zigzag’’ and the structure where n = m (*n,n*) is called ‘‘armchair’’. The third non-standard type of CNTs construction, which can be characterized by the equation where *n* > *m* > 0, is called ‘‘chiral’’. The chirality determines the electrical, mechanical, optical and other properties of CNTs.[7] For a given (n,m) nanotube, if n = m, the nanotube is metallic; if n − m is a multiple of 3, then the nanotube is semiconducting with a very small band gap, otherwise the nanotube is a moderate semiconductor. CNTs can be either single-walled (SWCNTs) or multi-walled (MWCNTs). MWCNTs consist of multiple rolled layers (concentric tubes) of graphene. The diameter of CNTs varies from a few nanometres in the case of SWNTs to several tens of nanometres in the case of MWCNTs, and their lengths are usually in the micrometre range.[7] The interlayer distance in MWCNTs is close to the distance between graphene layers in graphite,

approximately 3.4 Å. Each individual shell can be described as a SWCNT, which can be metallic or semiconducting. Due to statistical probability and restrictions on the relative diameters of the individual tubes, one of the shells, and thus the whole MWCNT, is usually a zero-gap metal.

High temperature preparation techniques such as arc discharge or laser ablation were first used to produce CNTs but nowadays these methods have been replaced by low temperature chemical vapor deposition (CVD) techniques (<800 ˚C), since the orientation, alignment, nanotube length, diameter, purity and density of CNTs can be precisely controlled in the latter.[7] CVD with Fe, Co, Ni, or their alloys as a catalyst can be used to grow single-walled, double-walled, or multi-walled CNTs by controlling the particle size and chemical nature of the catalyst. The adhesive force between the catalyst and the substrate has been often attributed as an important factor in determining the growth mechanisms of CNTs.[8] The growth of CNTs can be divided into four steps: (1) supply of source carbon on the catalyst surface by adsorption and the subsequent catalytic decomposition of the adsorbed carbon by carbon atoms; (2) desorption of the carbon atoms into a gas phase; (3) diffusion of the carbon atoms away from the catalyst surface through bulk or surface diffusion; and (4) precipitation and formation of a graphite structure.[8] While weak contact between the catalyst and substrate favors a tip-growth mechanism, a strong interaction promotes base-growth. Single-walled and multi-walled CNTs with fewer than 7 walls are known to grow from their base, i.e., small metal particles, whereas multi-walled CNTs with more than 10 walls grow on the tip that feeds carbon.

The extraordinary properties of CNTs has been explored in a plethora of applications. Due to their high Young's modulus and tensile strength, CTNs have great potential in composite materials with improved mechanical properties.[9] CNTs are suitable as electron field emitters because of their nanosize, structural perfection, high electrical conductivity, and chemical stability, with an application in flat panel displays.[10] MWCNTs have been used to electro-catalize the oxygen reduction reaction, which is important for fuel cells.[11] Electrochemically Li intercalated SWNTs showed large irreversible capacities and voltage hysteresis which is an advantage for using them as battery electrodes.[12] The extraordinary high and reversible hydrogen adsorption in SWNTs has attracted much attention due to the possibility of using them as high-capacity hydrogen storage media.[13] It was proposed to use nanotubes as central elements of electronic devices including field-effect transistors, single-electron transistors and rectifying diodes.[14]

1.1.3 Graphene and derivatives

For several decades the isolation of graphene monolayers was thought to be impossible on the basis of, among other things, theoretical studies on the thermodynamic stability of two-dimensional crystals.[15] An important step in this direction was made by Geim and Novoselov in 2004, who reported a method for the creation of a single layer graphene sheet on a SiO_2 substrate by peeling the graphite by micromechanical cleavage, the so-called scotch tape method.[4]

Graphene is the name given to a monolayer of carbon atoms tightly packed into a two-dimensional (2D) honeycomb lattice, and is a basic building block for graphitic materials of all other dimensionalities (Figure 1.4).[16]

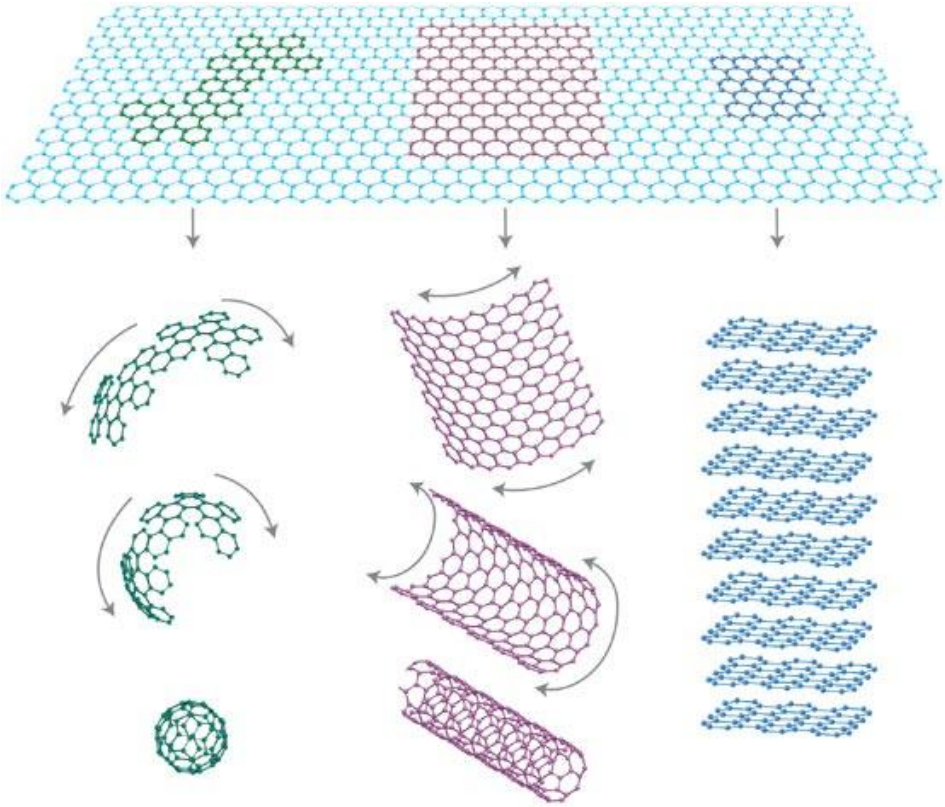

Figure 1.4 Graphene scheme as a 2D building material for carbon materials of all other dimensionalities. It can be wrapped up into 0D fullerenes, rolled into 1D nanotubes or stacked into 3D graphite. Adapted from Ref. [16].

The remarkable properties of graphene reported so far include high values of its Young's modulus (~1100 GPa),[17] fracture strength (125 GPa),[17] thermal conductivity (~5000 W m^{-1} K^{-1}),[18] mobility of charge carriers (200000 cm^2 V^{-1} s^{-1}),[19] and specific surface area (calculated value, 2,630 m^2 g−1)[20], plus fascinating transport phenomena such as the quantum Hall effect.[21]

Graphene can be produced by micro-mechanical exfoliation of highly ordered pyrolytic graphite,[4] epitaxial growth,[22] and chemical vapor deposition (CVD).[23]

Although these three methods can produce graphene with a relatively perfect structure and excellent properties, graphene produced by reduction of graphene oxide (GO) has some important characteristics as it is produced using readily available graphite material by cost-effective chemical methods in large scale. It is also highly hydrophilic and forms stable aqueous suspensions to facilitate the assembly of macroscopic structures by simple and cheap solution processes. The well-known methods used for the synthesis of graphite oxide are Brodie method, Staudenmaier method, Hofmann method, and Hummers method, and also their modified and improved forms.[24] Figure 1.5 depicts the reaction scheme for the preparation of graphene by reduction of GO.

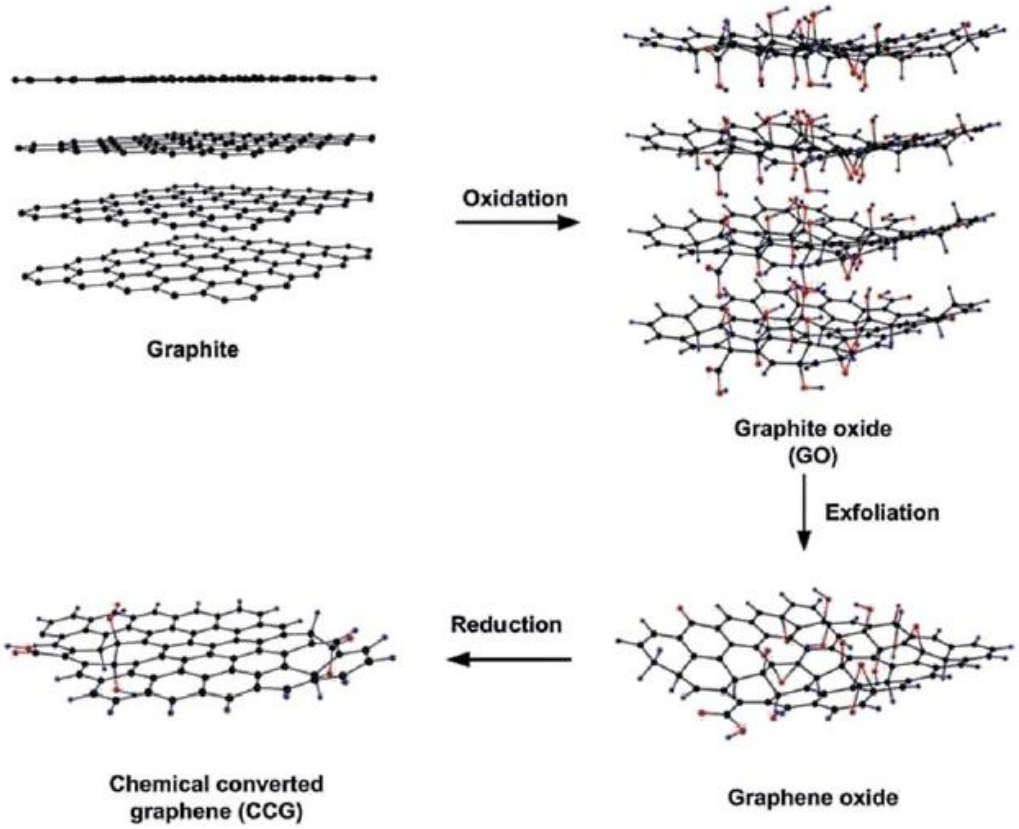

Figure 1.5 Preparation of chemically converted graphene by reduction of GO.

In all these methods, initially graphite powder is chemically reacted with acids (HCl, H_2SO_4 and HNO_3 etc.) followed by the intercalation of alkali metals (alkali metal compounds $KClO_3$, $KMnO_4$, $NaNO_3$ etc.) into the graphitic layers which further helps in the breaking of graphitic layers into small pieces. The graphene oxide product can be purified by centrifugation and dialysis to remove aggregates and various inorganic impurities such as metal ions and acids. Graphene oxide can be chemically reduced to graphene. Various inorganic and organic reducing agents such as hydrazine

monohydrate, sodium borohydride, hydroquinone, and strongly alkaline solutions have been explored for the chemical reduction of graphene oxide.[25] Additionally, GO reduction can also be carried out by thermal annealing in vacuum or in inert or reducing atmosphere, by microwave heating, by photoreduction, and through solvothermal or hydrothermal reduction.[24]

Direct exfoliation of graphite in N-methylpyrrolidone (NMP) also can produce a mixture of monolayer and few layered graphene dispersion without using hydrazine.[26] NMP was chosen because of its strong interaction with graphite or its surface tension matches that of graphene. The resulting graphene mixture is unoxidized and has high conductivity. Its dispersions can be used for synthesizing graphene/polymer composites. However, only graphene dispersions with low concentrations (about 0.01 mg mL^{-1}) can be obtained by this technique and sonication limits the size of graphene fl akes achievable. To avoid sonication, Pénicaud and co-workers developed a new technique using potassium intercalated graphite as the starting material.[27] They found that the exfoliation of this intercalated graphite took place spontaneously in NMP, yielding a dispersion of graphene. On the other hand, as chlorosulphonic acid was used to replace NMP, isotropic graphene dispersion with a concentration as high as 2 mg mL^{-1} was obtainable, one order of magnitude higher than any other known solvents or dispersants.[28] This is mainly due to that the superacid protonates the graphene layers to enhance their repulsion and the graphene obtained through this technique is of high quality, with over 70% being single layered graphene with few defects.

The unusual and remarkable properties of graphene and its derivatives, such as GO and few layer graphene (FLG) has led researchers to explore its potential in catalysis, electrocatalysis, Li-ion batteries, fuel cells, supercapacitors, and solar cells.[16,24,25,29]

1.1.4 Carbocatalysts

Many reactions involve metals, especially noble metals or metal oxides as catalysts. Although metal-based catalysts have been playing a major role in various industrial processes, they still suffer from multiple competitive disadvantages, including their high cost, susceptibility to poisoning, and detrimental effects on the environment. Moreover, the increased demand for these finite elemental resources and associated accessibility issues has led to concerns over the future security of supply, as can be seen in Figure 1.6.[30]

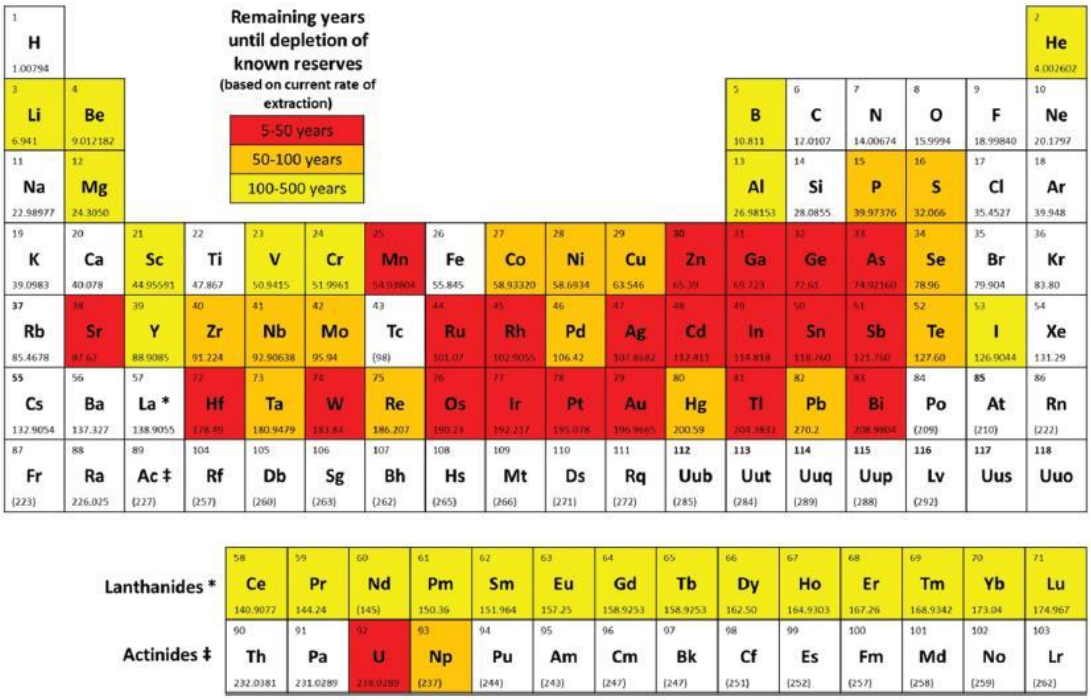

Figure 1.6 Remaining years until depletion of known reserves of elements. Adapted from Ref. [30].

Carbon materials have been used extensively as catalyst supports for many years.[5] However, owing to their wide availability, environmental acceptability, corrosion resistance, and unique surface properties, certain carbon materials have recently been demonstrated to be promising metal-free alternatives for low-cost catalytic processes.[5] The recent availability of novel carbon materials including fullerenes, nanofibers, nanotubes, nanodiamonds and graphene sheets, offer now new opportunities for the development of advanced metal-free materials with improved catalytic performance - carbocatalysts.[31]

Pristine carbon structures do not have a sufficient number of reactive sites to be a viable catalyst for most reactions, with the only active sites being located at the unsaturated carbons located at the edges or defects of the graphene layers. Nonetheless, the non-covalent binding interactions of graphite, CNTs or fullerenes with the target molecules, along with a fast charge transfer and resonance stabilization of intermediate states by these aromatic platforms, have often been cited to play catalytic role in reactions. [32–38]

Natural flake graphite flakes were used to catalyze the cleavage of alkyl ethers using acyl halides (Figure 1.7a).[32] The authors observed that tertiary alkyl ethers were selectively cleaved in the presence of secondary ethers, and that primary and secondary alkyl ethers were inert under the experimental reaction conditions tested. Similar reactivities were also observed in the graphite-catalyzed Friedel–Crafts-type

substitutions between various acid halides or alkyl halides and electron rich arenes to yield alkyl arenes (Figure 1.7b).[33,34]

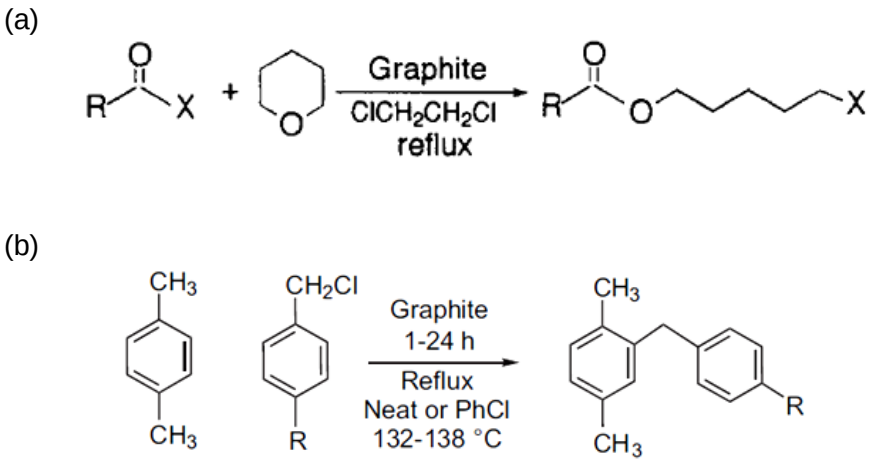

Figure 1.7 Graphite catalyzed (a) cleavage of ethers, followed by coupling with an acyl halide (adapted from Ref. [33]); (b) Friedel-Crafts-type substitutions (adapted from Ref. [34]).

Unfunctionalized carbon materials, such as CNTs and fullerenes, have shown some catalytic activity in the cracking and dehydrogenation of hydrocarbons.[35,36] In addition, fullerenes (both C_{60} and C_{70}) were also reported to be able to catalyze the hydrogenation of nitrobenzene to aniline at room temperature under UV-visible light irradiation.[37] The delocalized π-electron system of pristine graphene layers has also been reported to induce reactivity towards complexation reactions in organometallic catalysis.[38]

Despite these few examples of reactivity with pristine carbon materials, the catalytic activity of carbons can be greatly enhanced upon introduction of new active sites either through functionalization or through doping with heteroatoms.

In the absence of defects, the basal planes are not very reactive. Oxygenated functions have been studied most extensively, and are shown schematically in Figure 1.8. The concentration of these groups can be increased further by oxidative treatments, in either the gas or liquid phase. Thermal treatments at increasing temperatures can then be used to remove selectively some of the groups formed.[39] Acidic groups include carboxylic acids and anhydrides, lactones or lactols, and phenols, while carbonyl and ether are neutral or may form basic structures the nature of which is still open to debate, such as quinone, chromene, and pyrone groups. In addition, the π-electron system of the basal planes contributes to the carbon basicity.

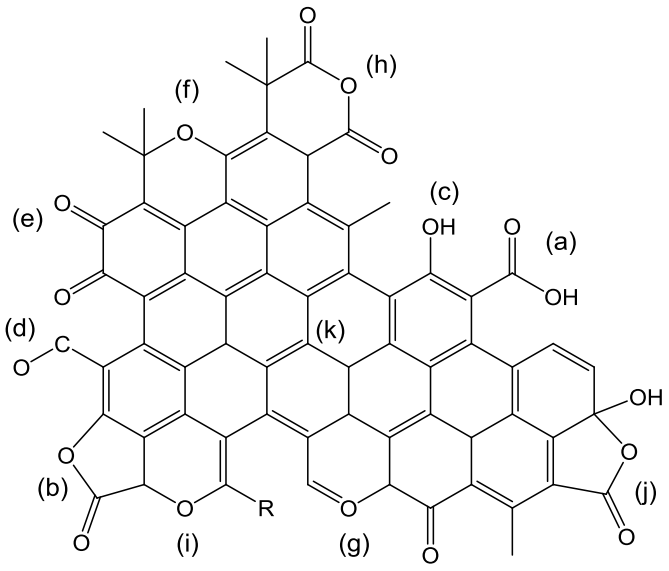

Figure 1.8 Oxygen-containing functionalities of carbon surface: (a) carboxyl groups, (b) lactone, (c) hydroxyl, (d) carbonyl, (e) quinone, (f) ether, (g) pyrone, (h) carboxylic anhydride, (i) chromene, (j) lactol, and (k) π electron density on carbon basal planes.

Heteroatom doping substantially modifies the atomic scale structures, surface energy, chemical reactivity and mechanical properties of carbon nanomaterials. In general, due to the small mismatch in atomic sizes, boron (B) and nitrogen (N) are the most popular doping elements in comparison to the other elements, such as sulphur (S), phosphorus (P), and silicon (Si), with significant size mismatches.[40] Heteroatoms can be incorporated in the graphitic lattice either during synthesis or post-synthetic treatments. Typical synthetic protocols for the heteroatom doping of carbon materials can be split into *in situ* vapor phase growth, and in post-synthetic doping. In vapor phase growth, a aliphatic or aromatic small molecule (methane, ethane, acetylene, alcohols, benzene, toluene, etc) or polymer is used as the carbon source and mixed with an appropriate heteratom precursor (ammonia, pyridine, triphenyl borane, dimethyl sulfide, etc), and treated at high temperatures. Other *in situ* procedures include ball milling and bottom-up synthesis.[41] In post-synthetic doping, pristine or oxidized carbon materials are mixed with the heteratom precursor and treated thermally under an inert atmosphere. If oxidized carbon materials are used, the high-temperature annealing restores the graphitic structure by removing oxygen functional groups and healing the structural disorder.[40]

a) Carbocatalysts for selective oxidation reactions

The oxydehydrogenation of cyclohexanol over carbon catalysts provides an excellent example of the strong influence of the surface chemistry on product

selectivity.[42] Carbon catalysts with surfaces of different chemical nature were investigated. The main products were cyclohexene, cyclohexanone, benzene, and phenol. Dehydration to cyclohexene was found to occur preferentially on the carboxylic acid groups (carbons treated with HNO_3), while the best selectivity to cyclohexanone were obtained on catalysts with high contents in phenol groups (carbons treated with H_2O_2 or oxygen).

Bielawski *et al.* reported a seminal work on the use of GO and graphite oxide as carbocatalysts for aerobic oxidation reactions (Figure 1.9).[43,44]

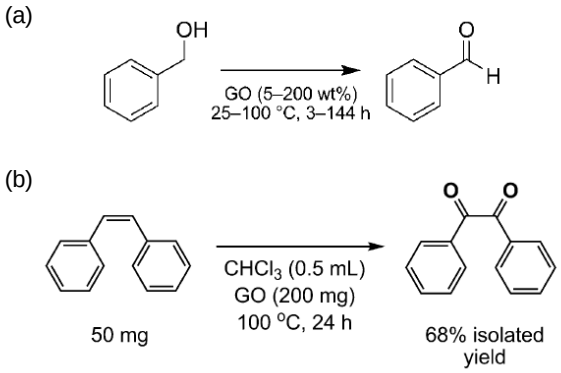

Figure 1.9 Oxidation of benzyl alcohol using graphene oxide (adapted from Ref [41]) Oxidation of cis-stilbene using graphite oxide (adapted from Ref [42]).

Neat benzyl alcohol was selectively oxidized by ambient oxygen to benzaldehyde in the presence of GO with TON based on weight of around 10^{-2} mol g^{-1}. In addition, high conversions to the corresponding carbonyl compounds were achieved for diphenylmethanol (>98%), 1,2-diphenylethane-1,2-diol (96%), and cyclohexanol (>98%), while moderate conversions were obtained for 1-phenylethanol (26%) and 2-thienylmethanol (18%). During the course of aerobic oxidation, partial reduction of the used GO material occurred, but experiments in the presence or absence of O_2 indicated that GO is acting as a catalyst and not only as an oxidizing agent. The catalyst was reused for up to 10 cycles for oxidation of benzyl alcohol without changes in the catalytic activity when loadings higher than 50 wt% of GO vs. substrate were present. However, at lower catalyst loadings (<20 wt%) GO becomes deactivated mainly due to reduction to rGO. In the same work, the authors used GO as catalyst for aerobic oxidation of unsaturated hydrocarbons and observed moderate conversions of cis-stilbene (56%), while trans-stilbene, 3-hexene, cyclohexane, and β-methylstyrene were found to be unreactive under the studied reaction conditions.[43]

Although molecular oxygen as a terminal oxidant should be the obvious oxidizing reagent, the use of other tolerable oxidants such as hydrogen peroxide (H_2O_2), *tert*-

butylhydroperoxide (TBHP), and peroxymonosulfate (PMS) can also be advantageous in order to achieve higher conversions and selectivity (both in terms of substrate and oxidant agent), envisaging applications in the synthesis of high added value chemicals or for environmental remediation. Ma *et al.* reported a direct, one-step hydroxylation of benzene to phenol using H_2O_2 as oxidant and chemically converted graphene (CCG) as catalyst (Figure 1.10).[45]

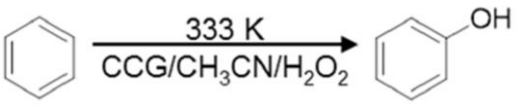

Figure 1.10 Oxidation of benzene using CCG as catalyst. Adapted from Ref. [43].

The authors observed that the oxidation proceeded with high selectivity and the catalyst was reused seven times without significant loss of catalytic activity. The high activity and selectivity of the catalytic oxidation using rGO was mainly attributed to different factors: (i) the preference of rGO to adsorb benzene with respect to phenol (thus avoiding over-oxidation of phenol to benzoquinone); (ii) the adequate π character of rGO and large surface area (446.5 m^2 g^{-1}) leading to strong adsorption of substrates; and (iii) low H_2O_2 decomposition. The same reaction of benzene hydroxylation to phenol by H_2O_2 using CNTs, provided a much lower catalytic activity (benzene conversion around 6%).[46] These positive results obtained with rGOs were also extended to other substrates including toluene, naphthalene, *p*-xylene, and ethylbenzene, reflecting different π–π interactions between rGO and the aromatics with steric hindrance being the major factor to be considered to rationalize the reactivity.[45]

Peng *et al.* demonstrated the use of N-doped CNTs as a metal-free catalyst for the liquid-phase aerobic oxidation of cyclohexane.[47] Using N-doped CNT (4.5 at% N) the whole reaction could be altered to one-step production of adipic acid to give selectivity as high as 60% at a conversion higher than 40% (Figure 1.11). Furthermore, no difference in both activity and selectivity was observed after five recycling tests, evidencing an excellent reusability. In a more recent work by the same group, Yu *et al.* synthesized N-, P- and B-doped CNTs with controllable heteroatom functionalities.[48] The authors found that N-doped CNTs and P-doped CNTs were active for the liquid-phase aerobic oxidation of cyclohexane, although P-doped CNTs suffered from a low specific surface area.

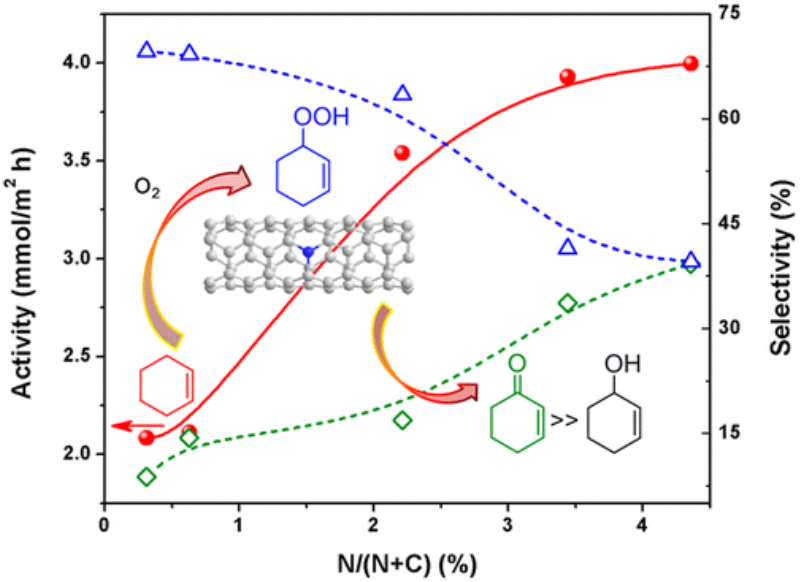

Figure 1.11 Variation of activity and selectivity of allylic products with the nitrogen content in N-doped CNTs. The selectivity was obtained at similar cyclohexene conversion of about 20%. Adapted from Ref. [47].

It was revealed that the electron transfer between graphene sheets and reactive radicals played a major role, which could be enhanced by n-type dopants, such as N or P functionalities. B acts in an opposite way due to its electron-deficiency, and was found not to improve the activity of CNTs.

Nitrogen-doped carbon nanotubes, prepared by CVD were tested in selective oxidation of benzyl alcohol to benzaldehyde with molecular oxygen as the terminal oxidant under mild reaction conditions.[49] The results showed that the N-CNTs exhibited much higher activity than the undoped CNTs, and the improved catalytic activity was attributed to the introduction of electron-rich nitrogen atoms in the graphitic domains enhancing electron transfer. Moreover, N-doped CNTs displayed excellent stability without any loss in activity and selectivity for benzyl alcohol oxidation after eight cycling reactions.

Wang *et al.* have employed a heat treatment procedure in NH_3 to synthesize N-doped graphene and reported its efficient catalytic activity toward the aerobic selective oxidation of different benzylic alcohols (Figure 1.12).[50]

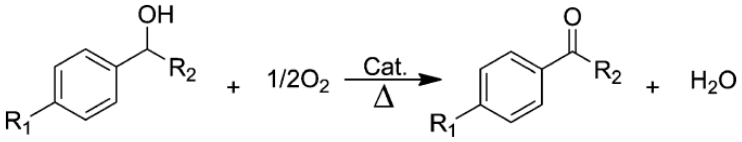

Figure 1.12 Catalytic oxidation of various types of alcohols over the N-doped graphene. Adapted from Ref [50].

They found that the nitridation temperature greatly influenced the N doping concentrations and formats. Graphitic-N was found to be the active site with good linear correlation with activities.

In addition to selective oxidation reactions, carbon materials have also been reported to be active in advanced oxidation processes, commonly used for pollutant removal from water. Among the most common are catalytic ozonation, catalytic wet air oxidation, and catalytic wet peroxide oxidation.[5]

b) Carbocatalysts for reduction reactions

Besides selective oxidations, carbon materials can be used as active catalysts for reduction reactions. Bao et al. reported the use of rGO as catalyst for hydrogenation of nitrobenzene with hydrazine at room temperature.[51] The authors showed the superior activity of rGO with respect to other carbonaceous materials (activated carbon, carbon black, graphite and GO) when working at room temperature. The presence of unsaturated carbon atoms at the edges of rGO and defects on rGO were proposed as the active sites for nitrobenzene reduction with hydrazine. The stability of rGO was established by performing nine catalytic cycles without observing loss of catalytic activity. It was proposed that the catalytic activity of rGO could be due to the unique electronic structure of zigzag edges in a single layer or a few-layer graphene.

Reduction of 4-nitrophenol (4-NP) to 4-aminophenol (4-AP) is one of the favorite test reactions to evaluate the catalytic activity for reductions of many homogeneous and heterogeneous catalysts. Activation of borohydride is a general reaction that has been considered to require metals as active sites since metal hydrides formed from the BH_4^- reagents are considered intermediates in this type of reduction. For this reason one of the targets in carbocatalysis has to be to find suitable metal-free carbon-containing catalysts that could also be used for this benchmark reaction. In this context, Chen et al. recently reported that rGO are suitable carbocatalysts for the reduction of the aromatic nitro group (Figure 1.13).[52] Hydroxyl and alkoxy radicals, as well as holes, were found beneficial to the catalytic performance, while epoxy and carboxyl groups were unfavorable and should be avoided. This conclusion was reached because a NaOH-treated rGO sample still containing carbonyl moieties exhibits significantly lower catalytic activity than the rGO.

Recently, Chen et al. reported the synthesis of N-graphene by hydrothermal treatment of GO and ammonia, and assessed its catalytic behavior in the reduction of 4-NP.[53] N-doped graphene was found to follow pseudo-zero-order kinetics, which was completely different from traditional pseudo-first-order reactions catalyzed by metallic nanoparticles, and this was assigned to the presence of smaller active sites.

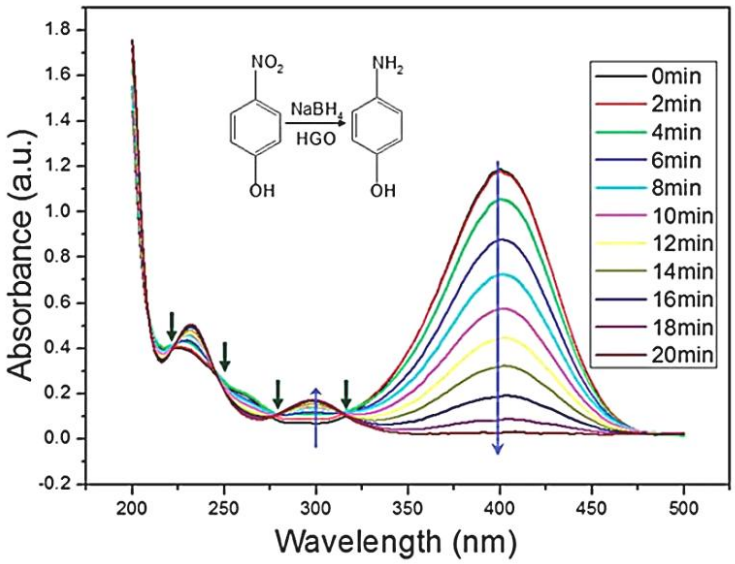

Figure 1.13 UV-vis spectroscopy monitoring of the catalytic reduction of 4-NP. Adapted from Ref. [52].

The authors proposed a reaction mechanism where only the carbon atom near the doped N atom could be activated to catch 4-NP species owing to its weaker conjugation compared to other carbon atoms, so the number of active sites on the graphene surface was much smaller than those of metallic nanoparticles (Figure 1.14).

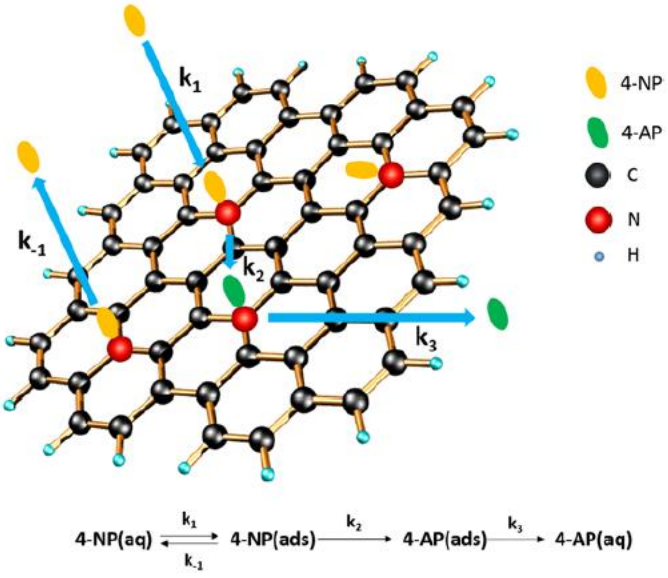

Figure 1.14 Catalytic process of the reduction of 4-NP on the surface of N-doped graphene. Adapted from Ref [53].

Therefore, the adsorption process of 4-NP on the surface of N-graphene was more pivotal than in the cases of metals, changing its reaction kinetics.

Since the work of Dai *et al.,* that reported excellent electrocatalytic performance of vertically aligned N-doped CNT arrays in the oxigen reduction reaction (ORR), there has been great progress in the development of carbon-based metal-free catalysts for the ORR.[54,55] However, electrocatalysis is beyond the scope of this work and will not be further adressed.

1.2 Carbon materials and solar cells

1.2.1 Background and evolution of solar cells

The worldwide demand for energy is expected to double by the year 2050 and triple by the end of the century. There is a serious concern that the production of oil will soon not be able to keep up with the demand for energy. Moreover, there is a growing consensus that the accumulation of CO_2 in the atmosphere originated from fossil fuels combustion, is leading to global climate changes.[56] The Sun is an obvious source of clean and cheap energy, with the solar flux containing 10000 times the average global power usage. In fact, efficient solar energy harvest is one of the most promising fields of study in materials chemistry nowadays. While technologies have been developed to harness solar energy efficiently, they are not yet an economic viable alternative to fossil fuels. The abundant supply and environmental friendliness of solar energy make the efficient and cost-effective conversion of solar radiation into electricity a compelling scientific goal.[57–60]

The history of photovoltaics started in 1839 with the work developed by the French physicist Alexandre Edmond Becquerel, who noticed the generation of an electric current between two platinum electrodes immersed in an illuminated solution containing a metal halide salt.[61] In 1873, the photovoltaic effect in selenium was observed by Willoughby Smith.[62] William Grylls Adams and his student, Richard Evans Day, discovered the photovoltaic effect in 1876, illuminating a junction between selenium and platinum, which resulted in the construction of the first selenium solar cell in 1877.[63] Despite these photovoltaic cells showed less than 1 % conversion of incident light into electric power and aged quickly, they are landmarks in the development of this technology. The theory behind the photovoltaic phenomenon was first described by Albert Einstein in 1904, which won him the Nobel Prize in 1921.[64] In 1918, Jan Czochralski developed the "*Czochralski method"*, a cornerstone of modern materials science, which consisted in a method of crystal growth used to obtain single crystals of semiconductors.[65] A few years later, the Bell Laboratories used the "*Czochralski method*" to grow single germanium crystals, introducing the use of this method in the production of suitable semiconductors, and the first germanium solar cell

was produced in 1951. Later on, in 1954, at the Bell Laboratories, the first high-power silicon solar cell with 6% efficiency – much more efficient than the first selenium solar cell – was developed. This was a very important milestone in photovoltaics technology and these SCs would later become known as the first generation SCs. However, the cost of the photogenerated electricity was so high that this recent technique was mainly only used in aerospace applications. Only in 1970 the research allowed a reduction of about 80% in the PV cost, enlarging its applications. The energy crisis in the 1970's boosted the research and development of several technologies for producing energy from renewable sources, including photovoltaics. During this period, the second generation solar cells emerged, solving some of the main problems of the first generation solar cells: these single junction devices involve high energy and labor inputs, which make them rather unviable because of the elevated costs. In opposition, since cadmium telluride (CdTe), copper indium gallium selenide (CIGS), copper indium diselenide (CIS), polycrystalline and amorphous silicon can be applied as thin-films over a substrate such as glass or ceramics, the costs are much lower. In the 1990's large-scale solar cell producers established in the PV market and the world biggest photovoltaic system was planned.

Summarizing, first generation SCs are based on crystalline Si [66] (c-Si), whilst second generation SCs are based on thin film technology which has often involved vapor deposited semiconductors. By contrast, third generation SCs are solution processed SCs based on organics, hybrids, inorganic semiconductors[67] and include dye-sensitized solar cells (DSSCs) and nanostructured SCs.[68]

In 1991, Brian O'Regan and Michael Grätzel described for the first time a three dimensional (bulk) heterojunction applied to the fabrication of DSSCs. This new device was based on the use of semiconductor films consisting of nanometre-sized TiO_2 particles, together with newly developed charge-transfer dyes. These authors report an astonishing efficiency of more than 7%.[60] Despite the exciting progresses in photoelectrochemistry and particularly in the field of DSSCs, so far the conversion of sunlight into electrical power has been widely dominated by solid-state crystalline silicon solar cells. As mentioned before, dye-sensitized solar cells are a new thin-film generation of photovoltaic devices, differing from the conventional photovoltaic technologies in what concerns the light absorption function, which is separated from the charge carrier transport. A schematic representation of the dye-sensitized solar cell is shown in Figure 1.15.

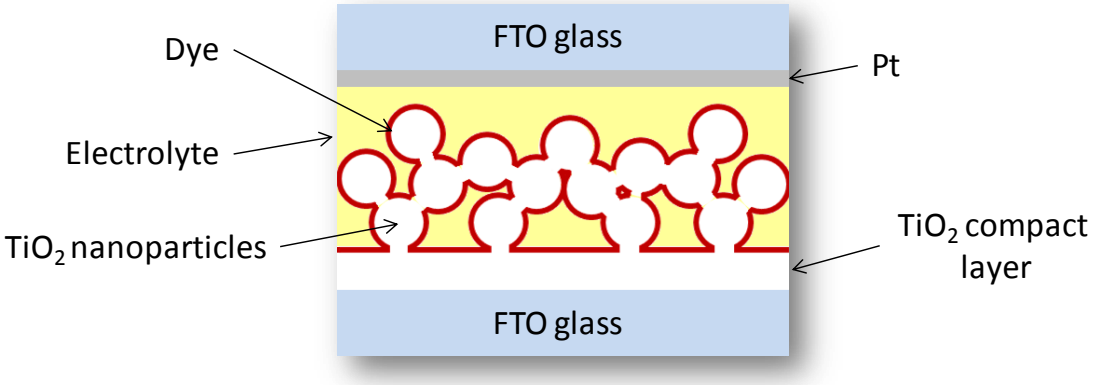

Figure 1.15 Dye-sensitized solar cell device schematic. Liquid-based DSCs are comprised of a transparent conducting oxide (such as fluorine-doped tin oxide, FTO) on glass, a nanoparticle photoanode (such as TiO_2) covered in a monolayer of sensitizing dye, a hole-conducting electrolyte and a platinum-coated, FTO-coated glass back-contact.

Due to its multiple advantages, titanium dioxide became the semiconductor of choice for the photoelectrode; furthermore, it is low cost, widely available, and non-toxic. Ruthenium complexes such as [Ru(4,4'-dicarboxy-2,2'-bipyridine)$_3$] were employed as sensitizer very early on and are still now the most commonly used sensitizer.[59] Finally, the main redox couple used is triiodide/iodine. Figure 1.16 shows schematically the operating principles of a p-n junction SC (such as a c-Si SC) and of a DSSC.

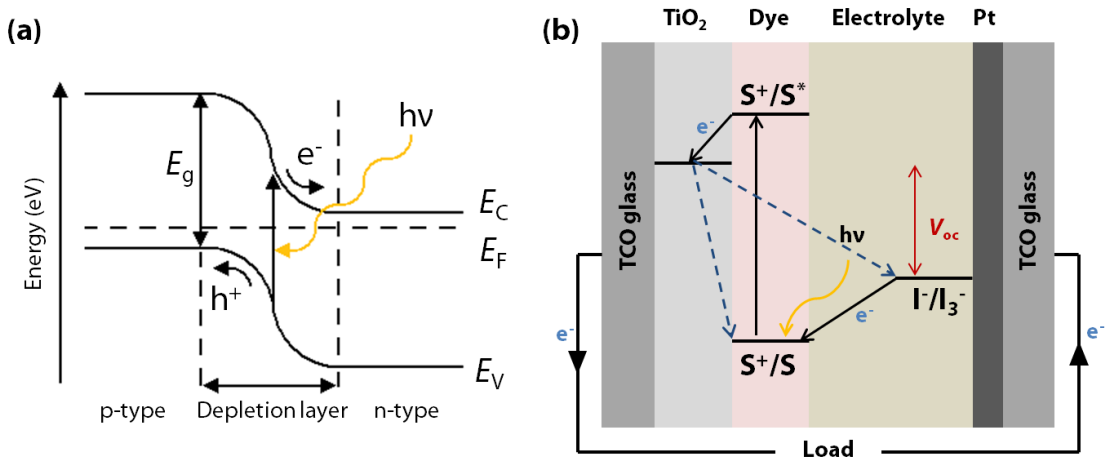

Figure 1.16 (a) Energy band scheme of a p-n junction solar cell; (b) principle of operation of a dye-sensitized solar cell. E_g - bandgap energy; E_V - valence band energy; E_C - conduction band energy; E_F - semiconductor Fermi energy; e^- - electrons; h^+ - holes; S - ground state of the sensitizer; S^* - excited state of the sensitizer; S^+ - oxidised sensitizer; TCO - transparent conductive oxide; Pt - platinum.

In a conventional p-n junction photovoltaic cell the semiconductor assumes simultaneously the function of harvesting sunlight to create an electron-hole pair and the transport of charge carriers (Figure 1.16a).

On the other hand, in dye-sensitized solar cells the dye is the element responsible for light absorption and charge generation, while charge transport occurs both in the semiconductor and in the electrolyte (Figure 1.15b).

The first step is the absorption of a photon by the sensitizer *S*, leading to the excited sensitizer S^* which injects an electron into the conduction band of the semiconductor, leaving the sensitizer in the oxidized state S^+. The injected electron flows through the semiconductor network to arrive at the back contact and then through the external load to the counter electrode to reduce the redox mediator which in turn regenerates the sensitizer, completing the circuit.

Since the work published in 1991, [60] these cells have attracted the interest of the scientific community not only because of their simple and low-cost fabrication process, but also due to their excellent performance under both direct and diffuse light conditions. In contrast to the vacuum deposition methods for conventional thin film devices, most of the fabrication steps for 3rd generation solar cells are based on solution processed methods. This is considered as one of the most significant attractive characteristics regarding the reduction of the fabrication cost.

Recent developments in the organometal trihalide perovskite (such as $CH_3NH_3PbI_3$) based solar cells upgraded the 3rd-generation solar device from both material and architecture perspectives. The certified efficiency has reached 22.1%.[69] Organic–inorganic hybrid perovskite $CH_3NH_3PbX_3$ (X = Br, I) was initially utilized as a light absorber in 2009 by Miyasaka and co-workers.[70] This pioneering work was conducted by absorbing the perovskite onto the TiO_2 surface in conventional DSSC structures, using liquid electrolytes.

Moving to solid-state hole transporting materials (HTM) and increasing the loading capacity of the perovskite materials significantly improved the efficiency. In 2012, Park, Grätzel and coworkers utilized 2,2',7,7'-tetrakis-(N,N-di-4-methoxyphenylamino)-9,9'-spirobifluorene (spiro-OMeTAD) as the solid state HTM, generating an efficiency of 9.7%.[71] This device is based on mesoporous TiO_2 nanoparticles supported $CH_3NH_3PbI_3$. Subsequently, the efficiency was improved to around 15% by two typical device structures based on the planar heterojunction and the mesoporous TiO_2 network.[72,73] The research enthusiasm in the perovskite solar cell was thus fueled by the high achievable efficiency, while a number of perovskite materials, device configurations and fabrication techniques were investigated for comprehensively improving the device performance.

The perovskite story – bearing the name of Russian mineralogist L. A. Perovski – began with the discovery of calcium titanate ($CaTiO_3$) in Russia by Gustav Rose in 1839. The compounds having similar crystal structures like $CaTiO_3$ are known as

perovskites. Ideally, perovskite can be represented by the simple building block AMX_3, where M is the metal cation and X an oxide or halide anion, etc. They form a MX_6 octahedral arrangement where M occupies the center of an octahedron surrounded by X located at the corners (Figure 1.17). The MX_6 octahedron extend to a three-dimensional network by connecting all the corners. Species A represents a cation which fills the hole formed by the eight adjacent octahedron in the three-dimensional structure and balances the charge of the whole network.[74]

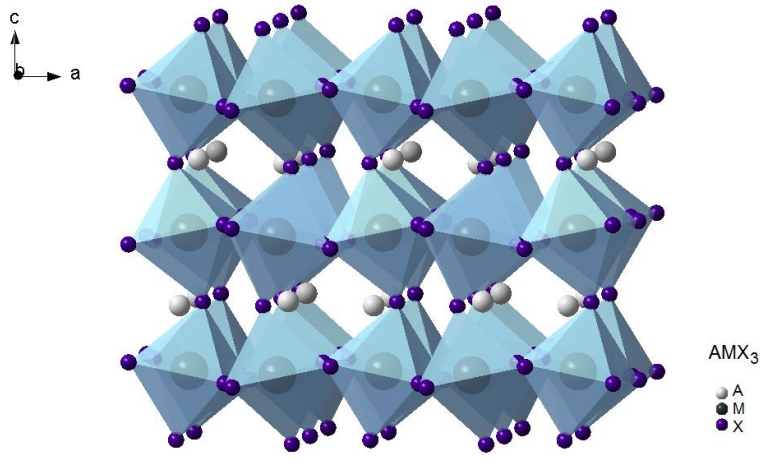

Figure 1.17 Extended perovskite network structure connected through corner-shared octahedron.

The large metal cation A can be Ca, K, Na, Pb, Sr, or various rare metals. In case of organic–inorganic hybrid perovskite, A is replaced by an organic cation, which is enclosed by twelve nearest X anions. The prerequisite for a closed-packed perovskite structure is that the organic cation must fit in the hole formed by the eight adjacent octahedra connected through the shared X corners. Too bulky organic cations cannot be embedded into the 3D perovskite. The size of organic cation and metal ion is an important parameter to modulate the optical and electronic properties of perovskite material. Ideally, perovskites have cubic geometry but in fact, they are pseudo-cubic or distorted cubic in nature.[75] Any sort of distortion will affect the physical properties of perovskite materials, such as electronic, optical, magnetic and dielectric properties.

Recently, organo-lead halide perovskite materials have drawn substantial interest as light harvester in mesoscopic solar cells due to their large absorption coefficient,[76] high charge carrier mobilities,[77] solution processability, and tunable optical and electronic properties. Miyasaka *et al.* were the first one who attempted $CH_3NH_3PbX_3$ (X=Br, I) perovskite nanocrystals as sensitizers in liquid electrolyte-based DSSCs and measured 3.8% and 3.1% PCE using $CH_3NH_3PbI_3$- and $CH_3NH_3PbBr_3$-based cells,

respectively. A very high photovoltage of 0.96 V was achieved with the lead bromide-based cell, which was associated with the higher valence band of the bromide compare to the iodide.[70] Subsequently, Park *et al.* fabricated liquid DSSCs using ca. 2-3 nm sized $CH_3NH_3PbI_3$ nanocrystals with iodide redox shuttle and improved PCE of 6.54% was obtained at 1 sun illumination.[78] $CH_3NH_3PbI_3$ was prepared *in situ* on a nanocrystalline TiO_2 surface by spin-coating an equimolar mixture of CH_3NH_3I and PbI_2 in γ-butyrolactone solution and the measured band gap was 1.5 eV according to ultraviolet photoelectron spectroscopy (UPS) and UV/Vis spectroscopy. Later, $C_2H_5NH_3PbI_3$ was synthesized by replacing methyl by ethyl ammonium iodide, and its crystal structure was identified as 2H perovskite-type orthorhombic phase. A valence band energy of 5.6 eV was measured by using UPS, and the optical band gap estimated from absorption spectra was ca. 2.2 eV. With I_3^-/I^--based redox shuttle, the $C_2H_5NH_3PbI_3$-sensitized solar cell gave PCE of 2.4% at 1 sun intensity (100 mW cm^{-2}).[79] However, these devices were unstable and performance dropped rapidly due to the dissolution of perovskite in the presence of liquid electrolyte. To protect the perovskite from corrosion and recombination and to avoid direct contact between perovskite and electrolyte, an insulating layer of aluminum oxide was introduced between the $CH_3NH_3PbI_3$-sensitized TiO_2 film and the liquid electrolyte, and the PCE significantly increased from 3.56 to 6.00%.[80] However, this PCE was still lower than that of counterpart DSSCs and thus requires further optimization. The curiosity to use perovskite in ss-DSSCs has then further fueled the research field. The cell architecture of perovskite-sensitized mesoscopic solar cells is similar to the ss-DSSC as shown in Figure 1.18a and just differs by the use of perovskite as light absorber instead of dye.

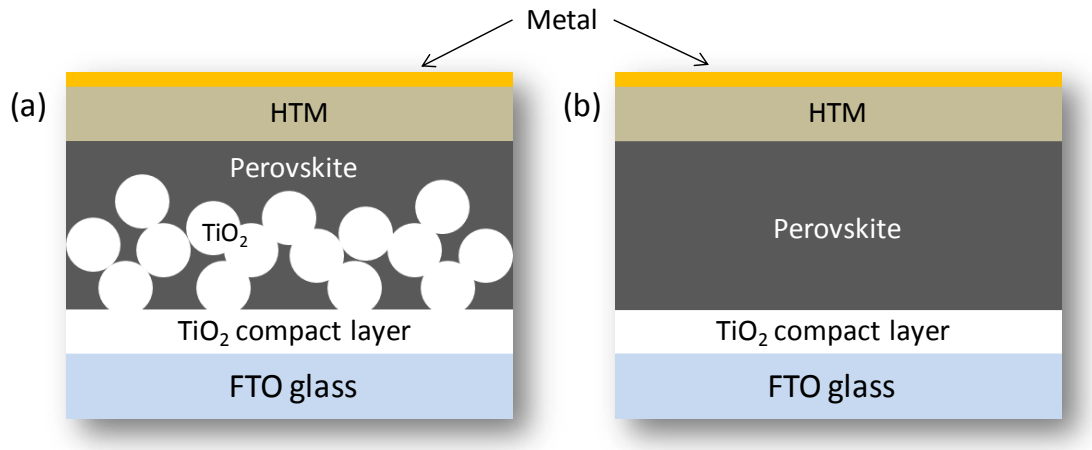

Figure 1.18 A scheme of: (a) a conventional mesoporous TiO_2 network based perovskite solar cell; (b) a planar heterojunction based perovskite solar cell.

The next breakthrough came in late 2012, when M. Grätzel and co-workers used $MAPbI_3$ as a light harvester in combination with the solid hole conductor 2,2',7,7'-tetrakis-(N,N-di-4-methoxyphenylamino)-9,9'-spirobifluorene (spiro-OMeTAD) on mesoporous TiO_2 (m-TiO_2), which led to a PCE of 9.7%.[71] Soon after that, H. Snaith in collaboration with T. Miyasaka discovered that in "meso-superstructured" solar cells the n-type mesoporous oxide can be replaced by an inert scaffold, such as Al_2O_3, onto which $CH_3NH_3PbI_{3-x}Cl_x$ and spiro-OMeTAD were coated.[81] The authors claimed that compared with the cells with m-TiO_2, the use of the Al_2O_3 scaffold avoids the voltage drop associated with the occupation of the TiO_2 band-tails and generates increased open circuit voltage (V_{oc}) values as high as 1.13 V and an efficiency of 10.9%. This result established that the perovskite materials can also behave as n-type semiconductors.

Since the middle of 2013, several milestones in PCE improvement are being witnessed due to the innovation of the cell fabrication technique, which leads the efficiency of organometal halide perovskite based solar cells over 15% (Figure 6). First came the introduction of a sequential deposition method (SDM) for the fabrication of perovskite on the m-TiO_2 film, which gave a PCE of 15% and a certified value of 14.1% with high reproducibility,[72,82] then came the planar heterojunction perovskite solar cell (Figure 1.18b) fabricated by vapor deposition which demonstrated 15.4% PCE and matched the 15% efficiency record of the mesoporous cell.[73]

After a series of eye catching PCE values, the PCE of 22.1% was certified in 2016.[69] Such a swift rise of PSC efficiency within only 6 years has been unprecedented in the history of photovoltaic technology.The fast development has triggered tremendous research interest followed by rapid and continuous improvements in the whole perspective of the relative PV devices and discussions about the underlying principles and the potential for further improvement of efficiency and stability. The remarkable synergistic achievements on devices from both materials science and device engineering promise further breakthroughs in this field of study.

1.2.2 Carbon materials as dopants in perovskite based solar cells

PSCs have several advantages such as remarkably high efficiency along with a simple and low cost synthesis. However, they also suffer from several drawbacks namely: (i) use of expensive, rare materials, (ii) high-temperature processing of n-type TiO_2 layer, (iii) relatively slow electron transport between the perovskite and TiO_2 and (iv) a lack of long-term stability. Consequently, it is necessary to overcome these issues in order to make this novel high efficiency solar cell commercially viable.

Carbon nanomaterials, with their excellent conductivity and good chemical stability, are very promising candidates for the development of this emerging technology. Furthermore, it is no surprise that carbonaceous materials including carbon particles, carbon nanotubes (CNTs) and graphene would have significant role in the development of PSCs as they have been extensively studied in various energy related applications owing to their excellent properties, low cost and abundance.

a) Carbon materials in counter electrodes

Thin layers of noble metals such as gold (Au) or silver (Ag) prepared by thermal evaporation are used as the back contact in PSCs. However, the use of the thermal evaporation process involves inherently complicated and costly vacuum technologies that can limit large-scale production of PSCs. Therefore, the replacement of this precious metal electrode with other low cost materials that are abundantly available whilst maintaining high performance is urgently required.

Han's group was the first to report the implementation of carbon materials in the counter electrode of $CH_3NH_3PbI_3$ based PSCs.[83] They deposited a carbon black/graphite composite via screen printing technique on the PSC photoelectrode that consisted of FTO glass substrate, TiO_2 compact layer, mesoporous TiO_2 layer and ZrO_2 spacer layer. Finally, the manufacturing process of the PSC was completed by drop-coating of $CH_3NH_3PbI_3$ perovskite sensitiser onto the mesoscopic carbon layer (Figure 1.19).

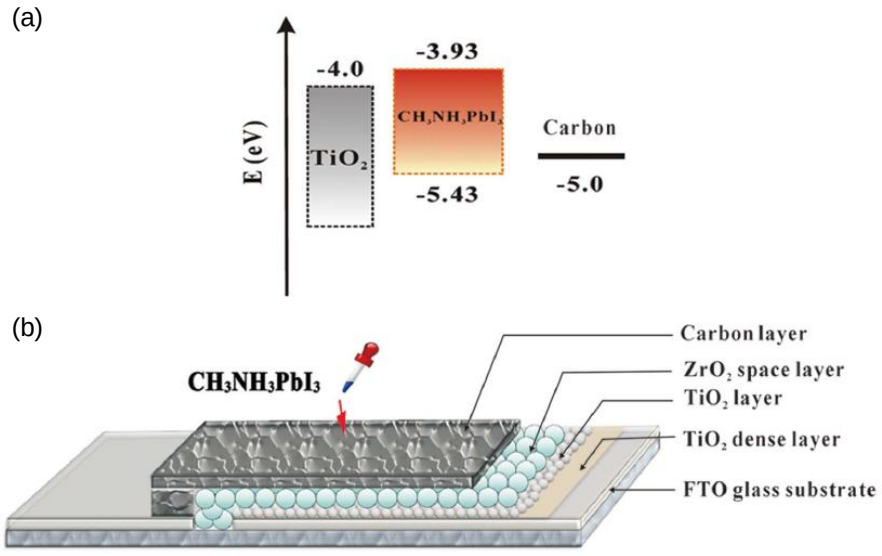

Figure 1.19 Energy levels of TiO_2, $CH_3NH_3PbI_3$, and carbon (a); schematic structure of a carbon based monolithic device (b). Adapted from Ref [83].

The highest PCE (6.64%) was achieved by PSC assembled with spheroidal graphite based carbon composite cathodes. One of the main reasons for this good performance by carbon cathode employed PSCs is, of course, the suitable energy levels of carbon material when compared with the other components of the device.

Meanwhile, the collaborative work of Han's and Graetzel's group reported the fabrication of holeconductor-free and fully printable PSCs.[84] Indeed, this work achieved the highest efficiency to date of carbonaceous cathode based cells. The manufacturing process of this porous carbon cathode based cell was unique in that it used 5-ammoniumvaleric acid (5-AVA) iodide based perovskite as a sensitiser. The 5-AVA played an important role in controlling the formation of perovskite crystals in the mesoporous oxide and providing better growth within the network. Consequently, the 5-AVA cations based perovskite provided good surface contact with the TiO_2 and lower defect concentration. Indeed, the measured short circuit current (J_{sc}), open circuit voltage (V_{oc}) and fill factor for this PSC which still used the carbonaceous cathode were 22.8 mA cm^{-2}, of 0.86 V and 0.66, respectively and yielded a PCE of 12.8%.[84]

Li *et al.* first reported CNT networks as the counter electrode of PSC.[85] A reasonable comparison was made by these authors by fabricating HTM-free PSCs based on only CNTs or only Au electrode. In the absence of organic HTMs, the efficiency of CNTs cathode employed cell was 6.87% which was far higher than that (5.14%) achieved by the Au based device. This impressive result indicates that the use of CNTs can outperform those precious metal based PSCs. Furthermore, the efficiency of the PSC fabricated with CNTs cathode was improved to be 9.9% by adding spiro-OMeTAD.

b) Carbon materials in the hole transporting layer (HTL)

The most commonly employed HTM in solid-state solar cells including PSCs, is spiro-OMeTAD. There are two disavantages for using spiro-OMeTAD: (i) limited long-term stability and (ii) high material cost. Therefore, exploring alternate cheaper materials that can show high stability whilst maintaining efficiency is of great interest.

Very recently, a composite material based on CNTs and polymer has been used as a highly stable hole collection layer in PSCs as reported by Snaith's group, and depicted in Figure 1.20.[86] They used an insulating hydrophobic polymer poly-(methylmethacrylate) (PMMA) because this polymer inhibits both the intrusion of moisture into the perovskite and the evaporation of the methylammonium iodide. By doing so, PMMA exhibited better stability compared to the conventional HTMs even after 96 h at 80 ˚C in air.

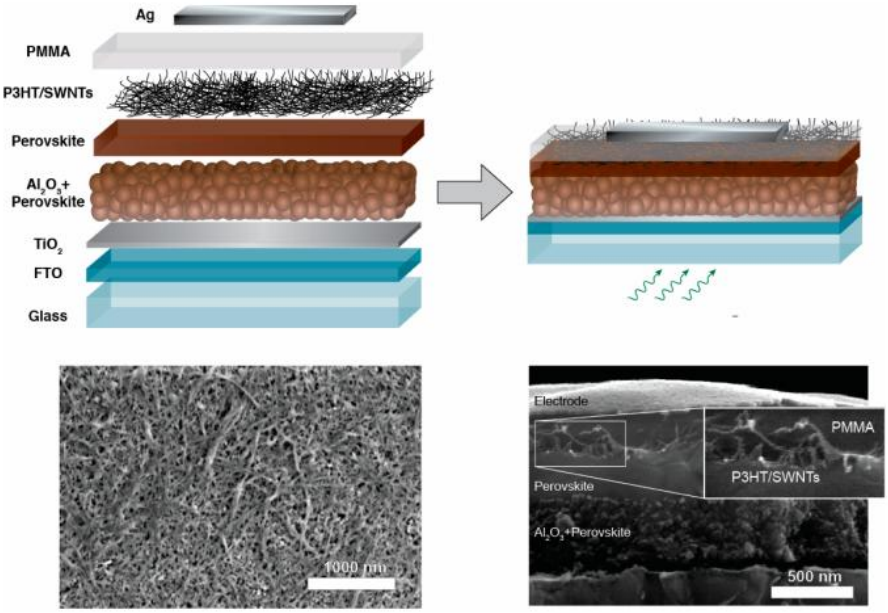

Figure 1.20 Schematic illustration of the solar cell with a carbon nanotube/polymer composite as hole-transporting structure. Adapted from Ref [86].

However PMMA is insulating, subsequently the authors incorporated highly conductive CNTs into the hole transporting layer of P3HT to efficiently transport the holes within the cells, and were able to achieve an energy conversion efficiency of 15.3%. This solar cell showed excellent stability not only under thermal stress but also their resistance to water was also increased. Based on this study, it can be summarised that the presence of carbon materials (CNT/polymer hybrids in this work) has an important role in improving the stability of PSCs.

Luo et al. demonstrated that p-type solution-processable rGO combined with dopant-free spiro-OMeTAD could be used as an efficient HTM in perovskite solar cells with superior stability and high-efficiency, as shown in Figure 1.21.[87] Through the use of a p-type and highly conductive reduced graphene oxide (rGO) reduced by ferrous iodide acid solution, combined with dopant-free spiro-OMeTAD as a hole extraction, the authors achieved a maximum power conversion efficiency (PCE) of 10.6%, greatly outperforming the reference devices based on pure dopant-free spiro-OMeTAD (PCE = 6.5%). The authors proposed the existence of an alternative route for hole transport in rGO/dopant-free spiro-OMeTAD, in which the holes in spiro-OMeTAD were transferred to rGO and finally reached the metallic back electrode, in addition to the individual routes promoted by rGO and spiro-OMeTAD.

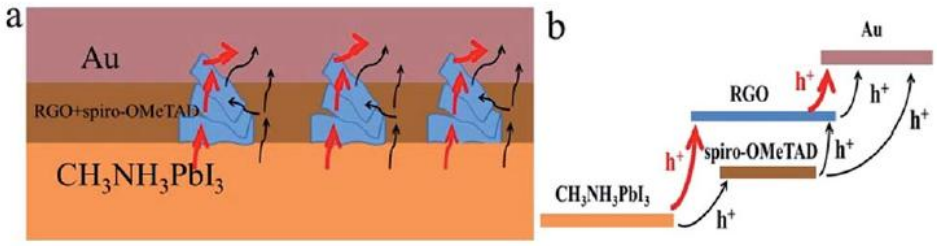

Figure 1.21 Schematic illustration (a) and energy levels of hole transport in completed perovskite solar cells (b). Adapted from Ref [87].

Impressively, only a 15% PCE degradation is observed for the device with RGO/dopant-free spiro-OMeTAD without encapsulation after 500 h, whereas the PCE drops by 65% for the device with LiTFSI and pyridine doped spiro-OMeTAD.

c) Carbon materials in the perovskite layer

Perovskite sensitizers are used due to their superb light-harvesting characteristics and are the key to charge generation and electron and hole injection into the conduction band of TiO_2 and valence band of HTM, respectively. However, one particular concern is the injection time of electrons to the TiO_2, with recombination reduced when the injection time is shorter. The electron injection time from the perovskite to the electron acceptor has been measured to be 0.3 ns,[88] which can be considered too long compared to the measurement of the hot carrier cooling (or thermalization) time (0.4 ps).[89] Once again, carbon based materials could address this limitation of PSCs as they have shown an ultrafast electron injection to the TiO_2 interface.[90,91]

The idea of incorporating nanocarbons between the perovskite layer and mesoporous semiconducting oxide layer was first initiated by Snaith's group by applying a C_{60}SAM upon the mesoporous TiO_2 layer, as shown in Figure 1.22.[92] They found that a fullerene self-assembled monolayer (C_{60}SAM) acts as a very effective electron acceptor from both the perovskite and polyhexathiophene (P3HT) polymer. It is also worth noting that in the presence of the C_{60}SAM, direct electron transfer from the perovskite to the TiO_2 is partially blocked and thus resulted in an improved V_{oc}. This inhibition of electron transfer to the TiO_2 was associated with the energy levels of the components (see inset of Figure 1.22) and poor electronic coupling. The charge transport of the TiO_2 was enhanced 4–5 times after the incorporation of the C_{60}SAM, and the doped devices exhibited an energy conversion efficiency of 6.7%, which was nearly 2 times higher than that obtained by the benchmark cell.

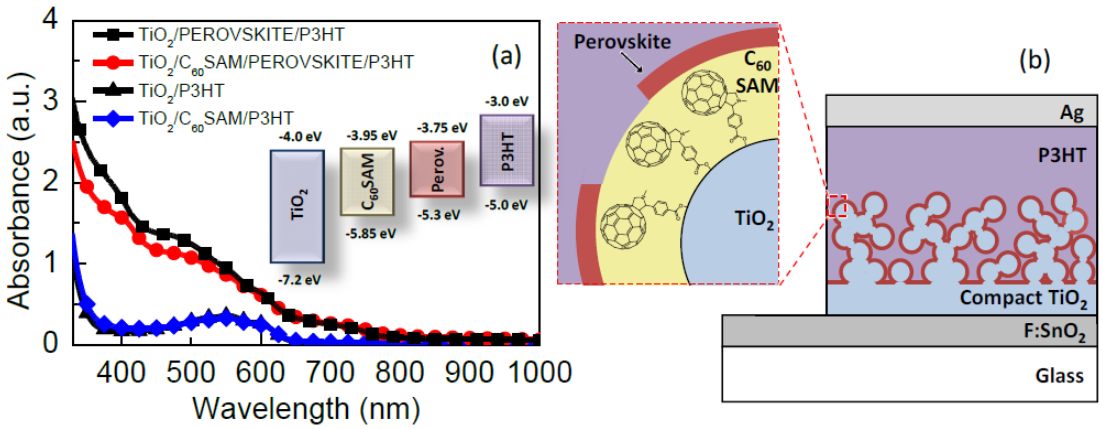

Figure 1.22 (a) Absorption spectra of P3HT and perovskite films with and without C_{60}SAM fullerene functionalization. Inset: Energy levels of the system components relative to vacuum. (b) Schematic of the device structure. Adapted from Ref. [92].

Zhu *et al.* who synthesized single/few layer graphene quantum dots (GQDs) using an electrochemical method and inserted them between the layers of perovskite and TiO_2 nanoparticles.[88]

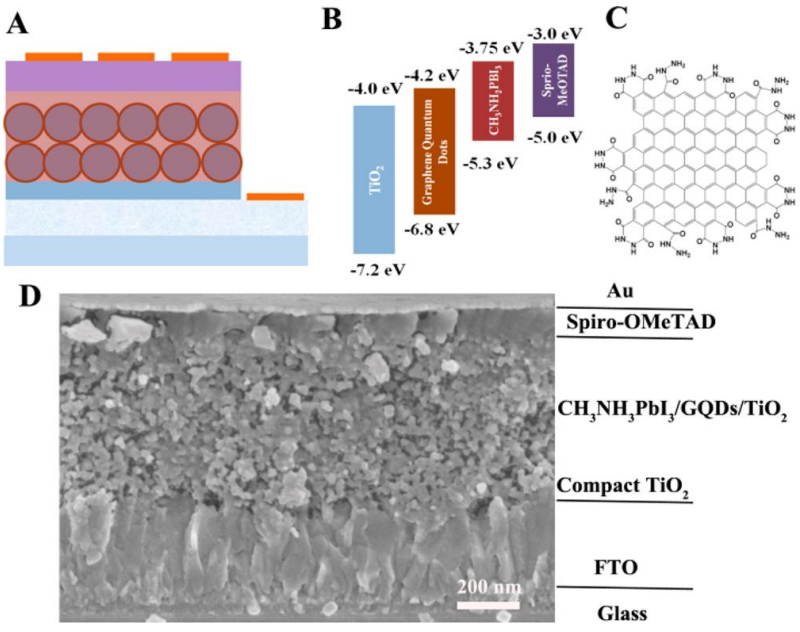

Figure 1.23 Schematic representation of the typical full device structure (A); the energy band alignment relative to vacuum (B); the edge-modified GQD structure determined by theoretical calculation (C); crosssectional SEM image of a complete device based on the $CH_3NH_3PbI_3$/GQDs/TiO_2 structure (D). Adapted from Ref. [88].

In their PSCs, the GQDs were proposed to serve as a bridge to facilitate electron injection from the perovskite to the TiO_2 conduction band. However, as shown in Figure 1.23, the conduction band of the GQD (-4.2 eV) is lower than that of the TiO_2 (-4.0 eV).

If these energy levels are correct, it is not “downhill” in energy from the perovskite to the GQD to the TiO_2 and hence rapid electron transfer would not seem feasible. However, the final PSC fabricated based on GQDs (Fig. 8c) exhibited a high PCE of 10.15% which was considerably higher than that of GQDs-free cell (8.81%). The authors showed that this significant improvement in the cell performance was associated with the much faster electron injection when GQDs are inserted in the cells. The injection time of electrons from the perovskite to the TiO_2 conduction band was measured to be 260–307 ps using transient absorption spectroscopy. A significant improvement in the electron injection time (90–106 ps) was observed after adding GQDs between the perovskite and TiO_2 layers. Although the insertion of GQDs between the perovskite and TiO_2 layers of PSCs has brought a significant improvement in the device efficiency, the mechanism for this efficiency enhancement clearly needed to be investigated further. In addition, controlling the band gap structure of GQDs for effective electron injection would be a promising future research direction and likely to further improve efficiency of GQDs enhanced PSCs.

d) Carbon materials in the blocking layer

The blocking layer (or compact layer) is of particular importance and mandatory for PSCs. It is essential to ensure that the blocking layer is pinhole-free and should be uniformly deposited, so that it can prevent charge recombination between the FTO and perovskite or FTO and HTM.

Recently, Wang et al.[93] developed low-temperature processed graphene/TiO_2 nanocomposites and employed them as the blocking layers in PSCs, as shown in Figure 1.24.

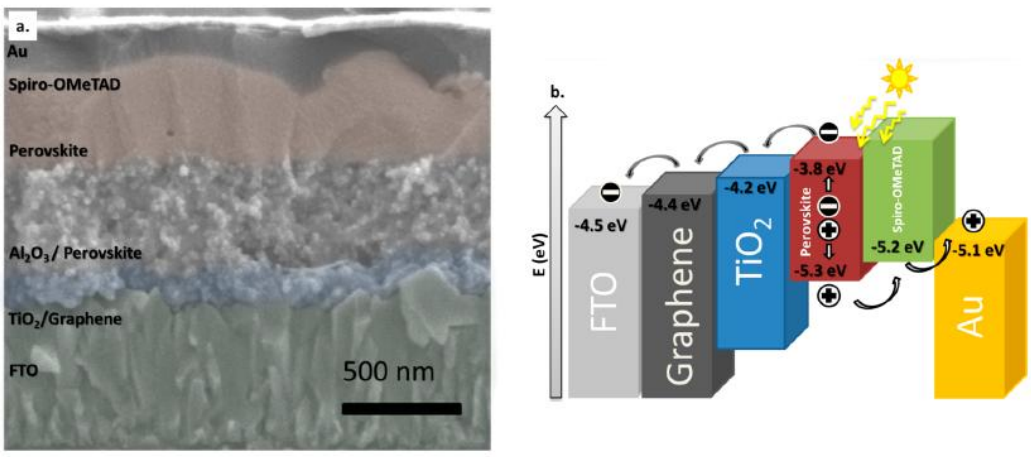

Figure 1.24 (a) Cross-sectional SEM micrographs showing a general schematic of the solar cell architecture. (b) Schematic illustration of energy levels of the materials used. Adapted from Ref [93].

It was demonstrated that the application of graphene in TiO_2 blocking layer has advantage of not only eliminating the high-temperature processing, it also minimises the series resistance of cells significantly. In the graphene/TiO_2 nanocomposite structure, graphene facilitated a rapid electron transfer within the network and thus suppressed the charge recombination because graphene possesses excellent electrical conductivity. The graphene/TiO_2 nanocomposite blocking layer based PSCs achieved very high energy conversion efficiency of 15.6%, which was significantly higher than that (10.0%) obtained by the cell fabricated with the TiO_2 only layer. Moreover, the energy level of graphene is ideal (see Figure 1.24) for the PSCs as its work function sits between the TiO_2 conduction band and FTO and so that the electrons transfer stepwise from the TiO_2 to FTO without an energy barrier.

1.3 Objectives

This thesis was devoted to the development of novel metal-free carbon catalysts for sustainable catalysis and to the development of carbon-doped perovskite solar cells. In the catalysis framework, modified MWCNTs and graphene flakes were used as catalysts in selective oxidation, and heteroatom-doped MWCNTs and graphene flakes were tested as reduction catalysts. In the perosvskite solar cells framework, graphene flakes were used as dopants in ETL and in the HTL.

The main objectives of the work were:

(i) to evaluate the effect of the different surface modifications on the carbon materials catalytic performance in the selective oxidation of *cis*-cyclooctene;

(ii) to investigate the effect of the different heteroatoms doping procedures on the catalytic properties of the carbon nanomaterials in the reduction of 4-nitrophenol;

(iii) to explore the potentialities of graphene flakes as dopants for perovskite-based solar cells and the effect of different incorporation architectures;

Figure 1.25 illustrates the bridging role of the carbon materials within the two framewoks of this thesis, as their versatility allows for the enrichment of two so distinct areas of materials science, so very important in the pursuit of a sustainable world. Multi-walled carbon nanotubes and graphene flakes were considered as key materials as their remarkable properties have already proven to be very useful for catalysis. Graphene flakes were considered for solar electricity generation based on their

enduring promise to revolutionize several electrochemical systems, as in the 3rd generation solar cells.

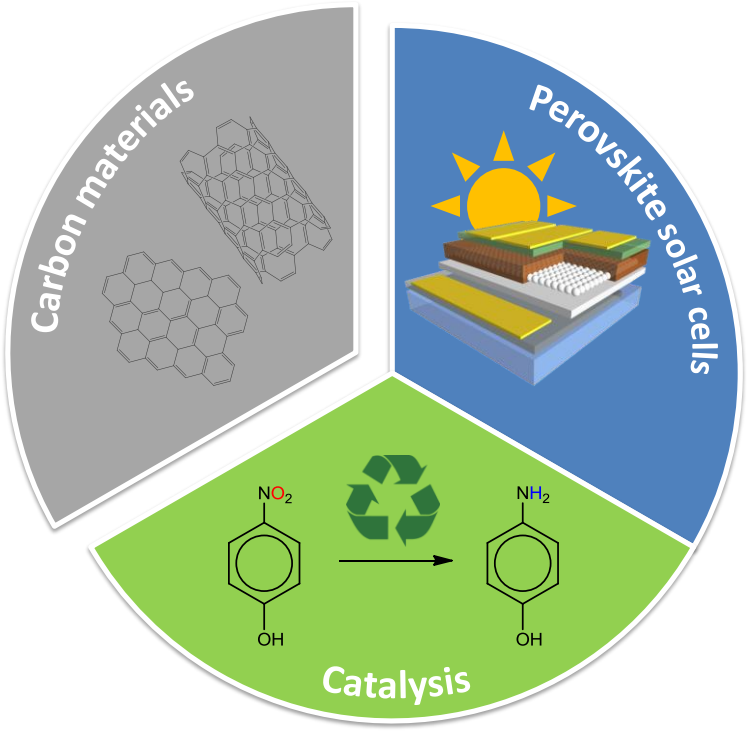

Figure 1.25 Carbon materials used in the framework of this thesis: catalysis and perovskite-based solar cells.

Apart from **Chapter 1**, which aims at giving an overall introduction on the reported themes, the thesis is divided into more 4 chapters.

Chapter 2 comprises the preparation and characterization of modified MWCNT and GF materials and the evaluation of their catalytic performance on the selective oxidation of cis-cyclooctene.

Chapter 3 corresponds to the preparation and characterization of heteroatom-doped MWCNT and GF materials and the evaluation of their catalytic performance on the reduction of 4-nitrophenol.

Chapter 4 relates to the assemblage and characterization of pristine and GF-doped perovskite solar cells.

Chapter 5 describes the overall conclusions and future perspectives.

The thesis also includes the Appendices A and B, in which some additional data and the experimental details on the most commom characterization techniques are described.

References

[1] A. Krueger, *Carbon Materials and Nanotechnology*, Wiley, **2010**.

[2] H. W. Kroto, J. R. Heath, S. C. O'Brien, R. F. Curl, R. E. Smalley, *Nature* **1985**, *318*, 162–163.

[3] S. Iijima, *Nature* **1991**, *354*, 56–58.

[4] K. S. Novoselov, A. K. Geim, S. V. Morozov, D. Jiang, Y. Zhang, S. V. Dubonos, I. V. Grigorieva, A. A. Firsov, *Science* **2004**, *306*, 666–669.

[5] P. Serp, J. L. Figueiredo, *Carbon Materials for Catalysis*, John Wiley & Sons, **2008**.

[6] J. Emsley, *Nature's Building Blocks : An A-Z Guide to the Elements*, Oxford University Press, **2011**.

[7] J. M. Chem, J. Prasek, J. Drbohlavova, J. Chomoucka, J. Hubalek, O. Jasek, R. Kizek, *J. Mater. Chem.* **2011**, *21*, 15872–15884.

[8] O. Lee, J. Jung, S. Doo, S. Kim, T. Noh, *Met. Mater. Int.* **2010**, *16*, 663–667.

[9] G. Overney, W. Zhong, D. Tom, *Z. Phys. D* **1993**, *27*, 93–96.

[10] A. G. Rinzler, J. H. Hafner, P. Nikolaev, L. Lou, S. G. Kim, D. Tomanek, P. Nordlander, D. T. Colbert, R. E. Smalley, *Science* **1995**, *269*, 1550–1553.

[11] G. Che, B. B. Lakshmi, E. R. Fisher, C. R. Martin, *Nature* **1998**, *393*, 346–349.

[12] B. Gao, A. Kleinhammes, X. P. Tang, C. Bower, L. Fleming, Y. Wu, *Chem. Phys. Lett.* **1999**, *307*, 153–157.

[13] A. C. Dillon, K. M. Jones, T. A. Bekkedahi, C. H. Kiang, D. S. Bethune, M. J. Heben, *Nature* **1997**, *386*, 377–379.

[14] A. Bachtold, A. Bachtold, P. Hadley, T. Nakanishi, C. Dekker, *Science* **2001**, *294*, 1317–1320.

[15] R. F. Curl, S. H. W. Kroto, A. Geim, P. Wallace, *Surf. Sci.* **2011**, *605*, 1607–1610.

[16] A. K. Geim, K. S. Novoselov, *Nat. Mat.* **2007**, *6*, 183–192.

[17] C. Lee, X. Wei, J. W. Kysar, J. Hone, *Science* **2008**, *321*, 385–388.

[18] A. A. Balandin, S. Ghosh, W. Bao, I. Calizo, D. Teweldebrhan, F. Miao, C. N. Lau, *Nano Lett.* **2008**, *8*, 902–907.

[19] K. I. Bolotin, K. J. Sikes, Z. Jiang, M. Klima, G. Fudenberg, J. Hone, P. Kim, H. L. Stormer, *Solid State Commun.* **2008**, *146*, 351–355.

[20] M. D. Stoller, S. Park, Y. Zhu, J. An, R. S. Ruoff, *Nano Lett.* **2008**, *8*, 3498–3502.

[21] Y. Zhang, Y. Tan, H. L. Stormer, P. Kim, *Nature* **2005**, *438*, 201–204.

[22] J. Wintterlin, M. Bocquet, *Surf. Sci.* **2009**, *603*, 1841–1852.

[23] K. S. Kim, Y. Zhao, H. Jang, S. Y. Lee, J. M. Kim, K. S. Kim, J. Ahn, P. Kim, J. Choi, B. H. Hong, *Nature* **2008**, *457*, 706–710.

[24] R. K. Singh, R. Kumar, D. P. Singh, *RSC Adv.* **2016**, *6*, 64993–65011.

[25] H. Bai, C. Li, G. Shi, *Adv. Mater.* **2011**, *23*, 1089–1115.

[26] Y. Hernandez, V. Nicolosi, M. Lotya, F. M. Blighe, Z. Sun, S. De, I. T. McGovern, B. Holland, M. Byrne, Y. K. Gun'Ko, et al., *Nat. Nanotechnol.* **2008**, *3*, 563–568.

[27] C. Valle, C. Drummond, H. Saadaoui, C. A. Furtado, M. He, O. Roubeau, L. Ortolani, M. Monthioux, A. Pe, *J. Am. Chem. Soc.* **2008**, *130*, 15802–15804.

[28] N. Behabtu, J. R. Lomeda, M. J. Green, A. L. Higginbotham, A. Sinitskii, D. V Kosynkin, D.

Tsentalovich, A. N. G. Parra-vasquez, J. Schmidt, E. Kesselman, et al., *Nat. Nanotechnol.* **2010**, *5*, 406–411.

[29] B. Luo, S. Liu, L. Zhi, *Small* **2012**, *8*, 630–646.

[30] A. J. Hunt, A. S. Matharu, A. H. King, J. H. Clark, *Green Chem.* **2015**, *17*, 1949–1950.

[31] D. S. Su; J. Zhang; B. Frank; A. Thomas; X. Wang; J. Paraknowitsch; R. Schlögl, *ChemSusChem* **2010**, *3*, 169–180.

[32] Y. Suzuki, M. Matsushima, M. Kodomari, *Chem. Lett.* **1998**, *27*, 319–320.

[33] M. Kodomari, Y. Suzuki, K. Yoshida, *Chem. Commun.* **1997**, 1567–1568.

[34] G. A. Sereda, V. B. Rajpara, R. L. Slaba, *Tetrahedron* **2007**, *63*, 8351–8357.

[35] P. Serp, M. Corrias, P. Kalck, *App. Catal. A* **2003**, *253*, 337–358.

[36] N. F. Goldshleger, *Fuller. Sci. Technol.* **2001**, 255–280.

[37] B. Li, Z. Xu, *J. Am. Chem. Soc.* **2009**, *131*, 16380–16382.

[38] S. Sarkar, S. Niyogi, E. Bekyarova, R. C. Haddon, *Chem. Sci.* **2011**, *2*, 1326–1333.

[39] J. L. Figueiredo, M. F. R. Pereira, M. M. A. Freitas, J. J. M. Orfao, *Carbon* **1999**, *37*, 1379–1389.

[40] U. N. Maiti, W. J. Lee, J. M. Lee, Y. Oh, J. Y. Kim, J. E. Kim, *Adv. Mater.* **2014**, *26*, 40–67.

[41] X. Wang, G. Sun, P. Routh, D. Kim, W. Huang, P. Chen, *Chem. Soc. Rev.* **2014**, *43*, 7067–7098.

[42] I. F. Silva, J. Vital, A. M. Ramos, H. Valente, A. M. Botelho do Rego, M. J. Reis, *Carbon* **1998**, *36*, 1159–1165.

[43] D. R. Dreyer, H. Jia, C. W. Bielawski, *Angew. Chem. Int. Ed.* **2010**, *49*, 6813–6816.

[44] H. Jia, D. R. Dreyer, C. W. Bielawski, *Tetrahedron* **2011**, *67*, 4431–4434.

[45] J. Yang, G. Sun, Y. Gao, H. Zhao, P. Tang, J. Tan, A. Lu, D. Ma, *Energy Environ. Sci.* **2013**, *6*, 793–798.

[46] S. Song, H. Yang, R. Rao, H. Liu, A. Zhang, *Catal. Commun.* **2010**, *11*, 783–787.

[47] Y. Cao, H. Yu, F. Peng, H. Wang, *ACS Catal.* **2014**, *4*, 1617–1625.

[48] Y. Cao, H. Yu, J. Tan, F. Peng, H. Wang, J. Li, *Carbon* **2013**, *57*, 433–442.

[49] J. Luo, F. Peng, H. Wang, H. Yu, *Catal. Commun.* **2013**, *39*, 44–49.

[50] J. Long, X. Xie, J. Xu, Q. Gu, L. Chen, X. Wang, *ACS Catal.* **2012**, *2*, 622–631.

[51] Y. Gao, D. Ma, C. Wang, J. Guan, X. Bao, *Chem. Commun.* **2011**, *47*, 2432–2434.

[52] X. Kong, Q. Chen, Z. Lun, *J. Mater. Chem. A* **2014**, *2*, 610–613.

[53] X. Kong, Z. Sun, M. Chen, C. Chen, Q. Chen, *Energy Environ. Sci.* **2013**, *6*, 3260–3266.

[54] K. Gong, F. Du, Z. Xia, M. Durstock, L. Dai, *Science* **2009**, *323*, 760–764.

[55] X. Liu, L. Dai, *Nat. Rev. Mater.* **2016**, 1–12.

[56] N. Oreskes, *Science* **2005**, *306*, 1686.

[57] T. W. Hamann, R. A. Jensen, A. B. F. Martinson, V. Ryswyk, J. T. Hupp, T. Hamann, *Energy Environ. Sci.* **2008**, *1*, 66–78.

[58] M. Grätzel, *J. Photoch. Photobiol. C* **2003**, *4*, 145–153.

[59] K. Nazeeruddin, E. Baranoff, M. Gra, *Sol. Energy* **2011**, *85*, 1172–1178.

[60] B. O'Regan, M. Grätzel, *Nature* **1991**, *353*, 737–740.

[61] E. Becquerel, *C. R. Acad. Sci. Paris* **1839**, *9*, 561–567.

[62] W. Smith, *Nature* **1873**, *7*, 303.

[63] W. G. Adams, R. E. Day, *Proc. R. Soc. Lond. A* **1877**, *25*, 113–117.

[64] A. Einstein, *Ann. Phys.* **1905**, *17*, 132–148.

[65] Z. Czochralski, *Phys. Chem.* **1918**, *92*, 219–221.

[66] J. Nelson, *The Physics of Solar Cells*, Imperial College Press, London, **2007**.

[67] S. D. Stranks, G. E. Eperon, G. Grancini, C. Menelaou, M. J. P. Alcocer, T. Leijtens, L. M. Herz, A. Petrozza, H. J. Snaith, *Science* **2013**, *342*, 341–344.

[68] H. Kim, S. H. Im, N. Park, *J. Phys. Chem. C* **2014**, *118*, 5615–5625.

[69] Y. Zhou, K. Zhu, *ACS Energy Lett.* **2016**, *1*, 64–67.

[70] A. Kojima, K. Teshima, Y. Shirai, T. Miyasaka, *J. Am. Chem. Soc.* **2009**, *131*, 6050–6051.

[71] H. Kim, C. Lee, J. Im, K. Lee, T. Moehl, A. Marchioro, S. Moon, R. Humphry-baker, J. Yum, J. E. Moser, et al., *Sci. Rep.* **2012**, *2*, 591.

[72] J. Burschka, N. Pellet, S.-J. Moon, R. Humphry-Baker, P. Gao, M. K. Nazeeruddin, M. Grätzel, *Nature* **2013**, *499*, 316–320.

[73] M. Liu, M. B. Johnston, H. J. Snaith, *Nature* **2013**, *501*, 395–398.

[74] S. Ahmad, P. S. Cells, S. Kazim, M. K. Nazeeruddin, M. Grätzel, S. Ahmad, *Ang. Chem. Int. Ed.* **2014**, *53*, 2812–2824.

[75] Z. Cheng, J. Lin, *Cryst. Eng. Comm.* **2010**, *12*, 2646–2662.

[76] A. Kojima, M. Ikegami, K. Teshima, T. Miyasaka, *Chem. Lett.* **2012**, *41*, 397–399.

[77] C. R. Kagan, C. R. Kagan, D. B. Mitzi, C. D. Dimitrakopoulos, **1999**, *286*, 945–947.

[78] J. Im, C. Lee, J. Lee, S. Park, N. Park, *Nanoscale* **2011**, *3*, 4088–4093.

[79] J. Im, J. Chung, S. Kim, N. Park, *Nanoscale Res. Lett.* **2012**, *7*, 353.

[80] W. Li, J. Li, L. Wang, G. Niu, R. Gao, Y. Qiu, *J. Mater. Chem. A* **2013**, *1*, 11735–11740.

[81] M. M. Lee, J. Teuscher, T. Miyasaka, T. N. Murakami, H. J. Snaith, **2012**, *338*, 643–647.

[82] M. A. Green, K. Emery, Y. Hishikawa, W. Warta, E. D. Dunlop, *Progr. Photovoltaics* **2014**, *22*, 701–710.

[83] Z. Ku, Y. Rong, M. Xu, T. Liu, H. Han, *Sci. Rep.* **2013**, *3*, 3132.

[84] A. Mei, X. Li, L. Liu, Z. Ku, T. Liu, Y. Rong, M. Xu, M. Hu, J. Chen, Y. Yang, et al., *Science* **2014**, *345*, 295–298.

[85] Z. Li, S. A. Kulkarni, P. P. Boix, E. Shi, A. Cao, K. Fu, K. Sudip, J. Zhang, Q. Xiong, L. H. Wong, et al., *ACS Nano* **2014**, *8*, 6797–6804.

[86] S. N. Habisreutinger, T. Leijtens, G. E. Eperon, S. D. Stranks, R. J. Nicholas, H. J. Snaith, *Nano Lett.* **2014**, *14*, 5561–5568.

[87] Q. Luo, Y. Zhang, C. Liu, J. Li, H. Lin, *J. Mater. Chem. A* **2015**, *3*, 15996–16004.

[88] Z. Zhu, J. Ma, Z. Wang, C. Mu, Z. Fan, L. Du, Y. Bai, L. Fan, H. Yan, D. L. Phillips, et al., *J. Am. Chem. Soc.* **2014**, *136*, 3760–3763.

[89] G. Xing, N. Mathews, S. Sun, S. S. Lim, Y. M. Lam, M. Grätzel, S. Mhaisalkar, T. C. Sum, *Science*

2014, *342*, 344–347.

[90] K. J. Williams, C. A. Nelson, X. Yan, L. Li, X. Zhu, *ACS Energy Lett.* **2013**, 1388–1394.

[91] Z. Zhang, J. Zhang, N. Chen, L. Qu, *Energy Environ. Sci.* **2012**, *5*, 8869–8890.

[92] A. Abrusci, S. D. Stranks, P. Docampo, H. Yip, A. K. Jen, H. J. Snaith, *Nano Lett.* **2013**, *13*, 3124–3128.

[93] J. T. Wang, J. M. Ball, E. M. Barea, A. Abate, J. A. Alexander-Webber, J. Huang, M. Saliba, R. J. Nicholas, *Nano Lett.* **2013**, *14*, 724–730.

Chapter 2

Modified carbocatalysts for the selective oxidation of *cis*-cyclooctene

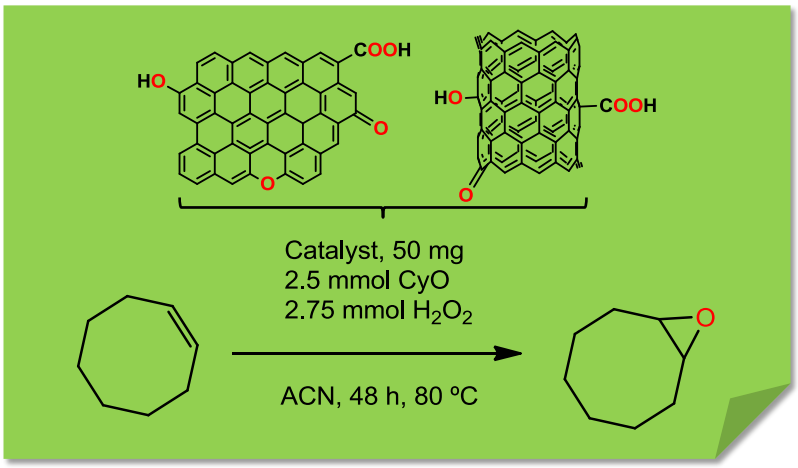

2

Modified carbocatalysts for the selective oxidation of *cis*-cyclooctene

Abstract

In this Chapter, it is described the modification and characterization of multi-walled carbon nanotubes and graphene flakes through three different oxidation procedures: (i) nitric acid treatment; (ii) nitric acid followed by thermal treatment at 400 ˚C; (iii) gas phase oxidation with O_2. The oxidised materials showed an overall increase in the oxygen content and revealed that the different oxidation procedures promoted different superficial chemical compositions: nitric acid treated materials MWCNTh and GFh, presented increased amounts of carboxylic acids, anhydrides and phenols; materials MWCNTht and GFht, treated with nitric acid followed by thermal treatment at 400 ˚C, presented a loss of carboxylic acids and an increase in carboxylic anhydrides content; and finally the gas phase treated materials MWCNTo and GFo presented an increase in the amounts of phenols, carbonyls/quinones, and lactones. The oxidation procedures promoted an increase in the carbon nanotube materials surface area, while the graphene flake materials presented lower surface areas upon the oxidation procedures, suggesting a higher degree of agglomeration. An overall increase in the materials disorder through the introduction of defects onto their original structure was also observed.

The catalytic studies showed that all the materials were active catalysts in the selective oxidation of *cis*-cyclooctene and that the modifications introduced in the pristine materials, through nitric acid followed by thermal treatment at 400 ˚C, originated catalysts with superior activity and selectivity: material MWCNTht presented a 47% conversion and 79% selectivity and material GFht showed a 57% coversion and 85% selectivity. Reusability experiments revealed no loss of catalytic activity up to three catalytic cycles. The results indicate that the fine tuning of the carbon materials through appropriate oxidation procedures, is crucial in achieving metal-free carbocatalysts with enhanced performance and selectivity.

2.1 Introduction

Epoxide formation is a central reaction in the oxyfunctionalization of many molecules and is of great importance in the present era of increasing industrial production demands, due to the versatility of epoxides as intermediates in synthesis.[1] For example, it has been reported that 4.5 million tons of propylene oxide and 70000 tons of butene oxide are produced yearly.[2] The established catalytic processes used in chemical industries use metals, in many cases noble metals, or metal oxides as catalysts, which are often expensive, difficult to remove, toxic, and are frequently obtained from limited natural resources.[3] Among the oxidation of alkenes, the selective oxidation of cyclooctene is of major relevance. Recently, various types of heterogeneous catalysts have been used to improve the catalytic ability for the selective oxidation of cyclooctene, including Au/C,[4] Au/graphite,[5] mesoporous mixed oxides (Ga, Ga–Nb and Ga–Mo)[6], CuO/mesoporous SiO_2 nanocomposites[7], and sandwich-type polyoxometallates with various transition metals in the central belts (Ni,Co, Mn, Zn, Fe).[8] Despite these efforts, the search for a catalyst that combines the toxicological benefits of a metal-free synthesis with the convenience of heterogeneous workup, whilst retaining high activity and selectivity, is of critical importance.

In the quest for a system that can satisfy such demands, carbon materials appear as excellent candidates, given their elemental natural abundance and the fact that organic chemistry can provide the tools to modify their reactivity. Traditionally, carbon materials have been used as supports for catalysts in heterogeneous catalytic processes, although their use as catalysts on their own is becoming more and more common, earning them the term “carbocatalysts”.[9] These carbocatalyst have proved to be efficient in a wide variety of reactions, which are beyond the scope of this work. Among the large variety of carbon materials, in this work we will focus on multi-walled carbon nanotubes and graphene flakes. Specifically regarding oxidation of alkenes, it is worth mentioning the work by Yu *et al.*, which demonstrated that multi-walled carbon nanotubes can be used as a metal-free catalyst for the aerobic oxidation of cyclohexene,[10] and the pioneer work by Bielawski *et al.*, which demonstrated the efficient oxidation of various alcohols and *cis*-stilbene, and the hydration of various alkynes, catalyzed by graphene oxide (GO).[11]

Pristine MWCNT and graphene are not very reactive as the active sites are found essencially at the edges of the nanotubes or graphene layers. The introduction of oxygen functional groups by oxidative treatments, in either gas- or liquid-phase, can increase the number of active sites in various reactions. The concentration and type of

surface groups plays a very important role on determining the surface chemistry of the carbon materials.

Herein, we report the modification of commercial multi-walled carbon nanotubes and graphene flakes, through different oxidation procedures, in order to produce materials with distinct surface chemistry, and to further understand how their chemistry affects their performance as mild and efficient catalysts for the selective oxidation of *cis*-cyclooctene. Furthermore, we use hydrogen peroxide as the oxidant in the catalytic system, which is a great advantage to the environment and industry because of the simplicity in handling, the environmental friendliness with water generation as a solo by-product, the high content of active oxygen species and the cheapness compared to organic peroxides and peracids.[12]

2.2 Experimental section

2.2.1 Materials and solvents

All the reagents and solvents used during the experimental execution of this work were used without further purification. Multi-walled carbon nanotubes (MWCNT) were commercially obtained from Nanocyl S.A., Ref. 3100 MWCNT (>95 % carbon purity; 9.5 nm average diameter). Commercial graphene flakes (sample denoted as GF) was from Graphene Technologies (Lot #GTX-7/6-10.4.13). *Cis*-cyclooctene (95 %), chlorobenzene (99.5 %), and hydrogen peroxide solution (30 % w/w) were from Sigma-Aldrich. Nitric acid (65 %) was from Merck, and acetonitrile (HPLC grade) was from Fisher Scientific. Gases used in the modification of the carbon materials were from Air Liquid: N_2 (99.999 %) and air (99,999 %).

2.2.2 Preparation of the modified carbocatalysts

The pristine multi-walled carbon nanotubes (MWCNT) and graphene flakes (GF) were submitted to three different treatments – acid oxidation, acid oxidation followed by thermal treatment at 400 ˚C and oxidation in the gas phase (5 % O_2/N_2) at 500 ˚C – described as follows and shown on Fig. 2.1. (i) *Oxidation with HNO_3:* About 3 g of MWCNT or GF were refluxed in HNO_3 7 M (150 cm^3) for 3 h, washed with distilled water to neutral pH, dried in an oven at 110 ˚C for 24 h and stored in a desiccator for later use (MWCNTh or GFh). (ii) *Thermal treatment:* About 1.5 g of MWCNTh or GFh were subsequently heated to 400 ˚C at 5 ˚C/min in a fused-silica tubular reactor, under nitrogen flow (100 cm^3 min^{-1}), and kept at this temperature for 1 h. The resulting materials (MWCNTht or GFht) were cooled to room temperature under the same atmosphere and stored in a desiccator.

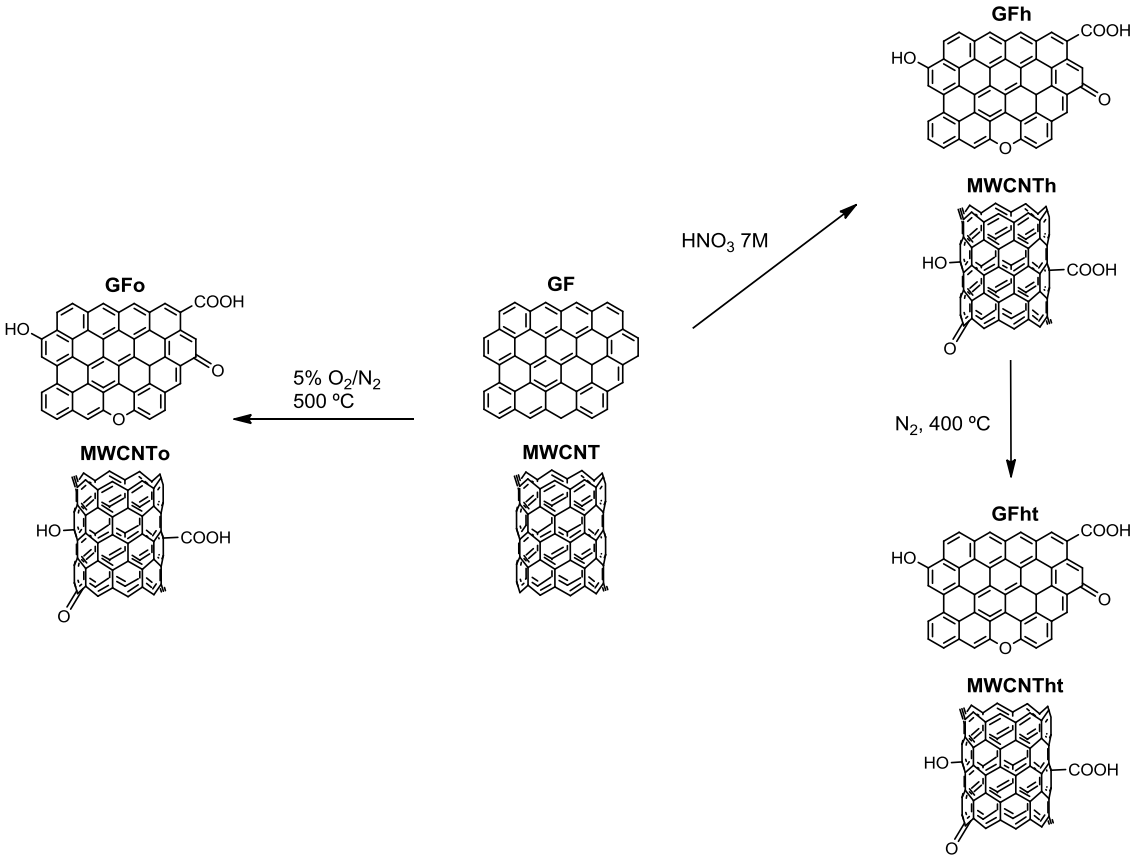

Figure 2.1 Schematic representation of the oxidation procedures.

(iii) *Gas phase oxidation:* About 1.5 g of MWCNT or GF were oxidised at 500 ˚C (5 ˚C/min) under a 5% O_2/N_2 atmosphere (100 cm^3 min^{-1}), for 3 h in a fused-silica reactor, cooled to room temperature under nitrogen atmosphere and stored in a desiccator (MWCNTo or GFo).

2.2.3 Physico-chemical characterization of the modified carbocatalysts

Fourier transform infrared spectroscopy (FTIR) spectra of the compounds were collected with a Jasco FT/IR-460 Plus spectrophotometer in the range 400–4000 cm^{-1}, using a resolution of 4 cm^{-1} and 32 scans. The spectra of the dried samples were obtained in KBr pellets (Merck, spectroscopic grade) containing 0.04 wt. % of carbon material.

The Raman spectra were measured directly on the materials using a Labram Dilor–Jobin-Yvon–Spex spectrometer, with the monochromatic green light at 532 nm of the Nd:YAG laser as the excitation source, at a power of 25 mW. The excitation laser frequency was maintained for all measurements, as the D band is a resonant mode and exhibits dispersive behavior, hence both its position and shape can vary with different excitation laser frequencies. A density filter at 75% was used to avoid thermal

decomposition of samples by the laser. The ×50 objective lens of an Olympus optical microscope was used to focus the laser beam on the sample and to collect the scattered radiation. A highly sensitive CCD camera was used to collect the Raman spectra. Each Raman spectrum presented in this study corresponds to the accumulation of 10 spectra recorded from 1000 to 3400 cm^{-1} over 10 s.

Textural characterization of the samples was carried out by N_2 adsorption–desorption at -196 ˚C in a Quantachrome NOVA 4200e apparatus. The apparent surface area (S_{BET}) was determined by applying the Brunauer–Emmett–Teller (BET) equation.[13]

X-ray diffraction (XRD) profiles were collected at room temperature in a continuous scanning mode (step 0.02 and time 10 s) on a Rigaku D/Max-B, Cu K diffractometer in the 2θ range from 7˚ to 100˚, in a Bragg-Brentano $\theta/2\theta$ configuration. A Lorentzian deconvolution of the (002) peak observed in the carbon material XRD profiles was performed and the crystallite sizes were estimated from the Scherrer equation [$L = 0.94 \times \lambda / (\beta_{1/2} \times \cos\theta)$], where L = average crystallite size, $\beta_{1/2}$ = line broadening at FWHM in radians, θ = Bragg angle and λ = X-ray wavelength (1.544 Å), and considering the interlayer distances. The area ratio was considered to measure the percentage of layers that are stacked as crystallites composed by the corresponding number of layers and although layers with interlayer spacings larger than 3.44 Å (2θ lower than 26.1º) are non 3-D stacked, they were considered only to estimate the weighted average number of layers in the materials and should not be regarded as crystallites.

Temperature programmed desorption (TPD) was performed in an Altamira Instruments AMI-200 device. Typically, samples of 100 mg were heated at 5 ˚C min^{-1} up to 1100 ˚C, under a flow of He (25 cm^3 min^{-1}); the amounts of CO (*m/z* = 28) and CO_2 (*m/z* = 44) released from the carbon samples were monitored using a Dymaxion 200 AMU Ametek mass spectrometer.

X-ray photoelectron spectroscopy (XPS) was performed at ‘‘Centro de Materiais da Universidade do Porto’’ (CEMUP, Porto, Portugal) in a VG Scientific ESCALAB 200A spectrometer using non-monochromatised Al K_α radiation (1486.6 eV). The powdered samples were pressed into pellets prior to the XPS measurements. To correct possible deviations caused by electric charge of the samples, the C1s band at 284.6 eV was taken as internal standard.[14,15] The XPS spectra were deconvoluted with the CasaXPS software, using non-linear least squares fitting routine after a Shirley-type background subtraction. The surface atomic percentages were calculated from the

corresponding peak areas and using the sensitivity factors provided by the manufacturer.

Transmission electron microscopy (TEM) images were collected at “Universidade de Trás-os-Montes e Alto Douro”, with a Zeiss LEO 906 microscope operating at an accelerating voltage of 120 kV. The samples were dispersed in dimethylformamide under sonication, after which a carbon-coated 400 mesh copper grid was immersed in the suspension and then air-dried.

2.2.4 Catalytic studies of the modified carbocatalysts in the selective oxidation of *cis*-cyclooctene

The oxidation reaction of *cis*-cyclooctene was carried out in acetonitrile (MeCN), using a borosilicate 50 cm^3 reaction vessel, with addition of H_2O_2 (30 % w/w), in the presence of the carbon materials as heterogeneous catalysts, at 80 ˚C. In a typical experiment, *cis*-cyclooctene (2.5 mmol) was dissolved in MeCN (25 cm^3) and stirred. Afterwards, 50 mg of carbon catalyst was added. The reaction was started with the addition of 281 µL of H_2O_2 solution (2.75 mmol). The mixture was stirred at 80 ˚C for 48 hours. The reaction progress was followed by gas chromatography in a Thermo Scientific Trace 1300 gas chromatograph, equipped with a Teknokroma TRB-5 column (30 m × 0.25 mm × 0.25 µm) and a flame ionization detector (FID). The mobile phase was a mixture of air (21 % O_2 in 79% N_2) and N_2 (>99,998 %), and the detector fuel gas was hydrogen (>99,95 %). The oven temperature program was: start at 80 ˚C, 20 ˚C min^{-1}, 200 ˚C (8 min). At 24 hours intervals, an aliquot was taken directly from the reaction mixture with a hypodermic syringe (approximately 0.1 cm^3), filtered through a 0.2 µm Nylon membrane filter, and 1 µL was injected into the chromatograph, with a 10 µL microsyringe, for analysis of starting materials and products. The reaction products reported were identified by mass spectrometry coupled with gas chromatography, in a Thermo Scientific Trace 1300 chromatograph equipped with a TG-5MS Thermo Scientific column (60 m × 0.25 mm × 0.25 µm) and a MS ISQ quadrupole operating in electron ionization mode (70 eV). At the end of reactions, the catalysts were filtered, washed with MeCN several times to remove the remaining substrate, reaction products and oxidant. The recovered catalysts were dried at 100 ˚C overnight under vacuum and reused in a new reaction under identical experimental conditions, with readjustment of all quantities, without changing the molar ratios and reaction concentrations. A blank reaction without catalyst was also performed.

2.3 Results and discussion

2.3.1 Materials characterization

XPS analysis was carried out to assess the type and relative amount of functional groups on the pristine and oxidised carbon materials. The relative amounts of the different elements, C, O and N, were calculated from the corresponding peak areas and are shown in Table 2.1.

Table 2.1 XPS surface atomic percentages and C/O atomic ratios for the carbon materials.

Material	% At			C/O ratio
	C1s	O1s	N1s	
MWCNT	98.7	1.3	-	75.9
MWCNTh	94.5	5.4	0.1	17.2
MWCNTht	96.6	3.2	0.2	30.2
MWCNTo	97.4	2.6	-	37.5
GF	92.9	6.8	0.3	13.7
GFh	91.5	8.2	0.3	11.2
GFht	93.9	5.8	0.3	16.2
GFo	95.3	4.5	0.2	21.2

Pristine MWCNT is composed by 98.7 % of carbon and 1.3 % of oxygen, whereas GF is composed by 92.9 % of carbon and a considerable amount of oxygen - 6.8 % - and 0.3 % of residual N. After the oxidation treatments applied to MWCNT, the amount of oxygen increased in all the materials, with the percentage varying between the lowest value of 2.6 % for MWCNTo and the highest value of 5.4 % for MWCNTh. Material MWCNTht presents an oxygen content of 3.2 %, as it results from a thermal treatment on material MWCNTh, at 400 ˚C, under an inert atmosphere. Under these conditions several deoxygenation reactions occur, which explain this oxygen content decrease. C/O atomic ratios have considerably decreased, as a consequence of the oxygen percentage increase, for MWCNTh, MWCNTht, and MWCNTo (C/O ratios of 17.2, 30.2, 37.5 and 13.0, respectively), when compared with the C/O atomic ratio of MWCNT (C/O ratio of 75.9). As for the graphene flakes, there was a modest increase in oxygen content for material GFh (8.2 %), oxidised with nitric acid, when compared with the pristine GF (6.8 %). Subsequent oxygen amount decrease in GFht (5.8 %) follows the same trend observed for the carbon nanotubes, as the thermal treatment employed was identical. Interestingly, material GFo, oxidised in the gas phase (5 % O_2/N_2 at 500 ˚C), revealed a decrease in the oxygen content (4.5 %). C/O atomic ratios

for the oxidised graphene flakes remained close to that of the starting material GF (C/O ratio of 13.7), with material GFh showing a slight decrease (C/O ratio of 11.2), and materials GFht and GFo revealing an increase upon the different modification procedures (C/O ratios of 16.2 and 21.7, respectively). These results indicate a milder surface oxidation extent in the graphene flakes when compared to the carbon nanotubes counterparts. However, it should be taken into account the higher oxygen content of the starting material GF, which is similar to values found for reduced graphene oxides prepared by the Hummers method (6.0-13.5).[16,17]

The relative atomic percentages of carbon-based functional groups, which were determined based on the deconvolution of C1s high resolution spectra, are shown in Table 2.2, and deconvoluted C1s and O1s high resolution spectra of carbon nanotubes and graphene flakes are presented in Figures 2.2 and 2.3, respectively.

Table 2.2 Relative atomic percentages of carbon-based functional groups presented in the XPS high resolution C1s spectra.

	% C				
Material	**284.6 eV (graphitic structure)**	**286.3 eV (C-O)**	**287.4 eV (C=O)**	**288.9 eV (COOH)**	**290.3 (π-π*)**
MWCNT	74.5	5.9	2.8	1.2	15.5
MWCNTh	73.3	5.6	5.1	2.7	13.3
MWCNTht	75.3	4.6	6.7	3.2	10.2
MWCNTo	74.4	5.1	6.1	3.1	11.3
GF	75.2	6.6	4.8	0.9	12.6
GFh	74.6	6.0	5.8	3.1	10.4
GFht	75.8	5.6	6.4	3.0	9.2
GFo	75.5	5.1	6.7	2.8	9.8

The shape of the high resolution C1s spectra for all the studied materials was similar to each other, with a predominant asymmetric peak, and a smaller contribution of C in surface oxygen functional groups on the high energy side of the main peak. For the deconvolution of the C1s spectra, it has been generally taken into account an asymmetric peak for carbon atoms in polyaromatic structures, and the presence of the various types of oxygen groups. Therefore, the C1s spectra were deconvoluted into five components corresponding to graphite (284.6 eV), carbon in single C-O bonds as ethers, alcohols, phenols (286.3 eV), carbon in carbonyl groups (287.4 eV), carbon in carboxyl or ester groups (288.9 eV) and the π-π* shake-up peak (290.3 eV).[18,19]

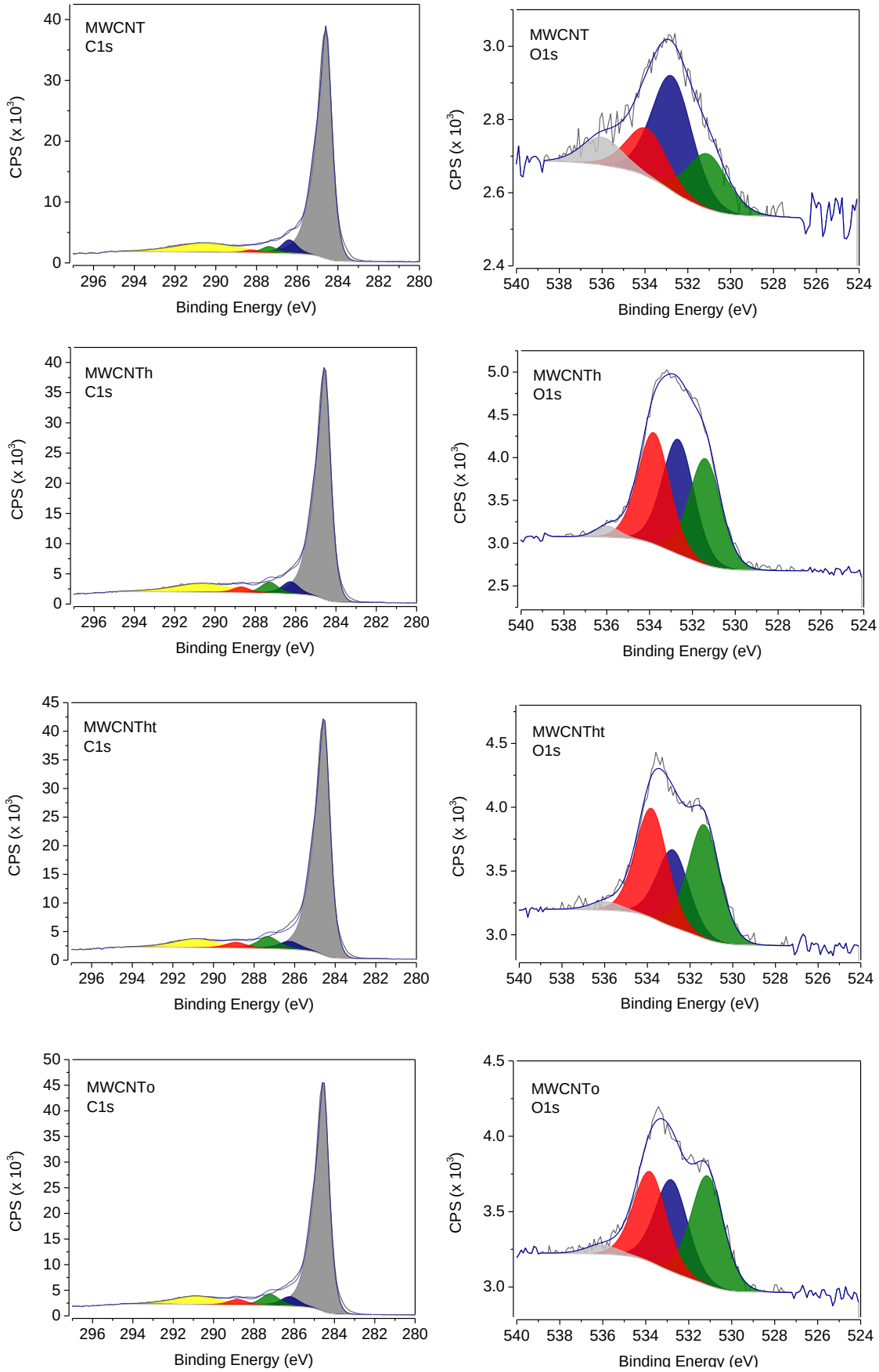

Figure 2.2 Deconvoluted C1s and O1s high resolution spectra of MWCNT materials.

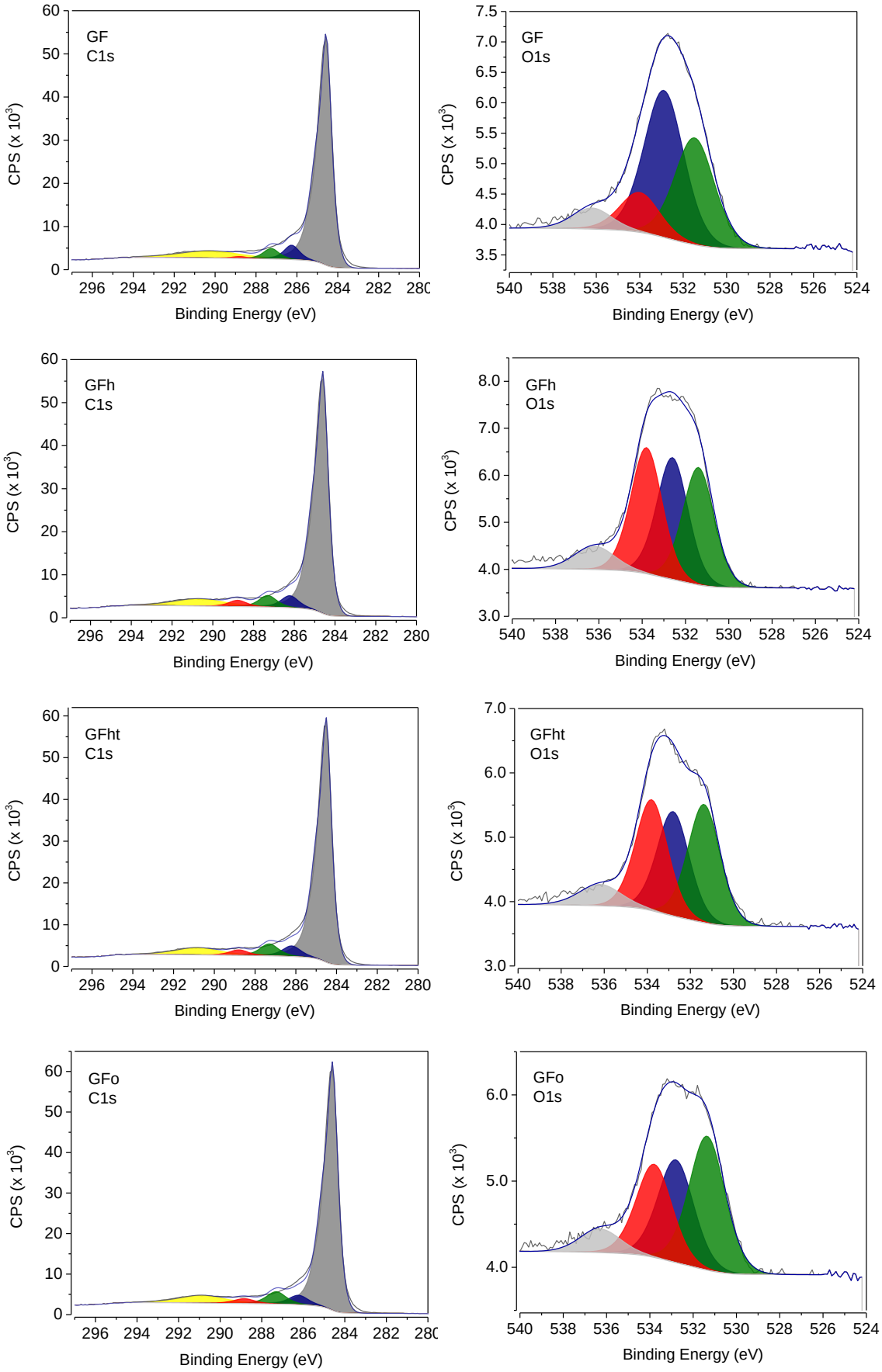

Figure 2.3 Deconvoluted C1s and O1s high resolution spectra of GF materials.

All the oxidised carbon materials presented a decrease of the π-π* satellite peak, indicating that the oxidation procedures envolved gave rise to a decrease in the electronic delocalization. In fact, there is a similar trend in both multi-walled carbon nanotubes and graphene flakes: a decrease in electronic delocalization upon nitric acid oxidation (MWCNTh and GFh), followed by a further decrease upon thermal treatment at 400 ˚C, under an inert atmosphere (MWCNTht and GFht). Inversely, the oxygen amount does not accompany this trend: while it increases upon nitric acid oxidation, after the referred thermal treatment, there is a decrease in oxygen content in both materials, indicating that the thermal treatment did not promote the rearrangement of further graphitic domains. As for the gas phase oxidised materials, MWCNTo and GFo, there is also a decrease in the electronic delocalization when compared to their pristine counterparts. These observations show that in both oxidation procedures there is a decrease in the electronic delocalization of the materials. The peaks corresponding to carbon atoms bound to oxygen (C-O, C=O, and O-C=O) present similar variations upon nitric acid oxidation for both carbon nanotubes and graphene flakes. There is an increase in the relative areas of the peaks corresponding to C=O and O-C=O, and a slight decrease in the relative area of the peak assigned to C-O, which indicates the formation of new carboxilic acids, carboxylic anhydrides, carbonyls and esters groups in MWCNTh and GFh. After the thermal treatment applied to materials MWCNTh and GFh, there is a decrease in the relative area of the peak assigned to C-O for both materials (MWCNTht and GFht), while the relative area of the peak assigned to O-C=O increases in MWCNTht and remains roughly the same in GFht. Taking into account the decrease in oxygen content observed after the thermal treatment, these results show a rearrangement of the surface oxygen functional groups relative contents. In the gas phase oxidations, a similar trend to nitric acid oxidation is observed for the both carbon nanotubes (MWCNTo) and the graphene flakes (GFo) counterpart. In these materials, there is an increase in the relative areas of the peaks assigned to C=O and O-C=O, and a decrease in the relative area of the peak due to C-O, indicating that this treatment induced the formation of new carboxilic acids, carboxylic anhydrides, carbonyls and esters groups. The relative atomic percentages of oxygen-based functional groups obtained from the deconvolution of the O1s high resolution spectra are presented in Table 2.3. The broad band in the O1s high resolution spectra was deconvoluted into four peaks in all materials:[19] a peak at 531.3 eV, assigned to O=C in ketones, quinones and aldehydes, a peak at 532.7 eV, associated to O–C from phenol and epoxy groups, a peak at 533.9 eV due to O–C=O in esters and carboxylic acids, and a peak at 536.0, assigned to oxygen atoms in water molecules. Analysis of the relative percentages of each type of oxygen types shown in Table 2.3 and in Figure 2.4

(normalized without taking into account the area of the peak atributted to water) shows an increase in the percentage of the O–C=O components, in comparison to O-C component, for all materials, revealing the significant introduction of acidic groups such as carboxylic acids, promoted by the different oxidation treatments.

Table 2.3 Relative atomic percentages of oxygen-based functional groups presented in the XPS high resolution O1s spectra.

Material	% O			
	531.3 eV (O=C)	532.7 eV (O-C)	533.9 eV (O-C=O)	536.0 eV (H-O-H)
MWCNT	22.4	46.8	19.5	11.3
MWCNTh	31.2	33.7	32.7	2.4
MWCNTht	36.9	25.0	35.4	2.7
MWCNTo	36.4	30.6	30.0	3.0
GF	34.0	46.7	12.6	6.7
GFh	29.7	30.8	31.9	7.6
GFht	32.7	28.9	30.7	7.7
GFo	37.6	28.9	26.1	7.4

The relative percentage of the O=C component for the carbon nanotube materials also show an increase upon oxidation, while for the graphene flake materials it shows a modest increase in GFo, and a slight decrease in GFh and GFht. Taking into account the O=C/O-C ratio, this indicates that the introduction of ketones, quinones and aldehyde functional groups in the carbon materials, was preferred over the formation of groups such as epoxides, hydroxyls and phenols (albeit to a greater extent in the carbon nanotube materials).

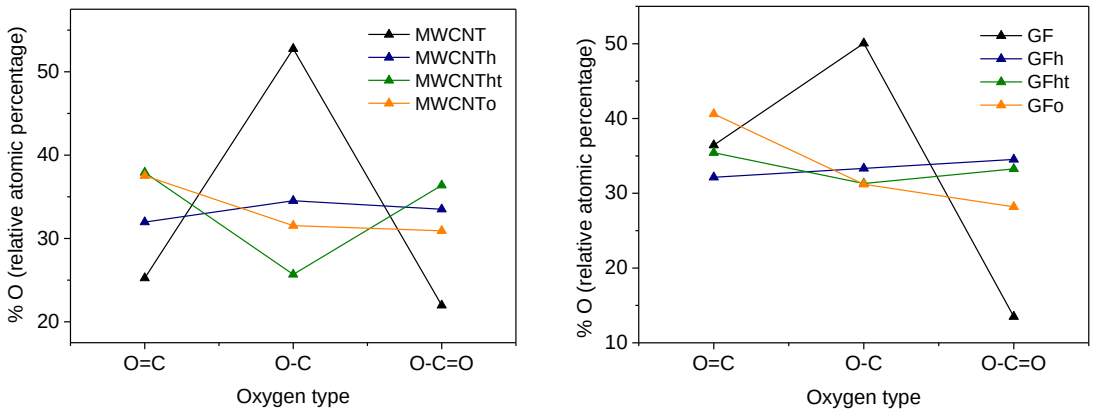

Figure 2.4 XPS relative atomic percentage of oxygen for each contribution of O1s peak components (normalized with the withdrawal of the peak assined to water molecules).

These tendencies indicate that the type and the amount of oxygen groups introduced onto the carbon surface are highly dependent on the oxidation procedure used. It is also noteworthy that the percentages depicted in Figure 2.4 follow the same tendencies for both the carbon nanotube and graphene flake materials, indicating that the oxidation procedures proceeded similarly, regardless of the nature of the initial carbon material.

TPD was used to estimate the content and nature of oxygen functional groups present in the pristine and modified carbon materials. Figure 2.5 shows the TPD profiles of carbon nanotube and graphene flake materials, and the amounts of CO_2 and CO released obtained by integration of the areas under the respective TPD profiles, together with the total mass percentage of oxygen are presented in Table 2.4.

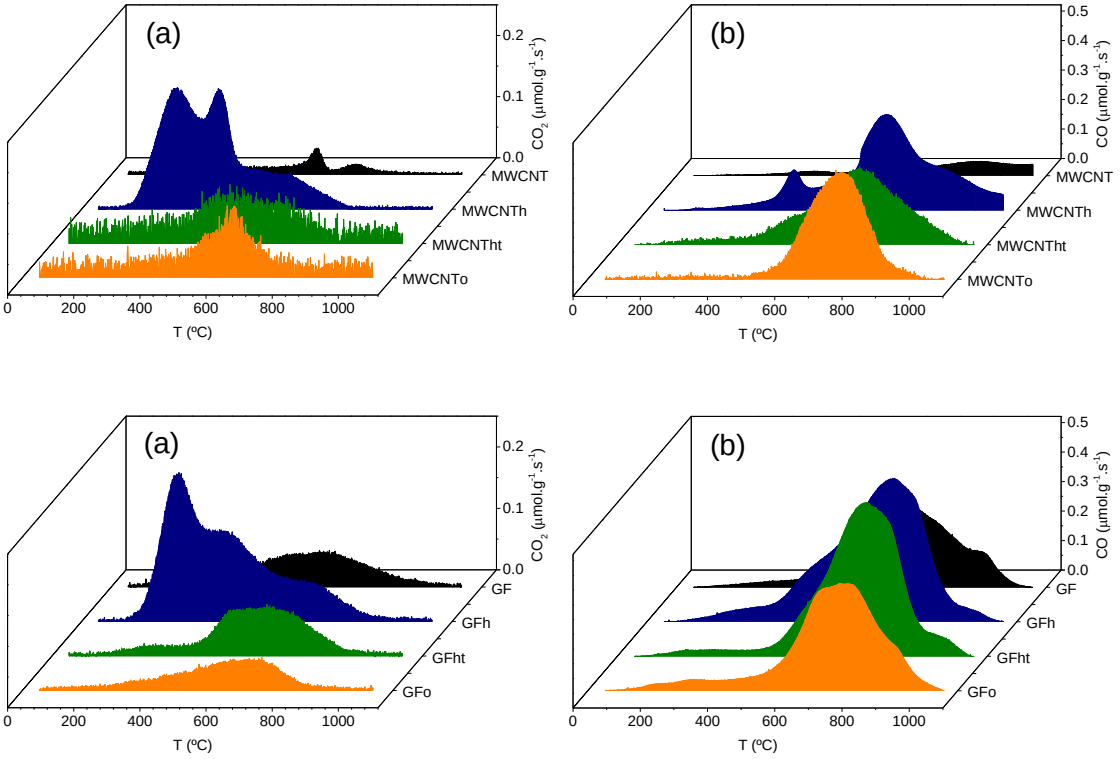

Figure 2.5 TPD profiles of carbon nanotube and graphene flake materials: (a) CO_2 evolution and (b) CO evolution.

All the carbon material TPD profiles reveal a substantial increase in the amounts of released CO_2 and CO, upon the different oxidation procedures, the only exception being the CO_2 amount released by material GFo, which released less CO_2 than pristine GF. Moreover, when comparing the total mass percentage of oxygen obtained from the integration of the TPD profiles with the percentages obtained from XPS data, one clearly indentifies the same patterns in the oxygen content variations: a large increase

upon nitric acid oxidation, followed by a subsequent decrease upon thermal treatment at 400 ˚C.

Table 2.4 Total amounts of CO_2 and CO released by TPD and total mass percentage of oxygen obtained from TPD data (assuming that all the surface oxygen is released as CO and/or CO_2).

Material	[CO_2] µmol g^{-1}	[CO] µmol g^{-1}	% O	% O (XPS)
MWCNT	108	228	0.71	1.72
MWCNTh	696	1076	4.11	7.07
MWCNTht	240	1008	2.38	4.22
MWCNTo	180	948	2.09	3.43
GF	312	1056	2.69	8.85
GFh	852	1920	5.80	10.63
GFht	336	1740	3.86	7.58
GFo	216	1380	2.90	5.90

However, for the gas phase treated materials, the TPD data shows a increase in the oxygen mass percentage for both MWCNTo and GFo materials, while the XPS data shows an increase for material MWCNTo and a decrease for material GFo. Sure enough, the oxygen mass percentages obtained from the TPD data, are all nearly halved when compared to their XPS counterparts, indicating that the location of the oxygen functional groups within the carbon materials lies preferably at the outer surfaces of the materials, e.g., at the carbon nanotube edges and outer walls and graphene flake edges and exposed basal planes. Interestingly, the TPD profiles are quite similar between the two different types of carbon materials. Nitric acid treated materials MWCNTh and GFh, clearly show two distinct peaks in the 250 – 500 ˚C region of the CO_2 TPD profile, a temperature range ascribed to the decomposition of carboxylic acid groups, corroborating the XPS results that revealed a high proportion of carboxylic acids. All the materials present peaks in the 550 – 650 ˚C and 650 – 750 ˚C regions of the CO_2 TPD profile, which are assigned to carboxylic anhydrides and lactones, respectively. In the CO TPD profiles it is possible to identify a large peak in the 700 – 800 ˚C region, assigned to the decomposition of phenol groups. It is also possible to observe two shoulders on this peak: one a lower temperatures (550 – 650 ˚C), corresponding to the decomposition of carboxylic anhydrides, and another at higher temperatures (850 – 1000 ˚C), ascribed to the decomposition of carbonyl and quinone groups. For some materials, namely MWCNT, MWCNTh, MWCNTht, and

GFh, it is possible to observe that there is a small CO evolution in the low temperature region 200 – 450 ˚C. The identification of oxygen functional groups that decompose in this temperature range is still a subject of debate. However, there is a growing consensus that the decomposition of epoxyl and hydroxyl functionalities occur in this temperature range.[19–21] In order to estimate the amount of each oxygen surface group, the deconvolution of the CO_2 and CO TPD profiles was performed. A multiple Gaussian function was used for fitting each of the TPD profiles, and the numerical calculations were based on a nonlinear routine, which minimized the square of the deviations, using the Levenberg-Marquardt method to perform the iteractions. The deconvoluted TPD profiles of the carbon nanotube materials and graphene flake materials are shown in Figures 2.6 and 2.7, respectively. The detailed data obtained from the deconvolutions is shown in Tables 2.5 and 2.6 for the carbon nanotube materials, and in Tables 2.7 and 2.8 for the graphene flake materials. For the TPD profiles deconvolution, the following assumptions were adopted: [20–23]

(a) The CO_2 profile results from the contribution of peak #1, peak #2, peak #3 and peak #4, attributed to strongly carboxylic acids, weakly acidic carboxylic acids, carboxylic anhydrides and lactones, respectively; the same width at halfheight (*W*) was imposed for peaks #2, #3 and #4;

(b) Materials GF and GFht present a fifth peak in the CO_2 profile peak at around 900 ˚C, attributed to lactones located in energetically different sites and its width at halfheight (*W*) was imposed the same as for peaks #2, #3 and #4;

(c) CO spectra are decomposed into five components: peak #1, attibuted to the decomposition of epoxyl and/or hydroxyl functionalities; peak #2, a peak not yet fully understood in the literature, that has been attributed to the decomposition of carbonyl groups in α-substituted ketones and aldehydes, that occurs at roughly the same temperature of the CO_2 peak #2; the same width at halfheight (*W*) was imposed for peaks #1 and #2; peak #3 that results from the releasing of one CO molecule during carboxylic anhydride decomposition – this peak has the same component peak maximum T_M, *W* and magnitude *A*, as the CO_2 peak #3; peak #4 and peak #5, ascribed, respectively, to the decomposition of phenols and carbonyl/quinones, in which the *W* was taken the same for both peaks.

(d) A new CO peak around 1020 ˚C was included (CO peak #6) in the TPD profiles of materials MWCNT and MWCNTh, based on the observation that the CO profile does not return to the baseline at high temperatures, and it seems that a new peak is appearing at those temperatures. This peak can be assigned to basic groups, such as pyrones and chromenes, or may result from the rearrangement of the surface.[23]

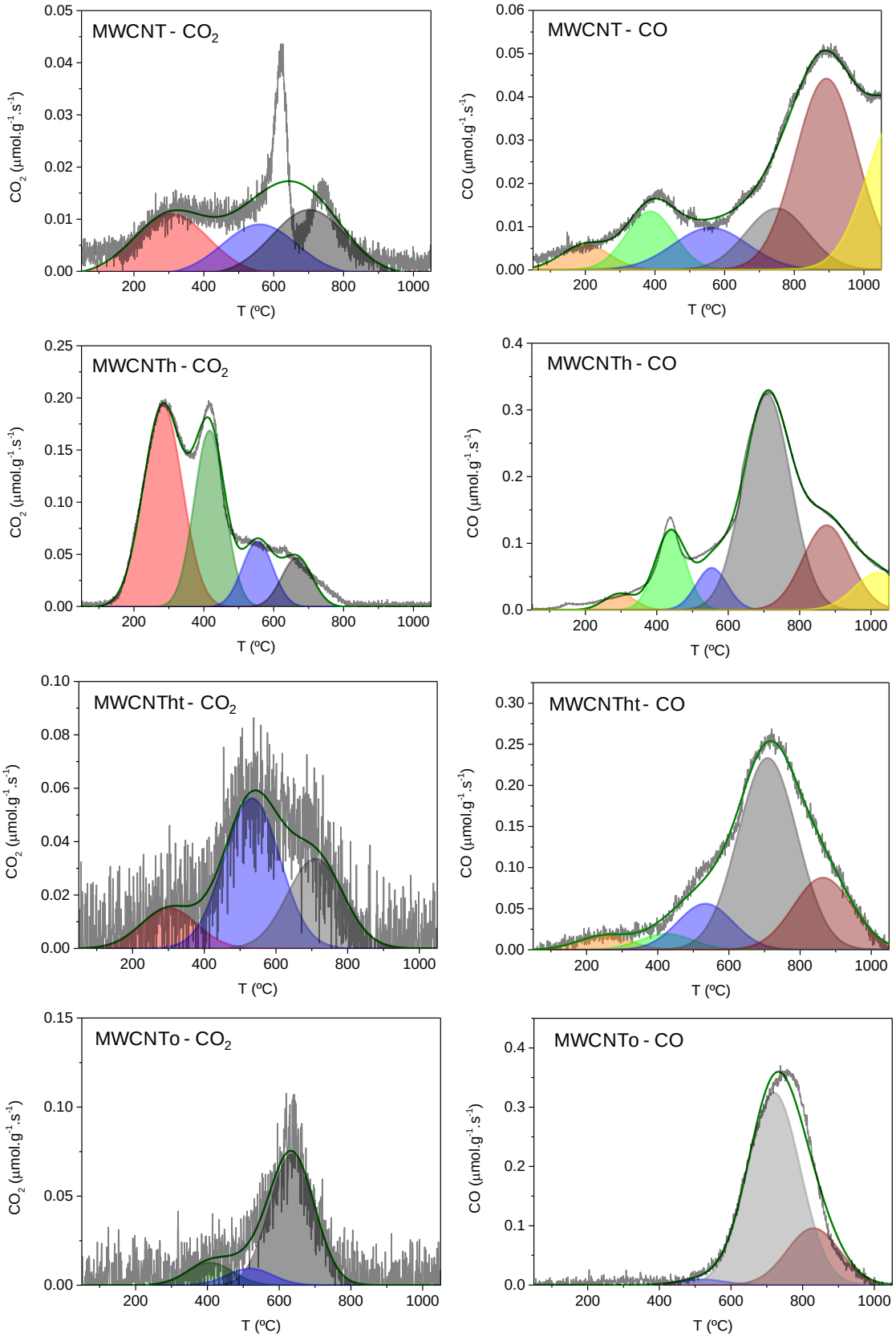

Figure 2.6 Deconvolution of the TPD profiles of the carbon nanotube materials.

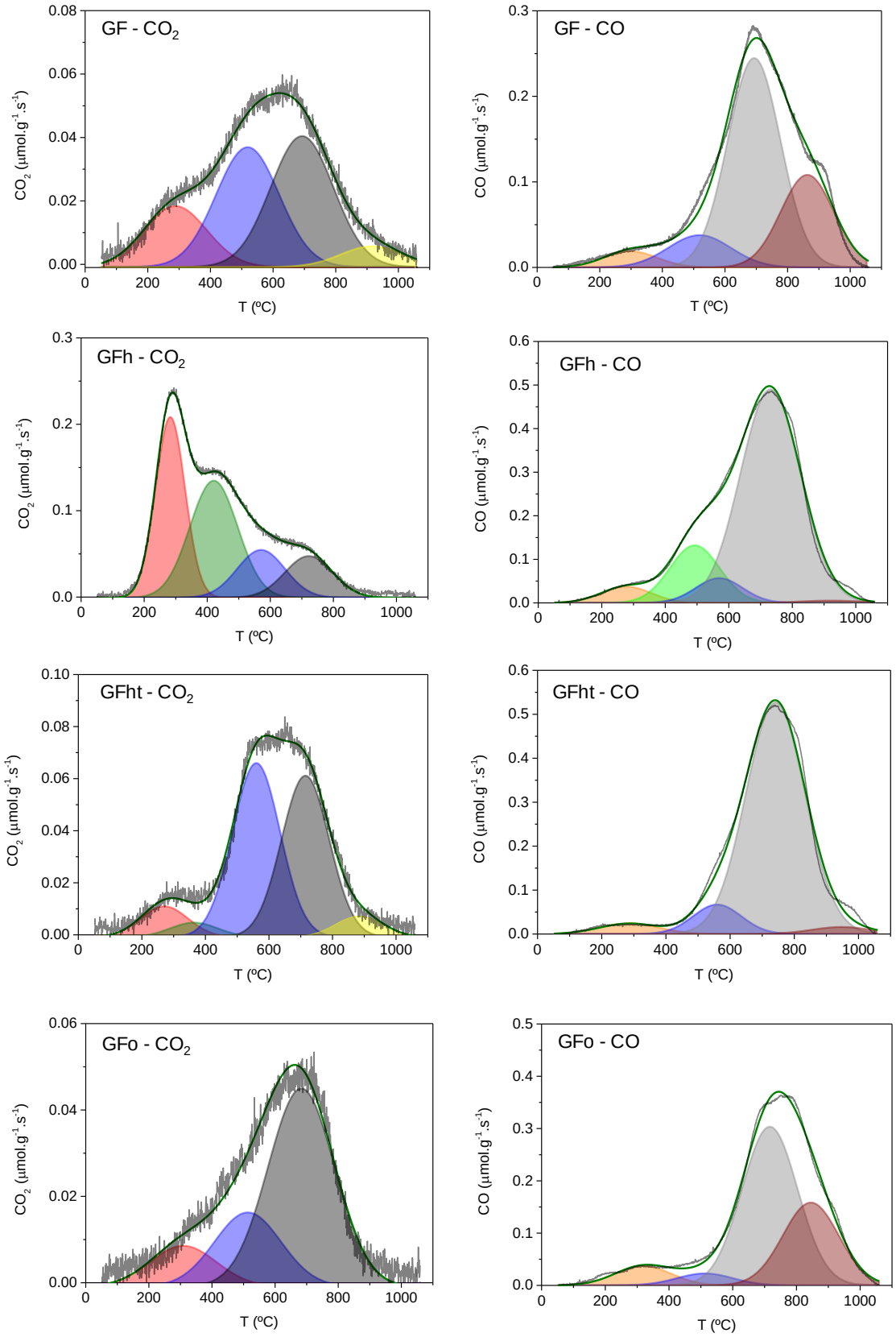

Figure 2.7 Deconvolution of the TPD profiles of the graphene flake materials.

Table 2.5 Data from the deconvolution of CO_2 TPD spectra of MWCNT materials using a multiple gaussian function.

Material	Peak #1				Peak #2				Peak #3				Peak #4					
	T_M[a] / °C	W[b] / °C	A[c] / µmol $g^{-1}s^{-1}$	% rel	T_M / °C	W / °C	A / µmol $g^{-1}s^{-1}$	% rel	T_M / °C	W / °C	A / µmol $g^{-1}s^{-1}$	% rel	T_M / °C	W / °C	A / µmol $g^{-1}s^{-1}$	% rel	A / µmol $g^{-1}s^{-1}$	A / µmol g^{-1}
MWCNT	307	251	3	33					560	251	3	33	702	251	3	34	9	108
MWCNTh	283	131	27	46	416	103	19	33	554	103	7	12	666	103	5	9	58	696
MWCNTht	302	183	3	15					533	183	11	55	710	183	6	30	20	240
MWCNTo					418	148	2	13	518	148	1	7	636	148	12	80	15	180

[a]T_M - temperature of the peak maximum; [b]W - peak width at half maximum; [c]A - integrated peak area.

Table 2.6 Data from the deconvolution of CO TPD spectra of MWCNT materials using a multiple gaussian function.

Material	Peak #1				Peak #2				Peak #3				Peak #4				Peak #5					
	T_M[a] / °C	W[b] / °C	A[c] / µmol $g^{-1}s^{-1}$	% rel	T_M / °C	W / °C	A / µmol $g^{-1}s^{-1}$	% rel	T_M / °C	W / °C	A / µmol $g^{-1}s^{-1}$	% rel	T_M / °C	W / °C	A / µmol $g^{-1}s^{-1}$	% rel	T_M / °C	W / °C	A / µmol $g^{-1}s^{-1}$	% rel	A / µmol $g^{-1}s^{-1}$	A / µmol g^{-1}
MWCNT	200	163	1	5	387	163	2	10	560	251	3	16	750	208	3	16	893	208	10	53	19	228
MWCNTh	295	101	3	3	438	101	13	13	554	103	7	8	709	157	54	62	876	157	21	24	88	1056
MWCNTht	250	175	3	4	424	175	3	4	533	183	11	13	709	196	49	58	864	196	18	21	84	1008
MWCNTo									518	148	1	1	720	174	60	76	830	174	18	23	79	948

[a]T_M - temperature of the peak maximum; [b]W - peak width at half maximum; [c]A - integrated peak area

Table 2.7 Data from the deconvolution of CO_2 TPD spectra of GF materials using a multiple gaussian function.

Material	Peak #1				Peak #2				Peak #3				Peak #4				Peak #5					
	T_M[a] / °C	W[b] / °C	A[c] / µmol $g^{-1}s^{-1}$	% rel	T_M / °C	W / °C	A / µmol $g^{-1}s^{-1}$	% rel	T_M / °C	W / °C	A / µmol $g^{-1}s^{-1}$	% rel	T_M / °C	W / °C	A / µmol $g^{-1}s^{-1}$	% rel	T_M / °C	W / °C	A / µmol $g^{-1}s^{-1}$	% rel	A / µmol $g^{-1}s^{-1}$	A / µmol g^{-1}
GF	288	237	5	20					519	237	9	35	693	237	10	39	916	237	2	6	26	312
GFh	283	111	25	35	421	179	26	37	571	179	11	15	722	179	9	13					71	852
GFht	270	177	2	7	364	177	1	4	560	177	12	43	715	177	12	43	884	177	1	3	28	336
GFo	309	248	2	11					513	248	4	22	683	248	12	67					18	216

[a]T_M - temperature of the peak maximum; [b]W - peak width at half maximum; [c]A - integrated peak area.

Table 2.8 Data from the deconvolution of CO TPD spectra of GF materials using a multiple gaussian function.

Material	Peak #1				Peak #2				Peak #3				Peak #4				Peak #5					
	T_M[a] / °C	W[b] / °C	A[c] / µmol $g^{-1}s^{-1}$	% rel	T_M / °C	W / °C	A / µmol $g^{-1}s^{-1}$	% rel	T_M / °C	W / °C	A / µmol $g^{-1}s^{-1}$	% rel	T_M / °C	W / °C	A / µmol $g^{-1}s^{-1}$	% rel	T_M / °C	W / °C	A / µmol $g^{-1}s^{-1}$	% rel	A / µmol $g^{-1}s^{-1}$	A / µmol g^{-1}
GF	299	199	4	5					519	237	9	10	693	199	52	59	863	199	23	26	88	1056
GFh	277	185	7	4	493	185	26	16	570	174	10	6	731	223	116	73	920	223	1	1	160	1920
GFht	286	218	6	4					560	177	13	9	742	218	122	84	947	218	4	3	145	1740
GFo	319	206	8	7					513	206	5	4	716	206	67	58	845	206	35	31	115	1380

[a]T_M - temperature of the peak maximum; [b]W - peak width at half maximum; [c]A - integrated peak area.

This peak was used for the deconvolution, but it was not taken into consideration for quantitative analysis.

It can be observed that all of the fits are in reasonable agreement, having approximately the same values of T_M and W for each component, when applied to the carbon nanotube materials or to the graphene flake materials containing different types and amounts of surface groups. Thus, the peak maxima found were between 270 and 310 ˚C for the strongly acidic carboxylic groups, 360 and 430 ˚C for the less acidic carboxylic groups, 510 and 575 ˚C for carboxylic anhydrides, 630 and 730 ˚C for lactones, 880 and 920 ˚C for lactones located in energetically different sites, 690 and 750 ˚C for phenols, and 830 and 950 ˚C for carbonyls/quinones. The areas and the relative percentages of each peak of the deconvoluted CO_2 and CO profiles allow us to estimate the amount of each oxygen functional group present in the different materials. Not taking into account the CO peaks #1 and #2, as these peaks are still not fully understood, and their relative area percentages are generally small, the estimated amounts of different oxygen functional groups are shown in Figure 2.8.

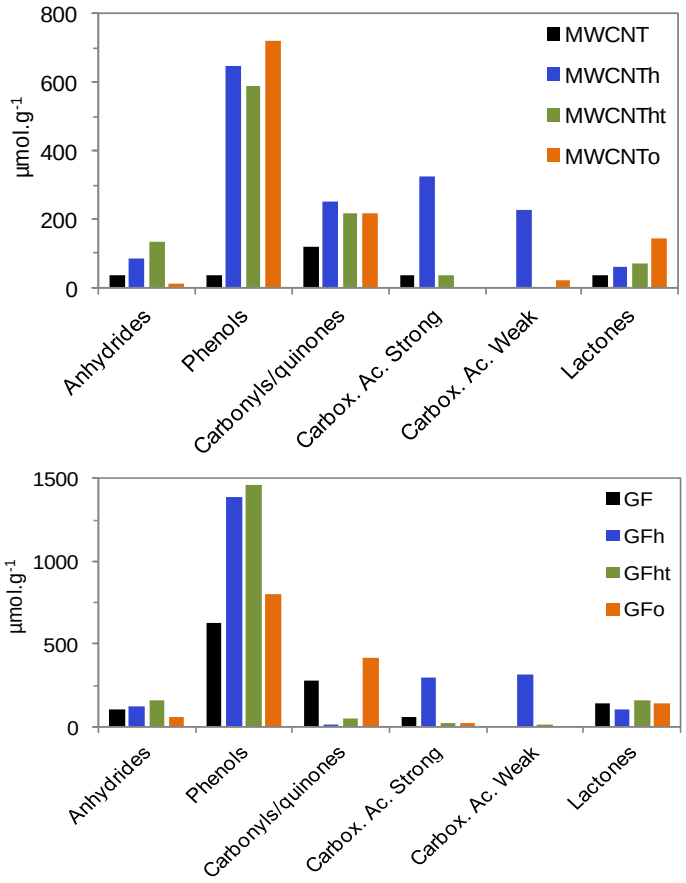

Figure 2.8 Amounts of oxygen functional groups estimated from the deconvolution of the TPD profiles of the carbon materials.

Hence, it is possible to conclude that: (i) the oxidation of MWCNT with HNO_3 promotes the increase in all the oxygen functional group amounts, most notably phenols, carboxylic acids, and carbonyls/quinones, whereas for GF, this increase is observed only for phenols, carboxylic acids and anhydrides, while the carbonyls/quinones amount is nearly depleted; (ii) the subsequent thermal treatment at 400 ˚C, under an inert atmosphere, of materials MWCNTh and GFh, resulted in the almost complete removal of carboxylic acid groups, while the amounts of carboxylic anhydrides and lactones showed a slight increase, indicating some degree of rearrangemnt of the oxygen surface groups; (iii) the gas phase oxidation treatment (5% O_2/N_2) favoured the introduction of phenols, carbonyls/quinones, and lactones; more so in the carbon naotube materials (MWCNTo), while the GFo material presented only a slight increase in phenol and carbonyl/quinone quantities; (iv) the oxidation procedures used rendered materials with different types and amounts of oxygen surface groups.

In order to further confirm the presence of oxygen functional groups in the oxidised carbon materials, FTIR spectra were also obtained (Figure 2.9).

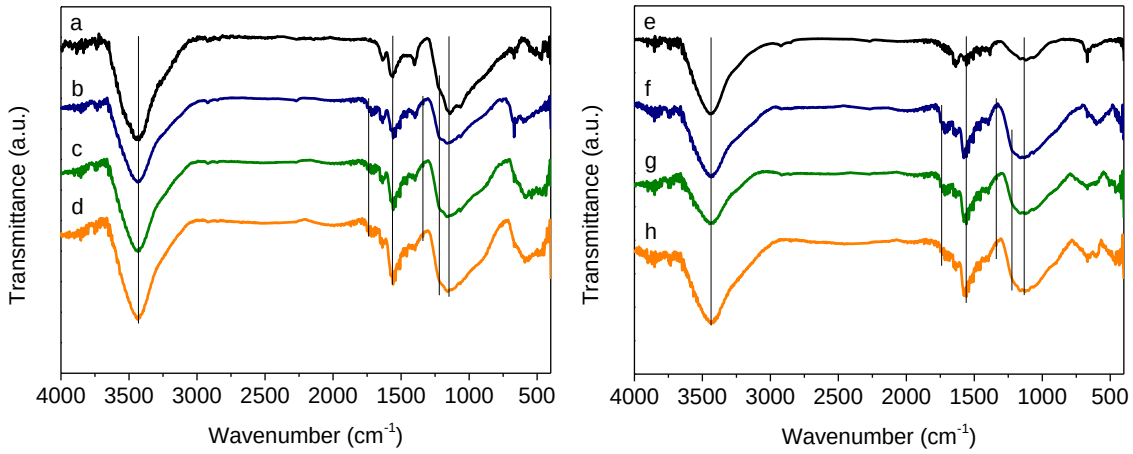

Figure 2.9 FTIR spectra of pristine MWCNT (a), MWCNTh (b), MWCNTht (c), MWCNTo (d), GF (e), GFh (f), GFht (g), and GFo (h).

Because of the extensive presence of π-π interactions in the pristine materials, their FTIR spectra present very weak and poorly resolved vibration bands. The bands observed in the original MWCNT and GF are assigned to the vibrations of the materials structure and of carbon–oxygen groups from residual oxidation: the band at 1560 cm^{-1} is assigned to C=C stretching vibrations of the aromatic carbon in non-graphitic domains,[24] the broad band at ~1130 cm^{-1} has contributions from the skeletal C–C

tangential motions (also observed in other carbon materials, such as C_{60})[24] and from some C–O stretching vibrations of oxygen groups. Finally, the band at 3430 cm^{-1} corresponds to OH stretching vibrations from hydroxyl groups. The FTIR spectra of the oxidised carbon materials present more resolved vibration bands, since the oxidation introduces some disruption of the electronic conjugation and leads to the rupture of some π–π interactions. In addition to the three vibrational bands stated above, these spectra also show a typical vibrational band of OH groups at 1340 cm^{-1}, due to the O–H bending mode, and a vibrational band at 1740 cm^{-1} due to the C=O stretching mode of carboxylic acid, carbonyl, ketone and quinone groups.[25–27] Also worth of mention is the shoulder at 1220 cm^{-1}, which is considerably more intense in the spectra of the oxidised carbon materials, when compared with the pristine materials (negligible in the case of GF), which suggests the introduction of new phenol/hydroxyl groups.[28]

The morphology of the pristine and modified carbon materials was analyzed by TEM and some examples of the obtained TEM micrographs are shown in Figures 2.10 and 2.11. The micrograph obtained for material MWCNT (Figure 2.10) shows that the thin multi-walled carbon nanotubes exist in well defined tubular structures with lengths in the micron range.

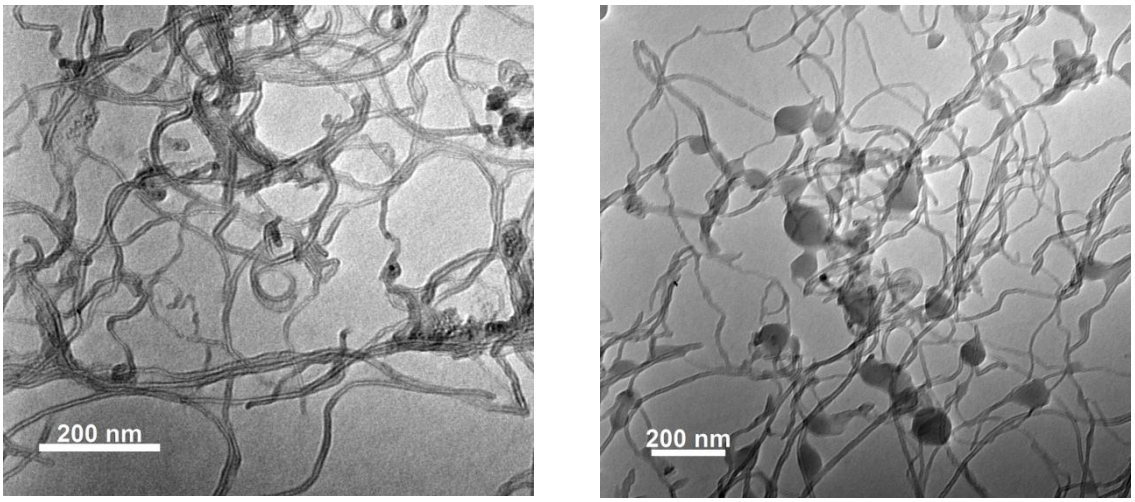

Figure 2.10 TEM micrographs of materials MWCNT (left), MWCNTht (right).

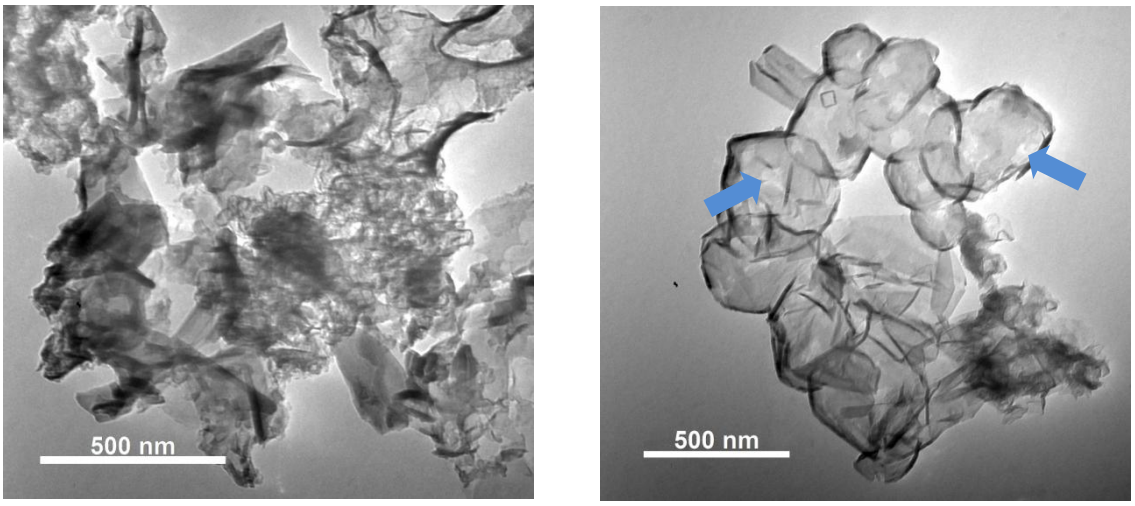

Figure 2.11 TEM micrographs of materials GF (left), and GFht (right).

The image obtained for material MWCNTht (Figure 2.10), subjected to nitric acid treatment and subsequent thermal treatment at 400 ˚C, shows peculiar sferoidal structures, which appear to be cross-linking different nanotubes. The acquired image of GF (Figure 2.11) suggests that it is composed by wrinkled few-layer graphene sheets, whose sizes are in the range of hundreds of nanometres to one micrometre. The micrograph obtained for material GFht (Figure 2.11) shows that the ball milling and subsequent thermal treatment at 600 ˚C, did not promote any apparent significant structural changes in the oxidized material. However, it is possible to observe some defective regions (marked with blue arrows), which may be attributed to the oxidation procedure.

Textural properties of the pristine and modified carbon material were evaluated by the corresponding N_2 adsorption–desorption isotherms performed at -196 ˚C, in order to assess the modifications promoted by the different oxidation procedures. Figure 2.12 depicts the N_2 adsorption–desorption isotherms for MWCNT and GF materials, and Table 2.9 presents the calculated specific surface area, S_{BET}.

All of the N_2 adsorption isotherms of the carbon materials are typically type II, accordingly to IUPAC classification,[29] which are characteristic of non-porous materials and represent unrestricted monolayer-multilayer adsorption. For the GF materials however, a distinct hysteresis loop is observed, which is characteristic of non-rigid aggregates of plate-like particles.

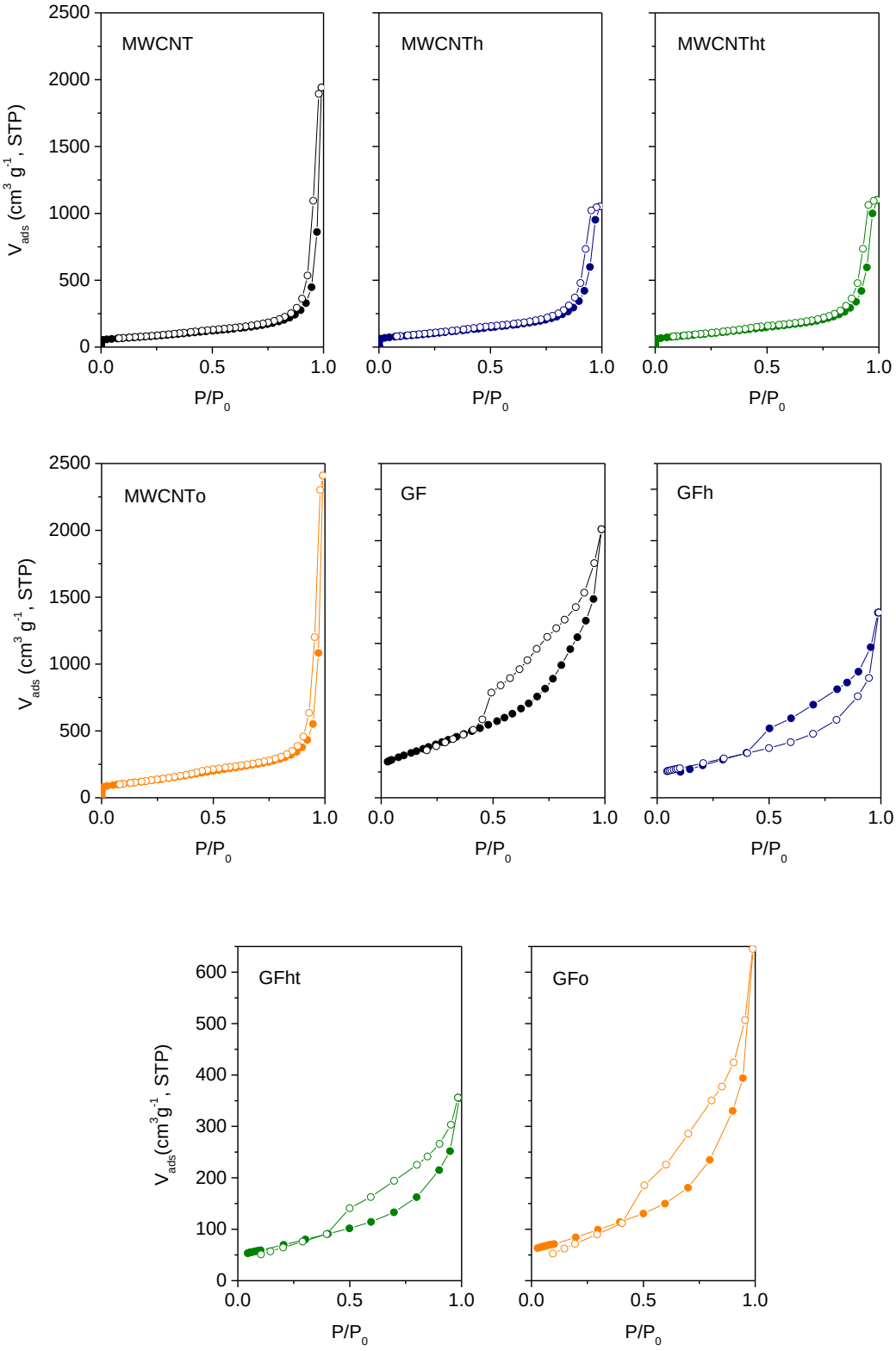

Figure 2.12 The nitrogen adsorption–desorption isotherms of the studied materials at −196 ◦C (filled and unfilled symbols represent the adsorption and desorption processes, repectively).

Table 2.9 Apparent BET surface areas of the carbon materials derived from the nitrogen adsorption–desorption isotherms at −196 °C.

Material	S_{BET} (m^2 g^{-1})
MWCNT	277
MWCNTh	348
MWCNTht	344
MWCNTo	456
GF	352
GFh	237
GFht	247
GFo	309

The differences in the material specific surface areas due to the different oxidation procedures between the carbon nanotubes and graphene flakes are striking: while the different oxidation treatments led to an increase in the nanotubes S_{BET}, they promoted an overall decrease in the surface areas of the GF counterparts. The S_{BET} increased from 277 m^2 g^{-1} in pristine MWCNT to 348, 344 and 456 m^2 g^{-1} in MWCNTh, MWCNTht, and MWCNTo, respectively. These results sugest that the oxidation procedures increased the access to the nanotubes inner cavities, throught the creation of defects and holes in the outer walls; an effect more pronounced in the gas phase treated material MWCNTo. For the graphene flake materials, the S_{BET} decreased from 352 m^2 g^{-1} in GF to 237, 247 and 309 m^2 g^{-1}, in GFh, GFht, and GFo, respectively. This decrease may be due a higher degree of agglomeration within the oxidised graphene flake crystallites, induced by the introduction of oxygen surface groups. Moreover, this decrease in the GF surface areas, follows the increase of the oxygen content present in the materials, as estimated by TPD analysis. The specific surfaces areas obtained for the GF materials allow the estimation of the average number of layers per crystallite, when comparing them the theoretical value of 2630 m^2 g^{-1} calculated for single layer graphene.[30] As such, the average number of layers are 7, 11, 11, and 8 for the GF, GFh, GFht, and GFo materials, respectively.

In order to gain further insights into the strucutral modification introduced by the different oxidation treatments on the graphene flakes, these materials were further studied by X-ray diffraction (XRD). All the XRD patterns collected and shown in Figure

2.13 show peaks at 2θ angle 26.1˚ and 43.1˚, corresponding to (002) and (101) planes of graphitic framework, respectively.[31,32]

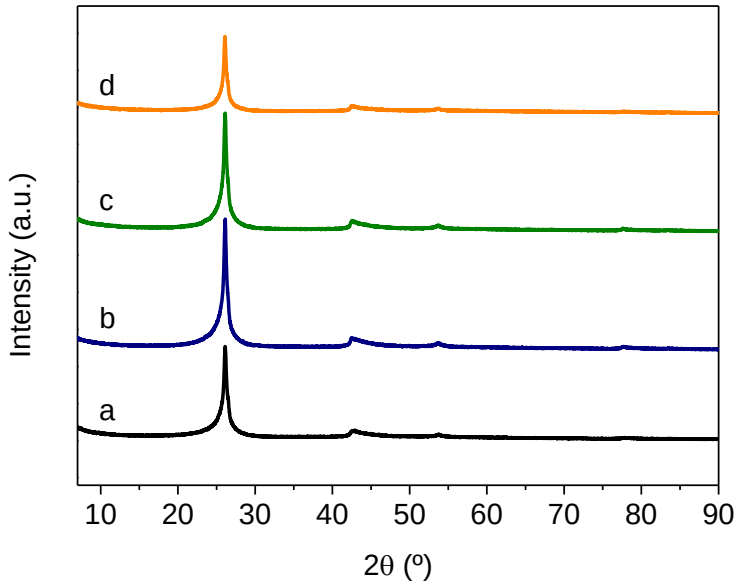

Figure 2.13 XRD patterns of: GF (a), GFh (b), GFht (c), and GFo (d).

The first peak is related to the periodicity between the graphene layers and the second within the graphene layer (honeycomb lattice at a single graphene sheet).[33] The intensity of XRD peaks has been associated with the extension of the corresponding domains.[34] In materials GFh and GFht, the intensity of the (002) peak increases in comparison to original GF, indicating a gain of periodicity in the interlayer dimensions, whereas for the gas phase treated material GFo, it remained roughly the same. Furthermore, due to the strong asymmetry observed in the (002) peaks of all XRD patterns, a Lorentzian deconvolution of the signals was performed, shown in Figure 2.14, and the deconvolution data is summarized in Table 2.10. The Bragg's equation was applied to the components of the deconvolution of the (002) peak in order to obtain the distance between graphene layers, for each crystallite type, which have different interlayer distances and a different number of graphene layers. The Scherrer's equation with a constant of 0.94 was applied to evaluate the crystallite size and number of layers per crystallite.[35]

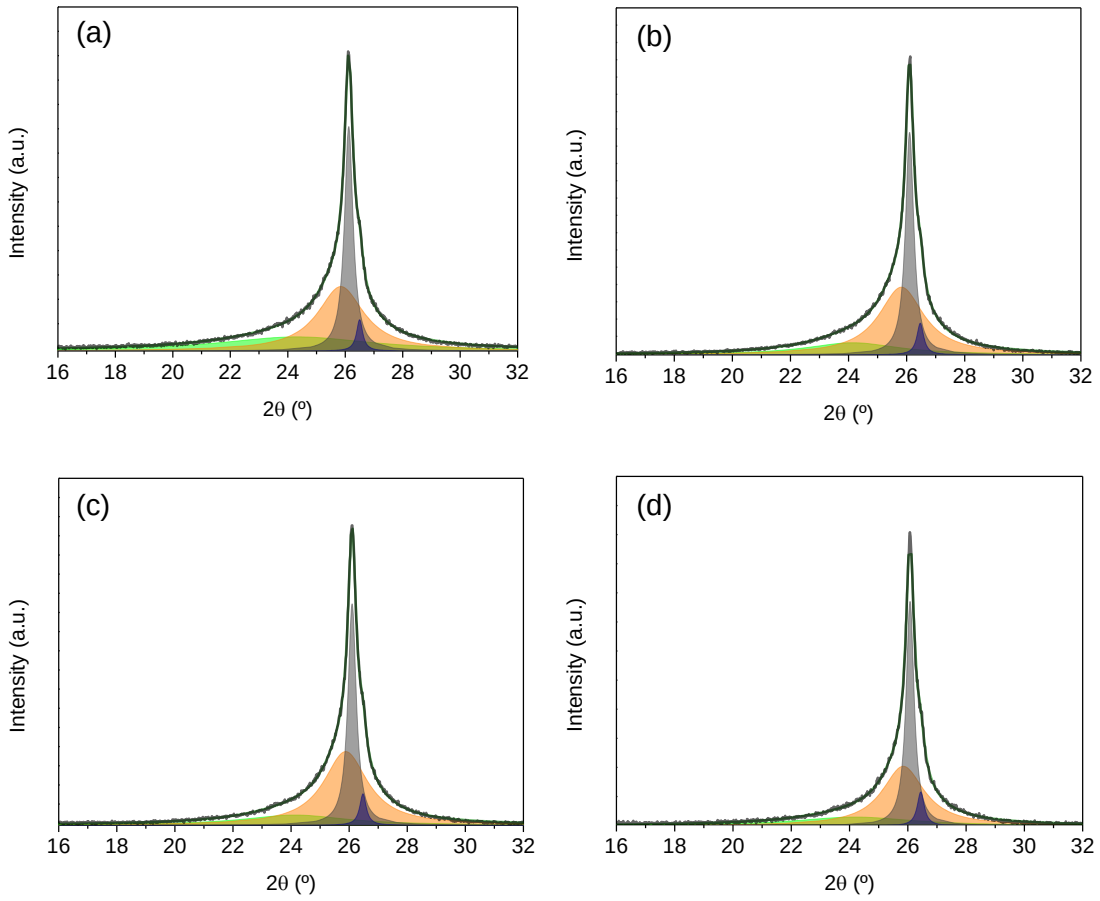

Figure 2.14 Deconvolution of the XRD (002) peak for: GF (a), GFh (b), GFht (c), and GFo (d).

Taking into account the peak area ratios of the different peak components, it was possible to estimate the weighted average number of layers for each material, namely 10, 15, 15, and 15 layers for materials GF, GFh, GFht, and GFo, respectively. This result is in reasonable agreement with the BET surface area analysis, which revealed 7, 11, 11, and 8 layers for the GF, GFh, GFht, and GFo materials, respectively. Moreover, it is possible to observe a decrease in the peak areas corresponding to the highest interlayer distance fo all the oxidised materials, indicating that the oxidation procedures induced the further stacking of the graphene flakes, which corroborates the specific surface areas obtained. It is also noteworthy that despite the existence of larger crystallites, more than 60 % of the layers are not 3-D stacked since they show interlayer spacings larger than 3.44 Å.

Table 2.10 XRD data for GF, GFh, GFht, and Gfo materials obtained from the deconvolution of the 002 peak.

Material	2θ / °	Interlayer distance / Å	Average no. layers[a]	Peak area ratio[b] / %	Weighted average no. layers[c]
GF	24.3	3.67	5	29.6	10
	25.8	3.46	14	41.2	
	26.1	3.42	70	26.5	
	26.5	3.37	99	2.7	
GFh	24.1	3.70	7	18.0	15
	25.8	3.46	14	48.9	
	26.1	3.42	72	29.7	
	26.5	3.37	92	3.4	
GFht	24.1	3.70	6	16.7	15
	25.9	3.44	15	51.2	
	26.1	3.42	74	28.9	
	26.5	3.37	95	3.2	
GFo	24.2	3.68	6	18.8	15
	25.8	3.46	15	44.8	
	26.1	3.42	77	32.1	
	26.4	3.38	88	4.3	

[a]Assuming that the areas of the XRD peaks are proportional to the no. of layers (which are stacked in different numbers to form crystallites of different sizes), the weighted average number of layers may be roughly estimated as follow: if one consider that 2.7 % of the layers are stacked as 1 crystallite of 99 layers, then the total number of layers is 3678; there will be 14 crystallites of 70 layers, 111 of 14 layers and 237 of 5 layers, which totals 363 crystallites. Thus, the average number of layers will be 3678/363 = 10 layers per crystallite.

Raman spectroscopy was employed in order to gain some general structural information on the studied materials. Fig. 2.15 shows first and second order Raman spectra of the pristine and modified MWCNT and GF materials. The first-order Raman spectrum of the studied materials is characterized by strong bands at ~1350 and ~1580 cm^{-1}, known as D and G bands, respectively. Defect-free graphite would only show the G band, common to all sp^2 carbon systems and corresponds to the first-order scattering of the E_{2g} mode, whereas the D band corresponds to a phonon mode whose intensity is strictly connected to the presence of six-fold aromatic rings close to local lattice distortions (defects) of the graphitic network.[36]

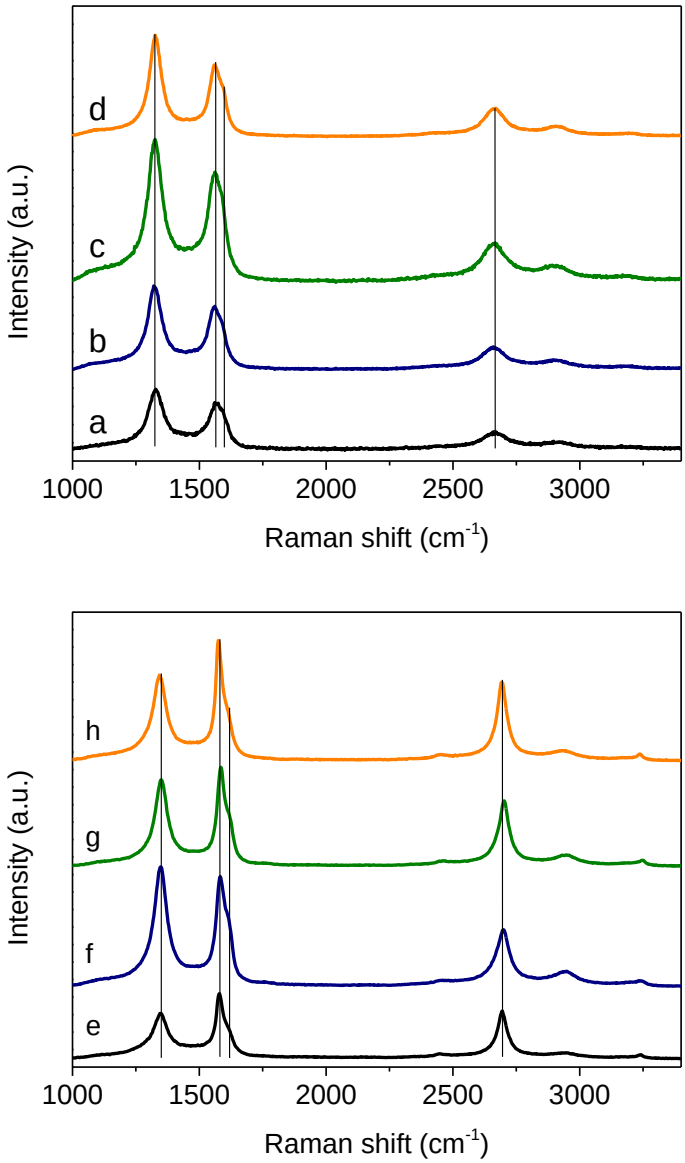

Figure 2.15 Raman spectra of pristine MWCNT (a), MWCNTh (b), MWCNTht (c), MWCNTo (d), GF (e), GFh (f), GFht (g), and GFo (h).

These distortions can be due, for example, to the presence of edges of graphitic planes, atomic vacancies or oxygenated groups. In the second-order spectra of original and oxidized graphene flakes, there is a strong peak at ~2700 cm^{-1}, assigned as the 2D mode and that is the overtone of the D peak. At ~1620 cm^{-1} it is also possible to identify a weak shoulder that corresponds to the D' mode. The intensity ratio of the D and G bands is commonly used to estimate the disorder degree of graphitic materials.[17,37–39] Figure 2.16 presents the I_D/I_G ratio for the pristine and modified MWCNT and GF materials. The oxidized carbon nanotube materials presented an

increase in the I_D/I_G for all materials, indicating the introduction of defects on the nanotubes structure. This result is concomitant with the N_2 adsorption isotherms, which showed that the oxidation procedures, increased the nanotube specific surface areas, throught the increase of the access to the inner cavities promoted by the formation of holes/defects.

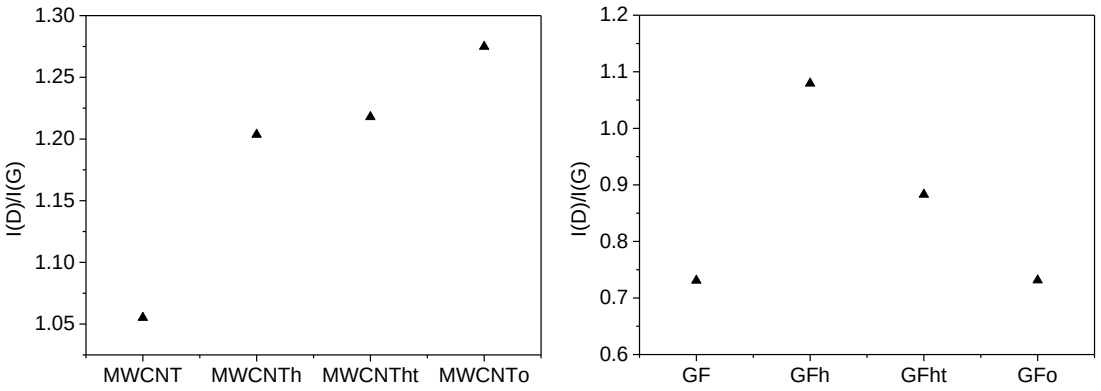

Figure 2.16 Calculated I_D/I_G ratio for the pristine and modified MWCNT and GF materials.

As for the GF materials, the I_D/I_G ratio increased considerably after HNO_3 oxidation for GFh, followed by a decrease after the thermal treatment at 400 ˚C in GFht, whereas the GFo material remained practically the same as the pristine material. These observations indicate the disorder effect of the introduction of oxygen functionalities on the structure of GF and the occurrence of structural defects. The results indicate that nitric acid, being a potent oxidant, introduced defects and oxygen functional groups to a greater extent in GFh, while the subsequent thermal treatment promoted the removal of part of the oxygen functionalities and possibly some degree of graphitization in GFht. As for the GFo, the unaltered I_D/I_G ratio indicates that the O_2 oxidation did not promote significant structural defects These results are in good agreement with the data obtained by XPS and TPD, concerning the variation of oxygen content upon the different oxidation procedures.

2.3.2 Catalytic studies

The catalytic oxidation of *cis*-cyclooctene (CyO) with 30% H_2O_2 in acetonitrile, at 80 ˚C, was studied in heterogeneous phase, using the pristine and modified carbon materials as catalysts, as schematized in Figure 2.17.

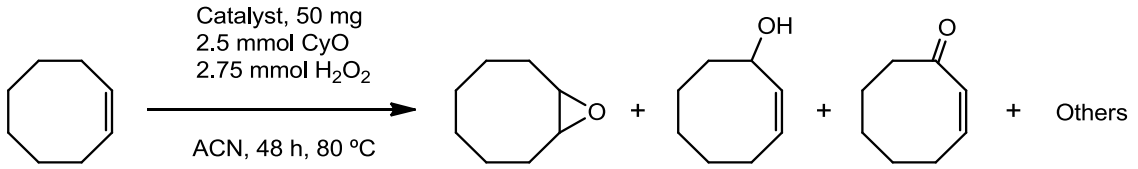

Figure 2.17 Reaction scheme of the studied catalytic experiments.

Under these reaction conditions, three main oxidation compounds are produced, namely, epoxycyclooctane, cyclooct-2-enol, and cyclooct-2-enone, as confirmed by GC-MS analysis. Small percentages of other oxidation products were also found, but their identification was not possible, hence these will be further referred to as *Others*. Results for the catalytic oxidation of cyclooctene with 30% H_2O_2 (molar ratio H_2O_2/CyO =1.1) are depicted in Figures 2.18, and 2.19, and summarized in Table 2.11.

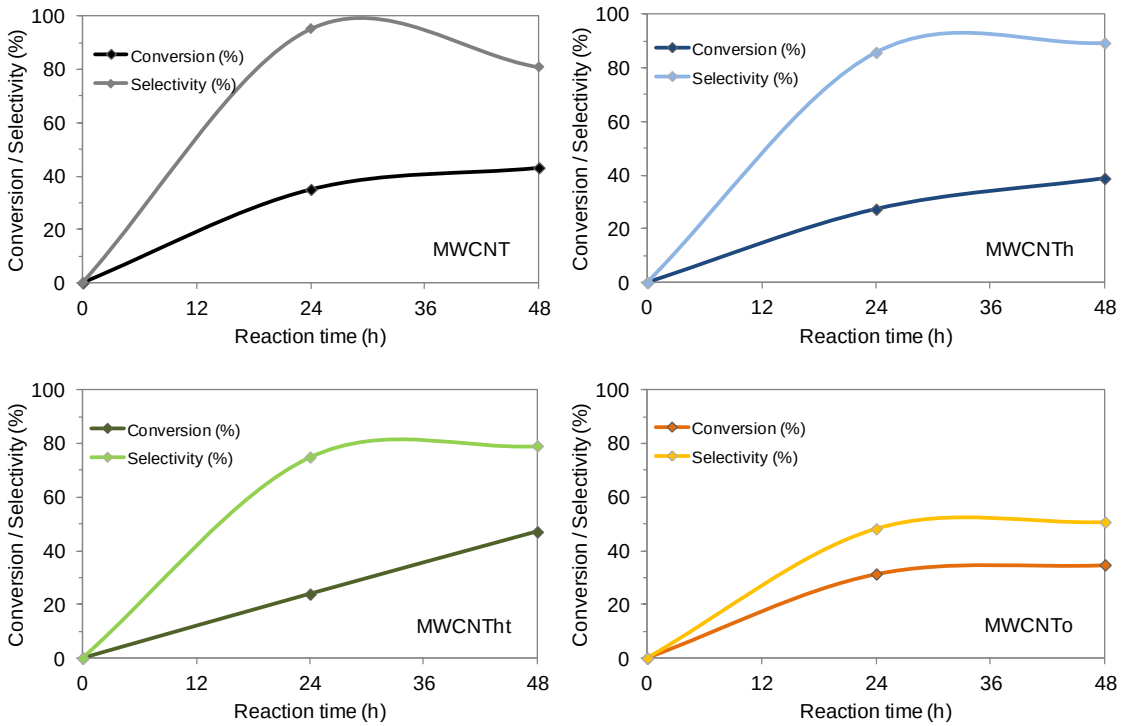

Figure 2.18 Reaction profiles for the oxidation of *cis*-cyclooctene using the carbon nanotube materials as catalysts.

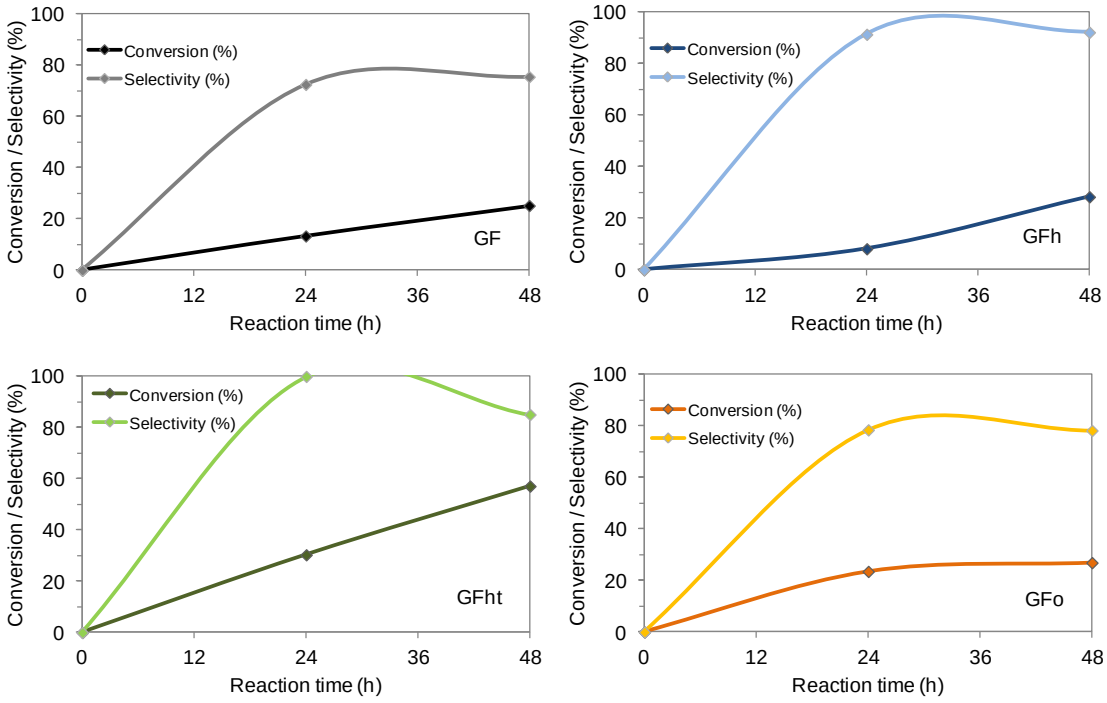

Figure 2.19 Reaction profiles for the oxidation of *cis*-cyclooctene using the graphene flake materials as catalysts.

All the carbon materials catalyse the oxidation of *cis*-cyclooctene. Their catalytic conversions are between 25 and 57 % after 48 h of reaction. In the absence of the carbocatalysts, the oxidation of *cis*-cyclooctene yields 19 %. Pristine MWCNT material yields a 43 % conversion, and the oxidised materials present similar conversions of 39, 47, and 35 % for materials MWCNTh, MWCNTht, and MWCNTo, respectively. Selectivity to epoxycyclooctane after 3 catalytic cycles, however, increases from 64 % in pristine MWCNT to 81 and 74 % in MWCNTh and MWCNTht, respectively, and decreases to 48 % in MWCNTo. This indicates that the types and amounts of surface groups introduced by the oxidation treatments influence the reaction pathway, with the materials having more acidic groups (MWCNTh, MWCNTht) yielding higher selectivities to epoxycyclooctane than those bearing more neutral groups (MWCNT, MWCNTo), which have a higher preference for the allylic oxidation.

For the graphene flake materials, conversion was 25 % for pristine GF, remaining roughly the same at 28 and 27 % for materials GFh and GFo, and increasing to 57 % for GFht. As with the nanotube materials, selectivity to epoxycyclooctane increased from 76 % in pristine GF to 92 and 85 % in GFh and GFht, respectively, and remained roughly the same in GFo (78 %).

Table 2.11 Catalytic activity of the carbocatalysts in the selective oxidation of *cis*-cyclooctene.

Material	Cycle	Conv. (%)[a]	TON × 10^{-2} (mol g^{-1})[b]	TOF × 10^{-4} (h^{-1})[c]	Product selectivity (%)[d]		
					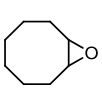	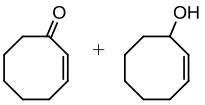	Others
No catalyst	1st	18			73	27	0
MWCNT	1st	43	2.2	4.5	81	13	6
	2nd	49	2.4	5.1	64	24	12
	3rd	68	3.4	7.0	64	25	11
MWCNTh	1st	39	1.9	4.0	89	9	2
	2nd	47	2.3	4.9	86	11	3
	3rd	42	2.1	4.4	81	15	4
MWCNTht	1st	47	2.4	4.9	79	18	3
	2nd	49	2.5	5.1	77	18	5
	3rd	69	3.5	7.2	74	20	6
MWCNTo	1st	35	1.7	3.6	51	41	8
	2nd	41	2.0	4.3	47	42	11
	3rd	47	2.4	4.9	48	42	10
GF	1st	25	1.3	2.6	76	21	3
	2nd	50	2.5	5.2	77	21	2
	3rd	54	2.7	5.7	77	20	3
GFh	1st	28	1.4	3.0	92	6	2
	2nd	39	2.0	4.1	95	4	1
	3rd	38	1.9	3.9	92	7	1
GFht	1st	57	2.9	6.0	85	12	3
	2nd	64	3.2	6.7	94	6	0
	3rd	74	3.7	7.7	90	8	2
GFo	1st	27	1.3	2.8	78	20	2
	2nd	46	2.3	4.8	73	23	4
	3rd	55	2.8	5.8	74	2	3

[a]Conversion refers to GC yields and was calculated through the internal standard method, using chlorobenzene as the internal standard, with 48 h of reaction time. [c]TON = mol reacted *cis*-cyclooctene / g catalyst. [d]TOF = TON / reaction time. [d]Selectivities are with respect to epoxide, enol + enone, and others, and obtained as molar percentages of the indicated products of the sum of moles of all products.

This corroborates the observation that the presence of more acidic groups, e.g. carboxylic acids, carboxylic anhydrides, favour the selectivity to epoxycyclooctane, while the existence of more neutral groups like carbonyls and phenols increase the

allylic oxidation. Interestingly, the conversion for GFht (57 %) is significantly higher than for GFh (28 %), while their selectivities to epoxycyclooctane remain similar (92 and 85 %, respectively). From the TPD data, it was shown that there was a considerable removal of carboxylic acid groups for GFht, and an increase in carboxylic anhydrides, during the applied thermal treatment. Thus, the catalytic results indicate that the surface rearrengement of the oxygen groups during the thermal treatment led to an optimized ratio of acidic groups, which yielded a more active catalyst, whilst preserving the desired selectivity. These results are consistent with previously published results by Zhou *et al.* and Li *et al.*, which used mesoporous carbons and P-doped macroporous carbon spheres, respectively, in the oxidation of *cis*-cyclooctene.[40,41] All carbon materials were reused two times in the catalytic oxidation of *cis*-cyclooctene, without changing the molar ratios and reaction concentrations, and their conversion/selectivity evolution are shown in Figures 2.20 and 2.21.

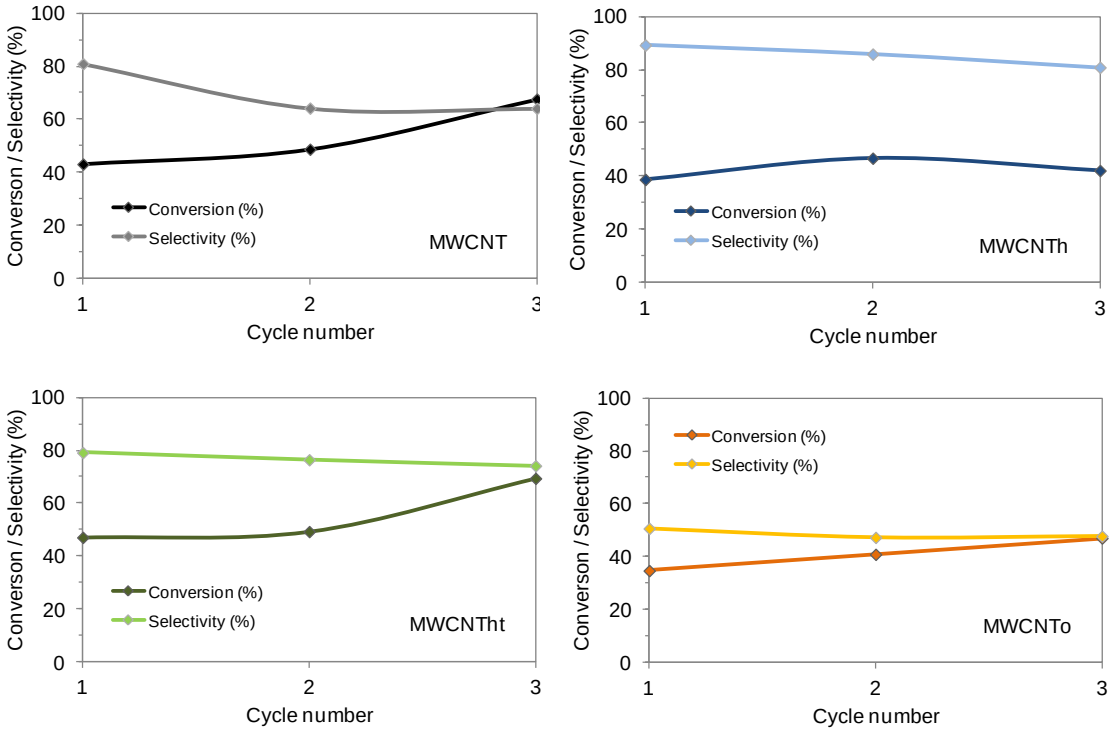

Figure 2.20 Conversion/selectivity evolution during the reutilization of the carbon nanotube materials in the oxidation of *cis*-cyclooctene, up to three cycles.

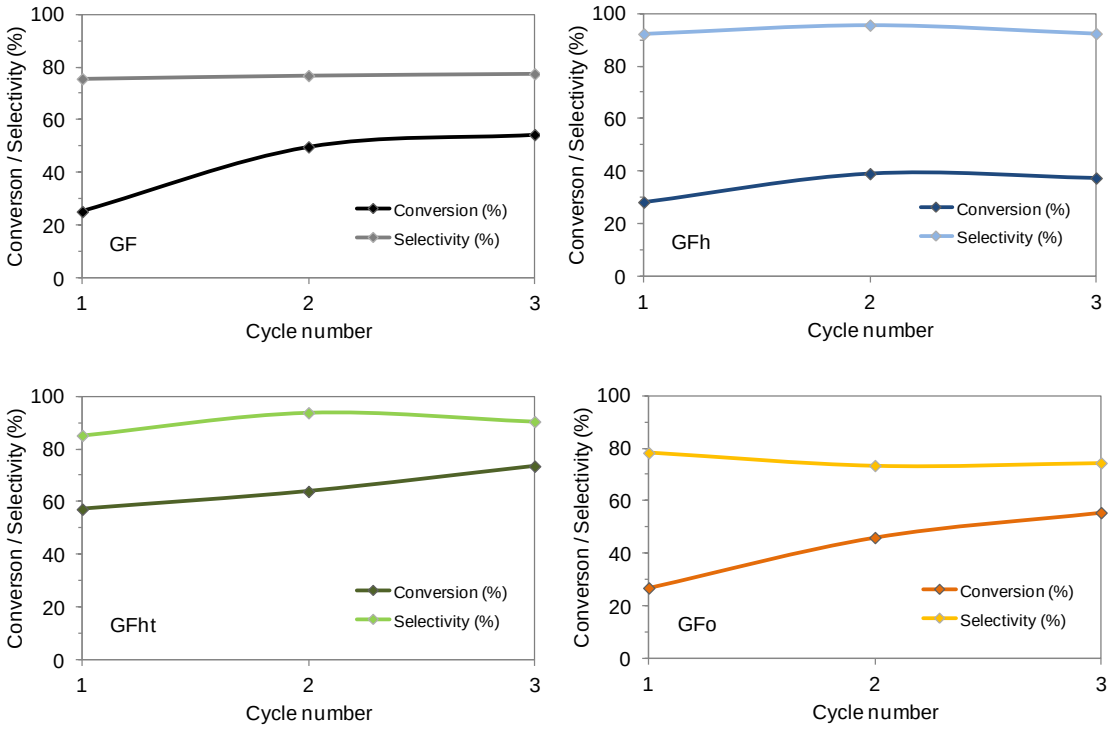

Figure 2.21 Conversion/selectivity evolution during the reutilization of the graphene flake materials in the oxidation of *cis*-cyclooctene, up to three cycles.

For the carbon nanotube materials, it is possible to observe an increase in the conversion percentages in the 2nd and 3rd cycles, and a slight decrease in the selectivity to epoxycyclooctane, while in the graphene flake materials, there is also an increase in conversion, but the selectivities remain almost inaltered. We attribute this increase in catalytic activity to the use of H_2O_2 as oxidant in the catalytic reactions, which further promotes the surface oxidation of all the carbon materials. Summing up, the modifications introduced in the carbon nanotubes and graphene flakes originated active, stable and selective catalysts in the oxidation of *cis*-cyclooctene, with the nitric acid followed by thermal treatment at 400 ˚C, yielding catalysts with superior activity and selectivity.

2.4 Conclusions

Multi-walled carbon nanotubes and graphene flakes were successfully modified through three different oxidation procedures, namely nitric acid treament, nitric acid followed by thermal treatment, and gas phase oxidation with O_2.

The materials characterization through XPS, TPD, and FTIR showed an overall increase in the materials oxygen content upon the different oxidation procedures and revealed that they induced different superficial chemical compositions, namely: (i) nitric acid treated materials MWCNTh and GFh, presented increased amounts of carboxylic acids, anhydrides and phenols; (ii) nitric acid followed by thermal treatment at 400 ˚C induced the removal of carboxylic acids and an increase in anhydrides content; (iii) gas phase oxidation promoted the introduction of phenols, carbonyls/quinones, and lactones.

Textural characterization through N_2 adsorption-desorption isotherms revealed that the oxidation procedures promoted an increase in the carbon nanotube materials specific surface area, through the increase in the inner cavities access, while the graphene flake materials present lower surface areas upon the oxidation procedures, indicating a higher degree of agglomeration, which was confirmed through XRD analysis. Raman spectroscopy revealed that the oxidation procedures promoted an overall increase in the materials disorder through the introduction of defects onto their original structure.

The catalytic studies showed that all the materials were active catalysts in the selective oxidation of *cis*-cyclooctene and that the modifications introduced in the carbon nanotubes and graphene flakes, through nitric acid followed by thermal treatment at 400 ˚C, originated catalysts with superior activity and selectivity in regard to their pristine counterparts. Reusability experiments revealed no loss of catalytic activity up to three catalytic cycles. These results clearly indicate that the fine tuning of the carbon materials morphology and surface chemistry, concerning amount of defects and types and amounts of oxygen surface groups, respectively, is of most importance in pursuing the generation of metal-free carbocatalysts with superior performance and selectivity.

References

[1] K. A. Jorgensen, *Chem. Rev.* **1989**, *89*, 431–458.

[2] P. Kim, C. M. Lieber, T. Ichihashi, C. Papadopoulos, J. M. Xu, M. Moskovits, N. Hamada, A. Oshiyama, R. Kuozo, M. Terauchi, et al., *Science* **2001**, *292*, 1139–1141.

[3] D. S. Su; J. Zhang; B. Frank; A. Thomas; X. Wang; J. Paraknowitsch; R. Schlögl, *ChemSusChem* **2010**, *3*, 169–180.

[4] M. D. Hughes, Y. Xu, P. Jenkins, P. Mcmorn, P. Landon, D. I. Enache, A. F. Carley, G. A. Attard, G. J. Hutchings, F. King, et al., *Nature* **2005**, *437*, 1132–1135.

[5] S. Bawaked, N. F. Dummer, D. Bethell, D. W. Knight, G. J. Hutchings, *Green Chem.* **2011**, *13*, 127–134.

[6] C. A. Deshmane, J. B. Jasinski, P. Ratnasamy, M. A. Carreon, *Catal. Commun.* **2011**, *15*, 46–51.

[7] C. Chen, J. Qu, C. Cao, W. Song, *J. Mater. Chem.* **2011**, *21*, 5774–5779.

[8] M. R. Farsani, F. Jalilian, B. Yadollahi, *Appl. Organomettalic Chem.* **2014**, *29*, 7–11.

[9] P. Serp, J. L. Figueiredo, *Carbon Materials for Catalysis*, Jonh Wiley & Sons, **2008**.

[10] H. Yu, F. Peng, J. Tan, X. Hu, H. Wang, J. Yang, W. Zheng, *Angew. Chemie - Int. Ed.* **2011**, *50*, 3978–3982.

[11] D. R. Dreyer, H. Jia, C. W. Bielawski, *Angew. Chemie - Int. Ed.* **2010**, *49*, 6813–6816.

[12] K. Kamata, *Science* **2003**, *300*, 964–966.

[13] S. Brunauer, P. H. Emmett, E. Teller, *J. Am. Chem. Soc.* **1938**, *60*, 309–319.

[14] J. F. Moulder, W. F. Stickle, P. E. Sobol, K. D. Bomben, *Handbook of X-Ray Photoelectron Spectroscopy*, Perkin-Elmer, **1992**.

[15] Y. Xie, P. M. A. Sherwood, *Chem. Mater.* **1990**, *2*, 293–299.

[16] D. R. Dreyer, S. Park, W. Bielawski, R. S. Ruoff, *Chem. Soc. Rev.* **2010**, *39*, 228–240.

[17] S. Stankovich, D. A. Dikin, R. D. Piner, K. a. Kohlhaas, A. Kleinhammes, Y. Jia, Y. Wu, S. T. Nguyen, R. S. Ruoff, *Carbon* **2007**, *45*, 1558–1565.

[18] H. Estrade-Szwarckopf, *Carbon* **2004**, *42*, 1713–1721.

[19] A. B. Dongil, B. Bachiller-baeza, A. Guerrero-ruiz, I. Rodríguez-ramos, A. Martínez-alonso, *J. Colloid Interface Sci.* **2011**, *355*, 179–189.

[20] S. M.-T. Luisa M. Pastrana-Martínez, V. Likodimos, P. Falaras, J. L. Figueiredo, J. L. Faria, A. M. T. Silva, *Appl. Catal. B Environ.* **2014**, *158–159*, 329–340.

[21] X. Fenga, X. Mab, N. Lia, C. Shanga, X. Yanga, Xiao Dong Chen, *RSC Adv.* **2015**, *5*, 74684–74691.

[22] J. L. Figueiredo, M. F. R. Pereira, M. M. A. Freitas, J. J. M. Orfao, *Carbon* **1999**, *37*, 1379–1389.

[23] J. L. Figueiredo, M. F. R. Pereira, M. M. A. Freitas, *Ind. Eng. Chem. Res.* **2007**, *46*, 4110–4115.

[24] H. Gaspar, C. Pereira, S. L. H. Rebelo, M. F. R. Pereira, J. L. Figueiredo, C. Freire, *Carbon* **2011**, *49*, 3441–3453.

[25] W. Gao, G. Wu, M. T. Janicke, D. A. Cullen, R. Mukundan, J. K. Baldwin, E. L. Brosha, C. Galande, P. M. Ajayan, K. L. More, et al., *Angew. Chemie - Int. Ed.* **2014**, *53*, 3588–3593.

[26] C. K. Chua, M. Pumera, *Chem. Eur. J.* **2014**, *20*, 1871–1877.

[27] K. Krishnamoorthy, M. Veerapandian, K. Yun, S. Kim, *Carbon* **2012**, *53*, 38–49.

[28] N. Wu, X. She, D. Yang, X. Wu, F. Su, Y. Chen, *J. Mater. Chem.* **2012**, *22*, 17254–17261.

[29] M. Thommes, K. Kaneko, A. V Neimark, J. P. Olivier, F. Rodriguez-reinoso, J. Rouquerol, K. S. W. Sing, *Pure Appl. Chem.* **2015**, *87*, 1051–1069.

[30] S. Park, R. S. Ruoff, *Nat. Nanotechnol.* **2009**, *4*, 217–224.

[31] A. B. Fuertes, S. Alvarez, *Carbon* **2004**, *42*, 3049–3055.

[32] T. Kim, I. Park, R. Ryoo, *Angew. Chemie - Int. Ed.* **2003**, *42*, 4375–4379.

[33] D. Reznik, C. H. Olk, D. A. Neumann, J. R. D. Copley, *Phys. Rev. B* **1995**, *52*, 116–124.

[34] J. P. Novais, S. L. H. Rebelo, B. Bachiller-baeza, M. E. Lipin, I. Rodríguez-ramos, A. Guerrero-ruiz, C. Freire, *Polyhedron* **2014**, *81*, 475–484.

[35] B. K. Saikia, R. K. Boruah, P. K. Gogoi, *J. Chem. Sci.* **2009**, *121*, 103–106.

[36] A. C. Ferrari, J. Robertson, *Phys. Rev. B* **2000**, *61*, 95–107.

[37] J. I. Paredes, P. Sol, A. Mart, J. M. D. Tasc, *Langmuir* **2009**, *25*, 5957–5968.

[38] H. Kang, A. Kulkarni, S. Stankovich, R. S. Ruoff, S. Baik, *Carbon* **2009**, *47*, 1520–1525.

[39] M. S. Dresselhaus, A. Jorio, M. Hofmann, G. Dresselhaus, *Nano Lett.* **2010**, *10*, 751–758.

[40] L. Zhou, J. Liu, X. Zhang, R. Liu, H. Huang, Y. Liu, Z. Kang, *Nanoscale* **2014**, *6*, 5831–5837.

[41] C. Li, M. Yang, R. Liu, F. Zhao, H. Huang, Y. Liu, *RSC Adv.* **2014**, *4*, 22419–22424.

Chapter 3

Heteroatom-doped carbocatalysts for the reduction of 4-nitrophenol

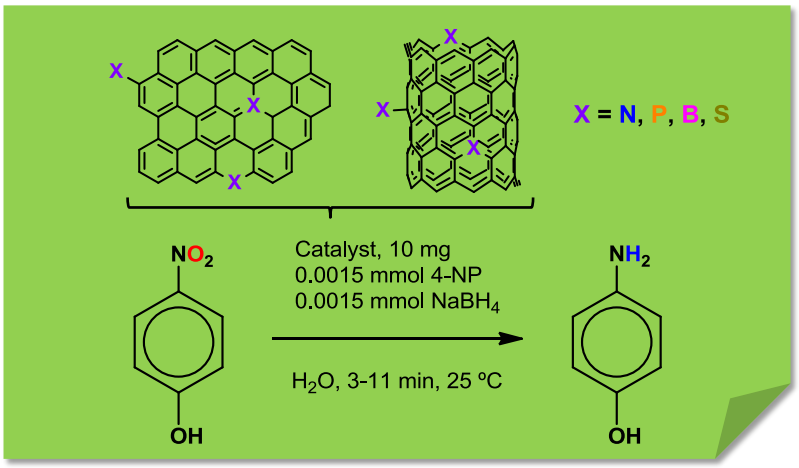

3

Heteroatom-doped carbocatalysts for the reduction of 4-nitrophenol[1]

Abstract

In this work, it is described the preparation and characterization of multi-walled carbon nanotubes and graphene flakes doped with heteroatoms, namely N, P, B, and S, through simple ball milling procedures with adequate precursors, followed by thermal treatment in an inert atmosphere. Ball milling the carbon nanomaterials with melamine resulted in the introduction of pyrrolic, pyridinic and quaternary N atoms on the graphitic structure. Using triphenylphosphine as the phosphorous precursor induced the formation of R-O-$PO(OH)_2$ functionalities. Materials prepared with boric acid showed the presence of boronic groups (C-BO_2) and B atoms in B_2O_3. S-doped materials presented tiophene-S type atoms. The doping procedures increased the carbon nanotubes specific surface areas, due to the breaking of tubular structures, whereas the graphene flakes presented an overall decrease in specific surface area, probably due to a higher degree of agglomeration within the doped graphene materials. A reduction of the overall amount of defects in the carbon nanotube materials was observed, whereas for all the doped graphene flake materials, the amount of disorder increased with the doping treatments. The catalytic studies showed that all the doped carbon materials were active catalysts in the reduction of 4-NP in the presence of $NaBH_4$, and that the modifications introduced by doping the carbon nanotubes and graphene flakes with heteroatoms, overall yielded catalysts with superior activity in regard to their pristine counterparts. Reusability experiments revealed no loss of catalytic activity up to three catalytic cycles for the doped carbon nanotubes, whereas the graphene flake materials showed some deterioration of catalytic performance. The results show the successful doping of the carbon materials with heteroatoms (N, P, B and S), as a convenient procedure in the preparation of metal-free carbocatalysts with superior performance in the reduction of 4-NP.

[1] The experimental details on the physico-chemical characterisation techniques are indicated in Appendix A.

3.1 Introduction

Aromatic amines are crucial intermediates in the preparation of several nitrogen-containing biologically active compounds, agrochemicals, dyes, polymers, etc.[1–3] They are the precursors for many important intermediates like amides, imines, azo compounds, isocyanates and diazonium salts which can be converted to other functional groups.[4–6] The importance of aryl amines as raw materials for these applications has spurred extensive research in developing new and sustainable processes for the reduction of nitroarenes.[7]

Reduction of nitroarenes is a most common, short and facile route employed to prepare anilines. Traditionally, nitro group reductions are carried out using various transition metal or precious metal catalysts.[8–10] However, their use on an industrial scale is restricted by limited reserves, high cost and low stability. Moreover, due to increasing environmental concerns, the development of innovative methods that maximize synthetic efficiency and minimize waste generation is a challenging but necessary task.

In moving towards green and sustainable chemistry, carbon nanostructured materials without metal elements have been explored and studied extensively in catalysis.[11] Most pristine carbon materials are chemically inert and their functionalization or surface modification is crucial to render them chemically active. Doping the nanostructured carbon materials with heteroatoms, which are able to create superficial defects and break the chemical inertness of pure carbon materials, represents a feasible path to achieve enhanced reactivity. In fact, heteroatom doped carbon materials represent one of the most promising families of materials that are used in energy related applications, such as fuel cells, batteries, hydrogen storage or super-capacitors.[12–14] Doping substantially modifies the atomic scale structures, surface energy, chemical reactivity and mechanical properties of carbon nanomaterials.[15,16] Among the large variety of carbon materials, in this work we will focus on doped multi-walled carbon nanotubes and graphene flakes. Regarding the reduction of nitroarenes using carbon catalysts, it is worth mentioning the work by Chen *et al.*,[17] which assesses the catalytic activity of N-graphene in the reduction of 4-NP, and Arai *et al.* who studied chemoselective transfer hydrogenation of nitrobenzene over oxygen- and nitrogen-doped activated carbon.[18]

In the present Chapter, we report the doping of commercial multi-walled carbon nanotubes and graphene flakes, with N, P, B, and S atoms, through a simple mechanochemical treatment with appropriate precursors, namely melamine, triphenylphosphine, boric acid, and elemental sulphur, followed by thermal treatment in

an inert atmosphere. Heteroatom-doped carbon nanotubes and graphene flakes with distinct surface chemistry and enhanced reactivity, were properly characterized and tested towards the reduction of 4-NP in aqueous medium.

3.2 Experimental section

3.2.1 Materials and solvents

The reagents and solvents used during the experimental execution of this work were used as received. Multi-walled carbon nanotubes (sample denoted as MWCNT) were commercially obtained from Nanocyl S.A., Ref. 3100 MWCNT (>95% carbon purity; 9.5 nm average diameter). Commercial graphene (sample denoted as GC) was from Graphene Technologies (Lot #GTX-7/6-10.4.13). 4-Nitrophenol (≥99.5%), 4-aminophenol (≥99%), sodium hydroborate (98%), boric acid (99.97%), and triphenylphosphine (99%), were from Sigma-Aldrich. Elemental sulfur was from Merck (>99%). Potassium carbonate (98%) was from VWR Chemicals. Melamine was from Alfa Aesar (99%). N_2 gas used in the modification of the carbon materials was from Praxair (>99,998%).

3.2.2 Preparation of the heteroatom-doped carbocatalysts

The incorporation of heteroatoms (N, P, S and B) onto the pristine carbon materials MWCNT and GC was realized through mechanical treatments in a ball milling Retsch MM200 equipment, with the appropriate heteroatom precursors (Figure 3.1), followed by adequate thermal treatments under N_2 flow.

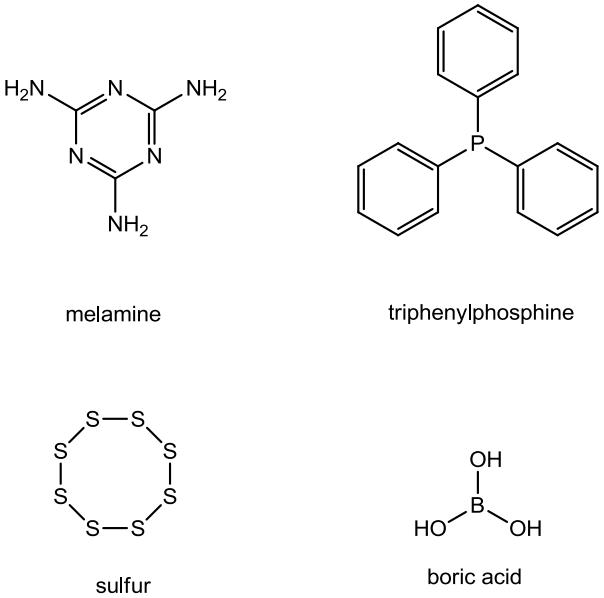

Figure 3.1 Heteroatom precursors used in the mechanical ball milling experiments.

In a typical experiment, 0.60 g of carbon material was mixed with 0.26 g of doping element using the appropriate precursor, and the mixture was ball-milled during 5 h at a constant frequency of 15 vibrations s^{-1}. Afterwards, the resulting materials were subjected to a thermal treatment under N_2 flow (100 cm^3 min^{-1}), at a rate of 10 °C min^{-1} until reaching the final temperatures, and kept at those temperatures during 1 h, cooled to room temperature under nitrogen atmosphere and stored in a desiccator. The precursors mass ratios and final temperatures for each sample are summarized in Table 3.1.

Table 3.1 Experimental conditions used in the preparation of the heteroatom-doped carbocatalysts.

Material	Precursors	Final temperature / °C
MWCNT_N6	0.60 g MWCNT + 0.39 g melamine	600
MWCNT_N8	0.60 g MWCNT + 0.39 g melamine	800
MWCNT_P10	0.60 g MWCNT + 2.20 g triphenylphosphine	1000
MWCNT_B10	0.60 g MWCNT + 1.49 g boric acid	1000
MWCNT_S6	0.60 g MWCNT + 0.39 g sulfur	600
GF_N6	0.60 g GF + 0.39 g melamine	600
GF_N8	0.60 g GF + 0.39 g melamine	800
GF_P10	0.60 g GF + 2.20 g triphenylphosphine	1000
GF_B10	0.60 g GF + 1.49 g boric acid	1000
GF_S6	0.60 g GF + 0.39 g sulfur	600

3.2.3 Catalytic studies of the heteroatom-doped carbocatalysts in the reduction of 4-nitrophenol

The catalytic reduction of 4-nitrophenol (4-NP) to 4-aminophenol (4-AP) was carried out at room temperature by monitoring the electronic spectra at 2 min intervals, using $NaBH_4$ as the reducing agent. The degradation of 4-NP was monitored by the absorbance decrease of the electronic band at λ = 400 nm due to nitrophenolate ion in basic media and development of a new electronic band at λ = 300 nm corresponding to the formation of 4-AP. In a typical experiment, 30.0 cm^3 of a 0.05 mM stock solution of 4-NP were transferred to a 50 cm^3 round bottom flask, and 56.7 mg of $NaBH_4$ were added. At this stage, the electronic band at λ = 400 nm remained unaltered until addition of the carbocatalysts. The reactions were started with the addition of the carbocatalysts (10 mg) and stirred constantly at room temperature. At 2 minutes intervals, an aliquot (1 cm^3) was taken directly from the reaction mixture with a hypodermic syringe, filtered through a 0.1 µm Nylon membrane filter, and the corresponding electronic spectra was monitored in an Agilent 8453 UV-Visible

spectrophotometer, in the range 200 – 800 nm, with a 1 nm resolution. After each catalytic cycle, the catalysts were filtered, washed with ultrapure water several times to remove the remaining substrate, reaction product and oxidant. The recovered catalysts were dried at 110 ˚C overnight under vacuum and reused in a new reaction under identical experimental conditions, with readjustment of all quantities, without changing the molar ratios and reaction concentrations. Adsorption of 4-NP substrate onto the carbocatalysts was also evaluated using similar catalytic reaction conditions, in the absence of $NaBH_4$ and with the addition of 100 mg of K_2CO_3 to 30 cm^3 of 0.05 mM stock solution of 4-NP.

3.3 Results and discussion

3.3.1 Materials characterization

XPS analysis was carried out to assess the composition of the doped carbon materials. The relative amounts of the different elements, C, O, N, P, B and S, were calculated from the corresponding peak areas and are shown in Table 3.2. As can be seen in Table 3.2, the XPS spectra of all the heteroatom-doped carbon materials indicated the presence of the corresponding doping elements in amounts ranging from 0.2 % of phosphorous in GF_P10, to 6.0 % of nitrogen in GF_N6. For the nitrogen-doped materials, the relative atomic percentages were 1.8 and 1.0 % for materials MWCNT_N6 and MWCNT_N8, respectively, whereas for the graphene flake counterparts, the percentages found were 6.0 and 5.8 % for GF_N6 and GF_N8, respectively. This result indicates that the nitrogen doping using melamine as precursor, was substantially more effective for the graphene flake materials. Moreover the nitrogen relative atomic percentages were lower for the materials subjected to thermal treatment at 800 ˚C (MWCNT_N8 and GF_N8), than those found for the materials subjected to thermal treatment at 600 ˚C (MWCNT_N6 and GF_N6).

The doping procedures using triphenylphosphine as phosphorous precursor, yielded materials with relative atomic percentages of 0.3 and 0.2 % of P, in materials MWCNT_P10 and GF_P10, respectively. The preparation of boron-doped carbon materials using boric acid as boron precursor resulted in materials with atomic percentages of 0.5 and 0.3 %, in materials MWCNT_B10 and GF_B10, respectively. Materials doped with sulphur showed atomic percentages of 0.7 and 0.9 %, for materials MWCNT_S6 and GF_S6, respectively.

Table 3.2 XPS surface atomic percentages for the pristine and heterotatom-doped carbon materials.

Material	Atomic %					
	C1s	O1s	N1s	P2p	B1s	S2p
MWCNT	98.7	1.3				
MWCNT_N6	94.7	3.5	1.8			
MWCNT_N8	98.1	0.9	1.0			
MWCNT_P10	98.5	1.2		0.3		
MWCNT_B10	97.5	2.0			0.5	
MWCNT_S6	98.6	0.7				0.7
GF	92.9	6.8	0.3			
GF_N6	91.1	2.9	6.0			
GF_N8	92.3	2.6	5.1			
GF_P10	97.3	2.5		0.2		
GF_B10	97.5	2.2			0.3	
GF_S6	97.1	2.0				0.9

Regarding the oxygen content after the different doping procedures, all the graphene flake materials show a decrease of the oxygen atomic percentage upon the doping procedures, whereas for the carbon nanotube materials there is also a decrease in the oxygen content, except for materials MWCNT_N6 and MWCNT_B10, which showed an increase in oxygen atomic percentage from 1.3 % in pristine MWCNT, to 3.5 and 2.0 %, respectively.

In order to assess the nature and relative amounts of the nitrogen functionalities present in the N-doped carbon materials, the deconvolution of the N1s high resolution XPS spectra was performed and shown in Figure 3.2. The relative atomic percentages obtained from the deconvolutions are summarized in Table 3.3.

As can be seen in Figure 3.2, the XPS N1s spectra of the N-doped carbon materials was deconvoluted into three main peaks that are assigned to pyridinic N (398.5 eV), pyrrolic N (400.1 eV), and quaternary N (401.6 eV).[19–21] Additionally, a fourth peak at 404.1 eV was found for materials MWCNT_N6, MWCNT_N8 and GF_N6, which is attributed to nitrogen oxide and/or nitrate species.[19]

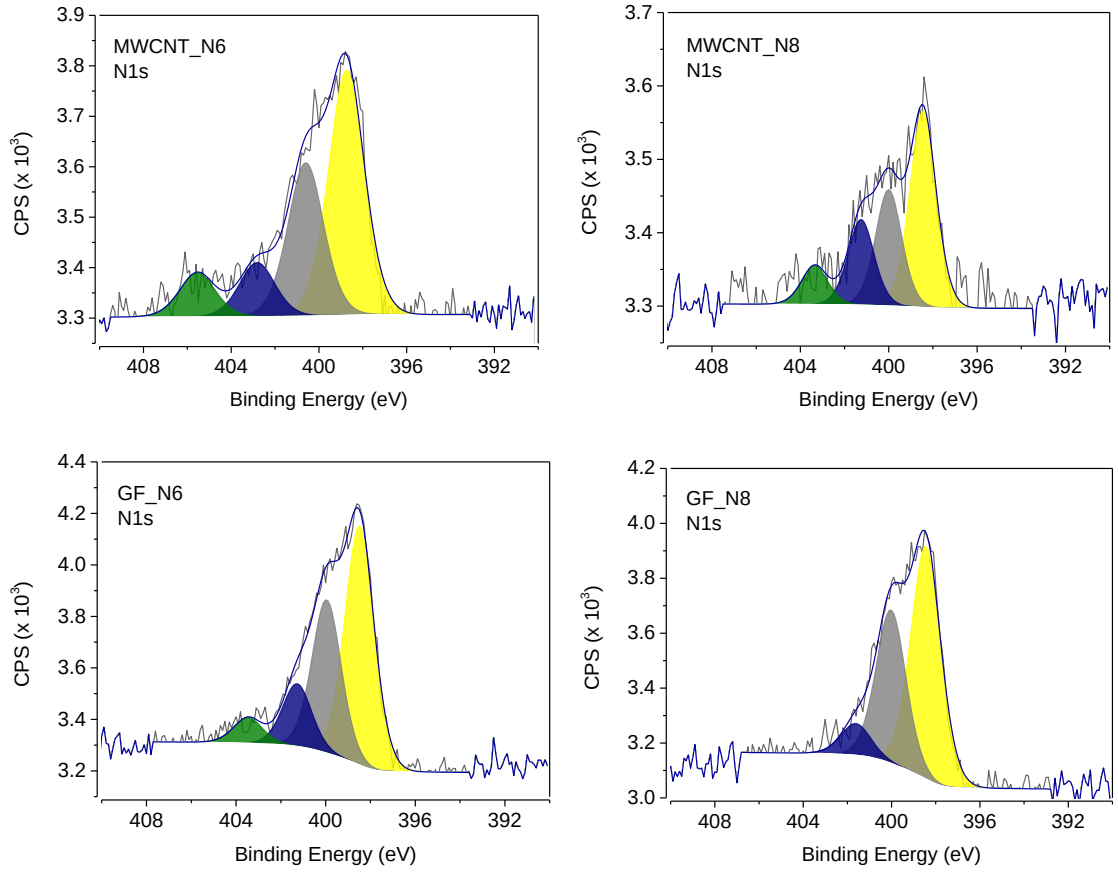

Figure 3.2 Deconvoluted N1s high resolution spectra of N-doped carbon materials.

Table 3.3 Relative atomic percentages of nitrogen presented in the XPS high resolution N1s spectra.

Material	% N			
	398.5 eV (pyridinic N)	**400.1 eV (pyrrolic N)**	**401.6 eV (quaternary N)**	**404.1 eV (N-oxides)**
MWCNT_N6	49.4	30.9	10.8	8.9
MWCNT_N8	44.9	26.6	19.6	8.9
GF_N6	49.7	31.9	13.0	5.4
GF_N8	55.7	36.7	7.6	

For all the prepared N-doped materials, the relative amounts of N-functionalities increase in the same order: [N-oxides/nitrates] < [quaternary N] < [pyrrolic N] < [pyridinic N]. However, for the carbon nanotube material treated at 800 ˚C, MWCNT_N8, there is a decrease in pyridinic and pyrrolic N, and an increase in

quaternary N, from 10.8 to 19.6 %, when compared to its counterpart material treated at 600 ˚C, MWCNT_N6. This indicates that the higher temperature during the thermal treatment favors the formation of substutional N functionalities in the carbon nanotube materials.

Interestingly, the graphene flake N-doped counterparts, exhibit the inverse pattern: for the graphene flake material treated at 800 ˚C, GF_N8, there is an increase pyridinic and pyrrolic N, and a decrease in quaternary N, from 13.0 to 7.6 %, when compared to its counterpart material treated at 600 ˚C, GF_N6. Also worth of notice is the inexistence of N-oxides/nitrates functionalities in material GF_N8.

The P2p high resolution XPS spectra of P-doped materials MWCNT_P10 and GF_P10, shown in Figure 3.3, revealed the existence of a single peak at 133.9 eV.

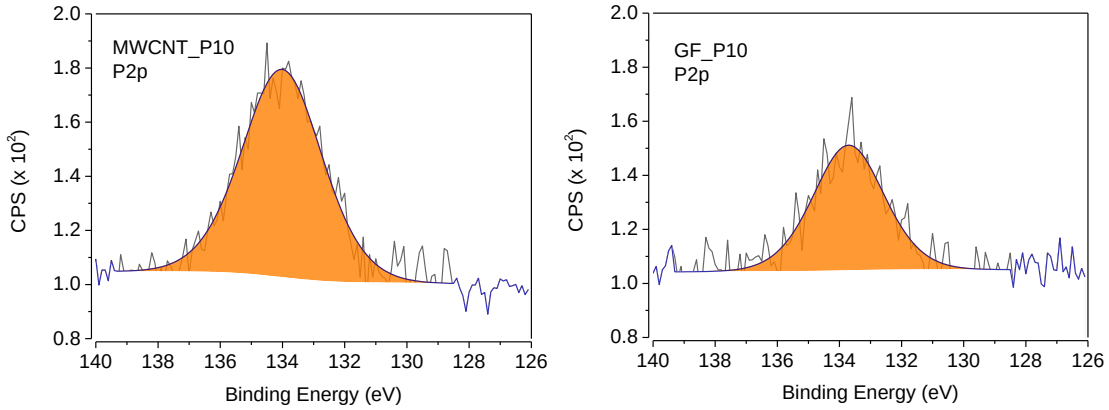

Figure 3.3 Deconvoluted P2p high resolution spectra of P-doped carbon materials.

At this binding energy, the P 2p peak has been attributed to P atoms in phosphate and in phosphite groups.[22,23] Taking into account that the peak corresponding to P atoms in P-C motifs would appear at 132.6 eV,[24] we estimate that the P atoms in MWCNT_P10 and GF_P10 are bound to graphitic carbon through R-O-$PO(OH)_2$ functionalities.

In order to obtain information about the types of boron functionalities introduced in materials MWCNT_B10 and GF_B10, the respective deconvolution of the B 1s high resolution spectra was performed and it is shown in Figure 3.4.

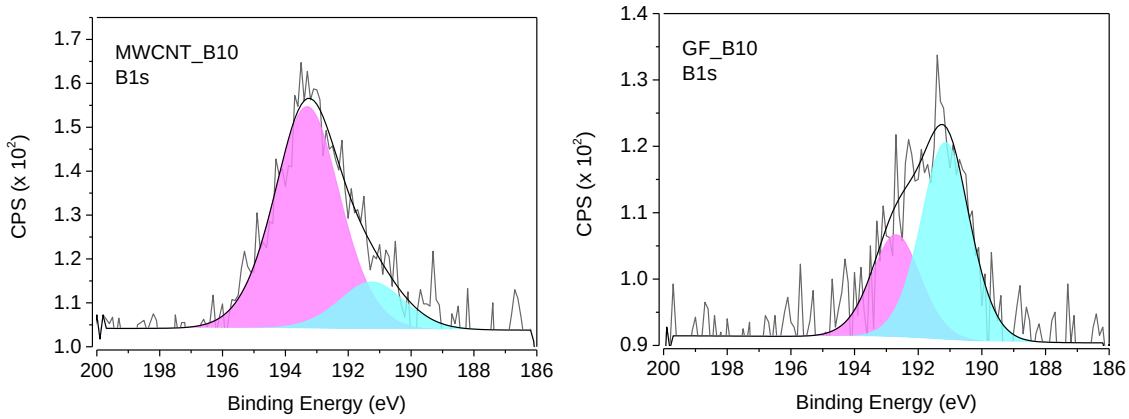

Figure 3.4 Deconvoluted B1s high resolution spectra of B-doped carbon materials.

The deconvolution revealed the existence of two peaks in both materials. The peak at 191.2 eV has been attributed to boronic groups (C-BO_2), whereas the peak at ~193 eV is assigned to B atoms in B_2O_3.[25,26] Table 3.4 shows the relative atomic percentages for the boron-containing groups found in materials MWCNT_B10 and GF_B10.

Table 3.4 Relative atomic percentages of boron presented in the XPS high resolution B1s spectra.

Material	% B	
	191.2 eV (boronic B in C-BO_2)	**193.0 eV (B in B_2O_3)**
MWCNT_B10	17.7	82.3
GF_B10	65.8	34.2

As can be observed in Table 3.4, material GF_B10 shows a much higher percentage (65.8 %) of boronic B than MWCNT_B10 (17.7 %), as this type of functionality is easily formed when B adopts a low coordinated substitutional site along graphene edges and these sites are in much higher quantities in the GF material than in MWCNT. No substitutional boron was found in both materials, as the B-C corresponding B 1s peak is found at energies no higher than 189.6 eV.[25]

For the assessment of the types and relative amounts of sulphur functionalities, the deconvolution of the XPS high resolution spectra of materials MWCNT_S6 and GF_S6, was performed and shown in Figure 3.5.

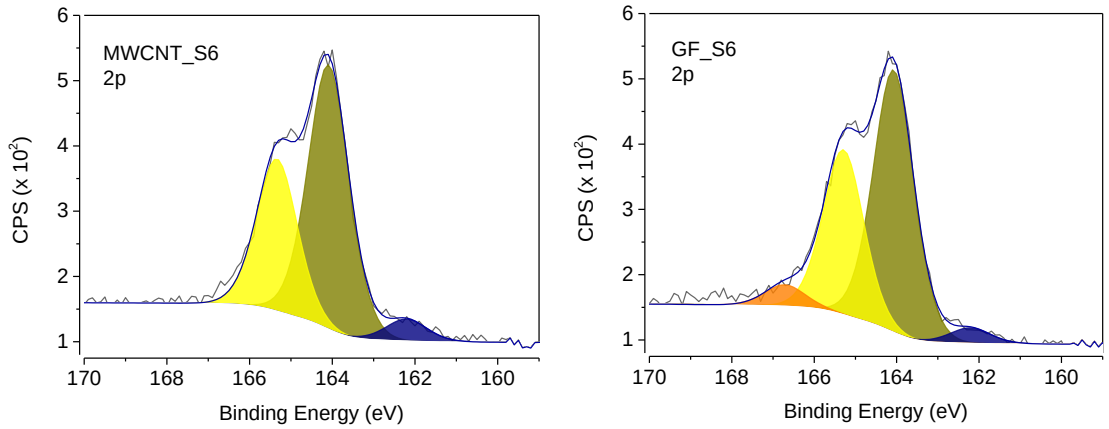

Figure 3.5 Deconvoluted S2p high resolution spectra of S-doped carbon materials.

The deconvolution revealed the existence of three peaks common to both S-doped carbon materials: the peaks at 164.1 and 165.3 eV are attributed to the S $2p_{3/2}$ and S $2p_{1/2}$ doublet in thiophene-S (ΔE = 1.2 eV), and the peak at 162.3 eV is assigned to thiol groups. [27–29] For material GF_S6, a fourth peak at 166.7 eV was found, which corresponds to sulphate species.[28] The formation of sulphate groups solely in GF_S6 is probably due to initial higher oxygen percentage in GF when compared to pristine MWCNT. The relative atomic percentages of sulfur containing functionalities are shown in Table 3.5. The percentages found indicate that that S-doping was successfully accomplished through the formation of S-C bonds in both carbon materials.

Table 3.5 Relative atomic percentages of sulfur presented in the XPS high resolution S2p spectra.

Material	**% S**			
	162.3 eV (S in R-SH)	**164.1 eV (S $2p_{3/2}$)**	**165.3 eV (S $2p_{1/2}$)**	**166.7 eV (S in sulphates)**
MWCNT_S6	5.0	60.3	34.7	
GF_S6	3.4	56.5	35.5	4.6

The morphology of the pristine and doped carbon materials was analyzed by TEM and some examples of the obtained TEM micrographs are shown in Figure 3.6.

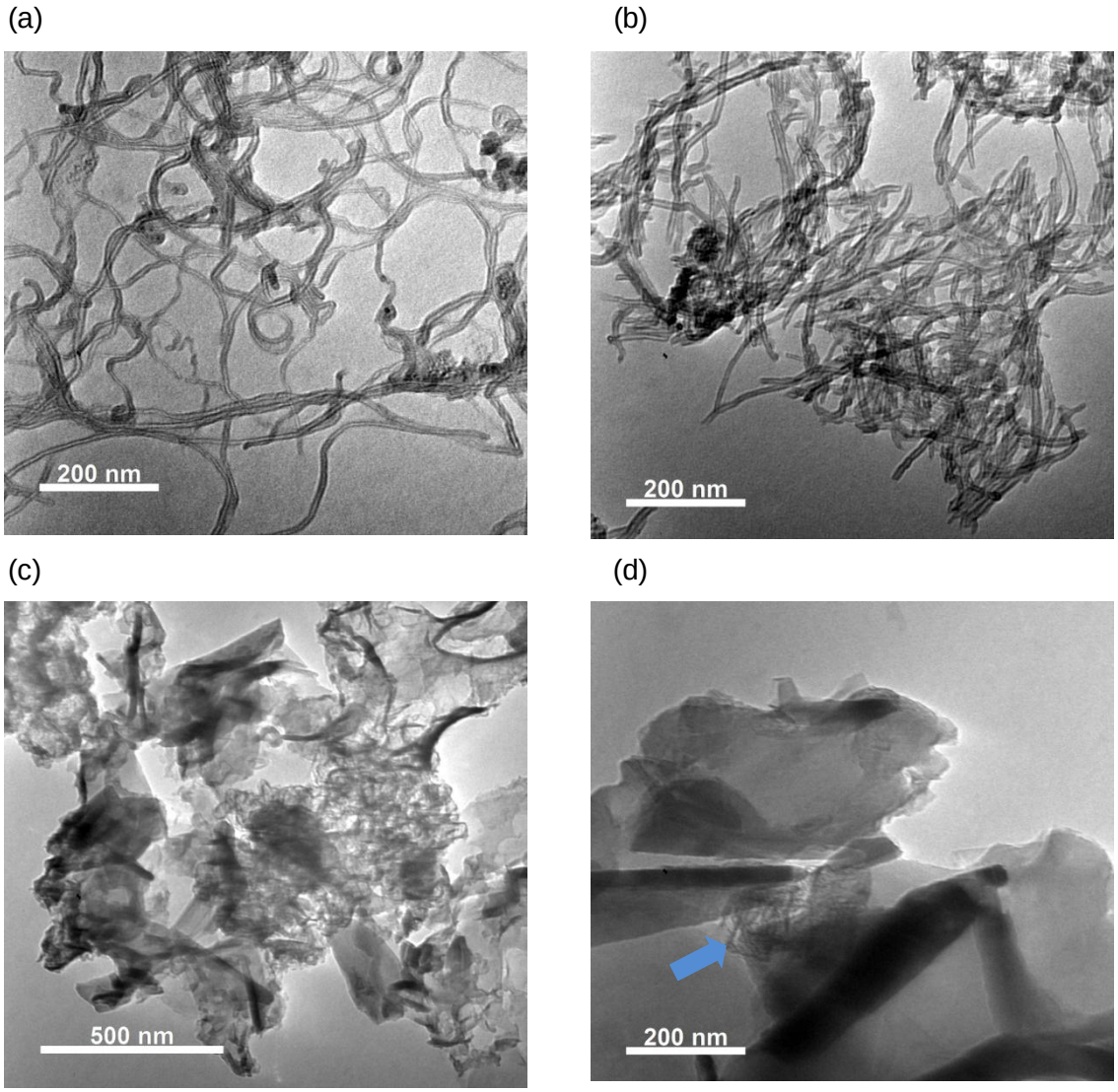

Figure 3.6 TEM micrographs of materials MWCNT (a), MWCNT_N8 (b), GF (c), and GF_S6 (d).

The micrograph obtained for material MWCNT (Figure 3.6a) shows that the thin multi-walled carbon nanotubes exist in well-defined tubular structures with lengths in the micron range. The image obtained for material MWCNT_N8 (Figure 3.6b), subjected to ball milling treatment and subsequent thermal treatment at 800 ˚C, shows some loss of the nanotubes initial structural integrity, as it is possible to observe shorter tubular domains, most probably due to breaking of the nanotubes during the milling process.

The acquired image of GF (Figure 3.6c) suggests that it is composed by wrinkled few-layer graphene sheets, whose sizes are in the range of hundreds of nanometres to one micrometre. The micrograph obtained for material GF_S6 (Figure 3.5a) shows that the ball milling and subsequent thermal treatment at 600 ˚C, did not promote any apparent significant structural changes in the doped material, as it is possible to

observe large wrinkled few-layer graphene sheet domains coexisting with smaller crystallites on top (marked with blue arrow).

Textural properties of the pristine and modified carbon material were evaluated by the corresponding N_2 adsorption–desorption isotherms performed at -196 ˚C, in order to assess the modifications promoted by the different doping procedures. Figures 3.7 and 3.8 depict the N_2 adsorption–desorption isotherms for MWCNT and GF materials, respectively, and Table 3.6 presents the calculated specific surface area, S_{BET}.

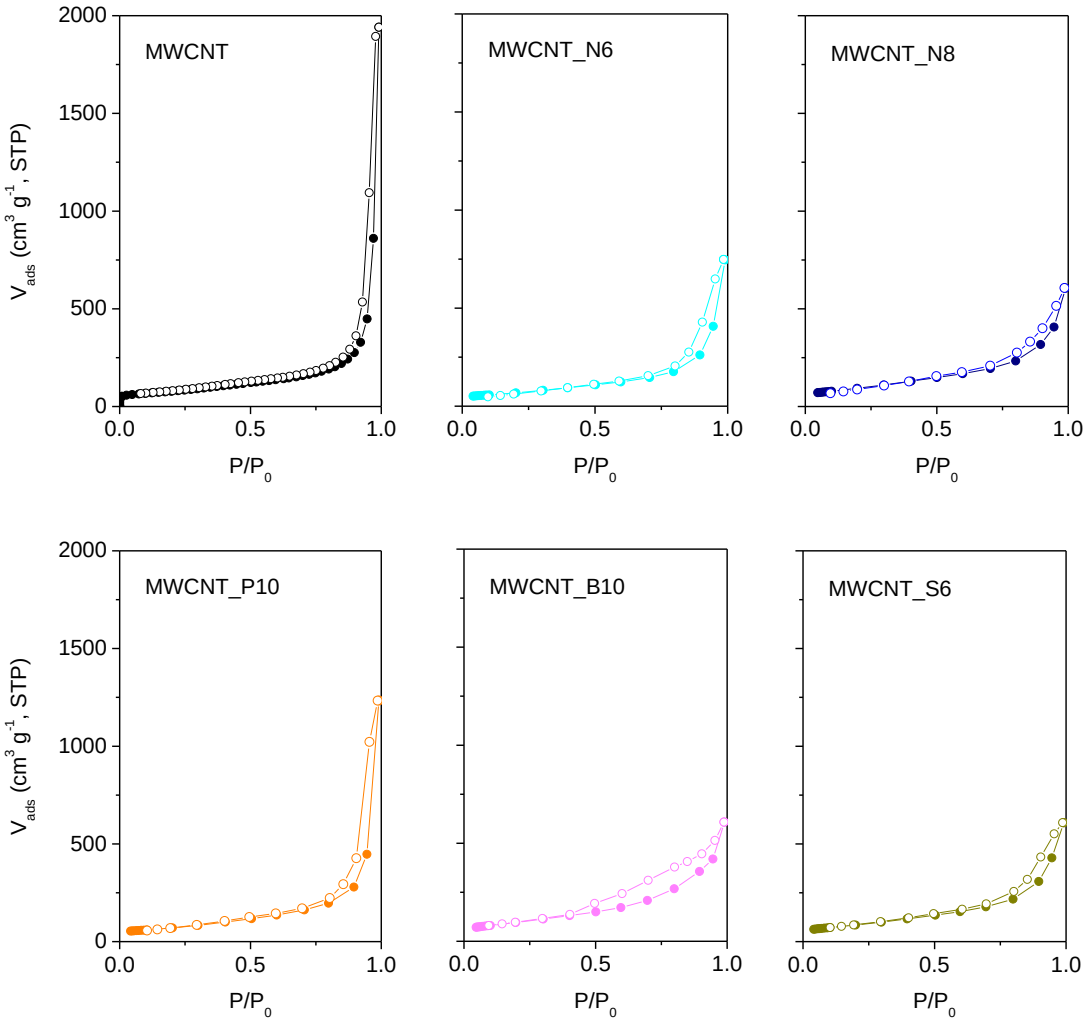

Figure 3.7 The nitrogen adsorption–desorption isotherms of the carbon nanotube materials at −196 ˚C (filled and unfilled symbols represent the adsorption and desorption processes, respectively).

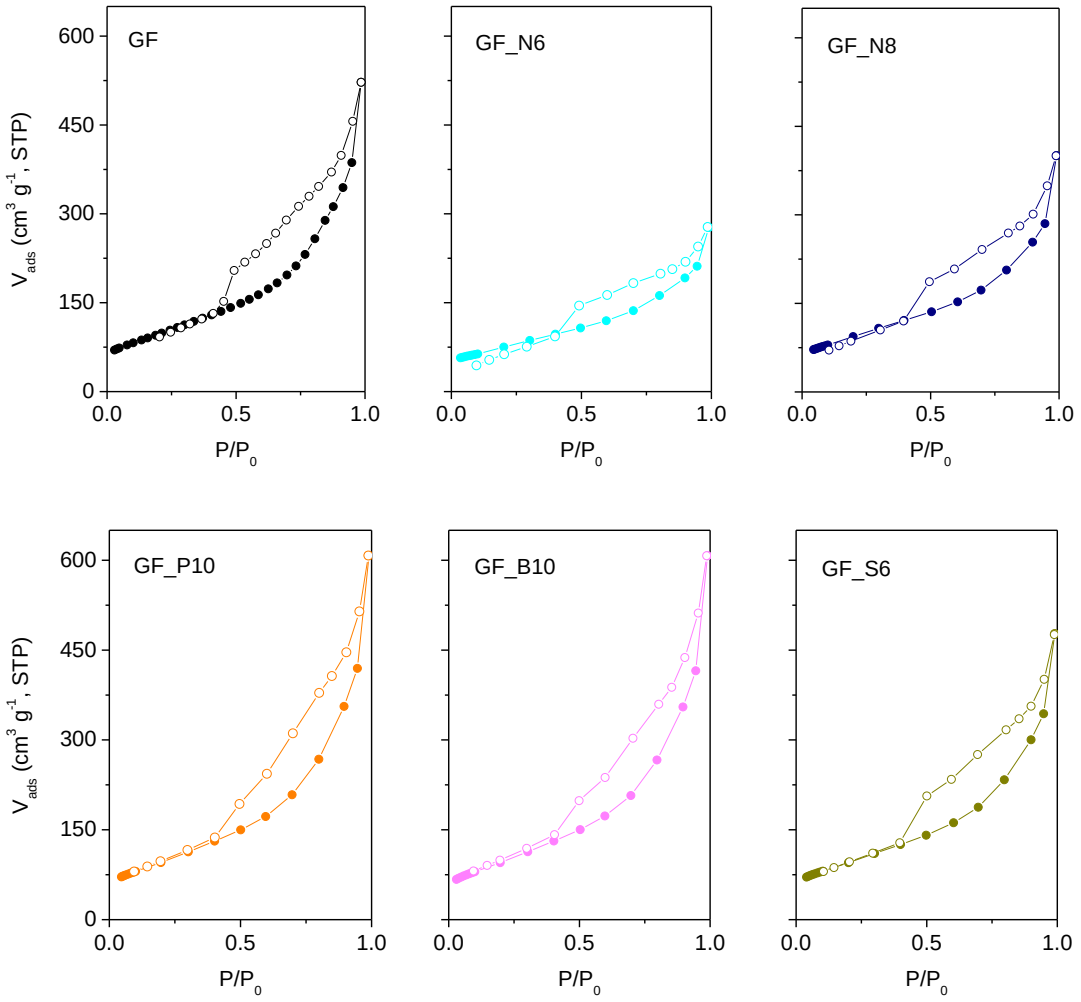

Figure 3.8 The nitrogen adsorption–desorption isotherms of the graphene flake materials at −196 ˚C (filled and unfilled symbols represent the adsorption and desorption processes, respectively).

The N_2 adsorption isotherms of all the carbon materials are typically of type II, accordingly to IUPAC classification,[30] which are characteristic of non-porous materials and represent unrestricted monolayer-multilayer adsorption. For the GF materials however, a distinct hysteresis loop is observed, which is characteristic of non-rigid aggregates of plate-like particles. For the doped carbon nanotube materials, there was an increase in the specific surface areas for materials MWCNT_N8, MWCNT_B10, and MWCNT_S6, and a decrease in S_{BET} for materials MWCNT_N6 and MWCNT_P10, upon the doping procedures. The S_{BET} increased from 277 m^2 g^{-1} in pristine MWCNT to 344, 334 and 310 m^2 g^{-1} in MWCNT_N8, MWCNT_B10, and MWCNT_S6, respectively. These results suggest that the doping procedures increased the access to the nanotubes inner cavities, through the breaking of the tubular structures, as seen in the TEM results for material MWCNT_N8.

Table 3.6 Apparent BET surface areas of the carbon materials derived from the nitrogen adsorption–desorption isotherms at −196 ˚C.

Material	S_{BET} (m^2 g^{-1})
MWCNT	277
MWCNT_N6	244
MWCNT_N8	344
MWCNT_P10	258
MWCNT_B10	334
MWCNT_S6	310
GF	352
GF_N6	267
GF_N8	336
GF_P10	346
GF_B10	345
GF_S6	341

In materials MWCNT_N6 and MWCNT_P10, the S_{BET} decreased from 277 m^2 g^{-1} in the pristine material to 244 and 258 m^2 g^{-1}, respectively. Taking into account that the ball milling treatment was the same for materials MWCNT_N6 and MWCNT_N8, we rationalize that the thermal treatment at 600 ˚C was not as effective as the thermal treatment at 800 ˚C in the removal of the residues originated from the decomposition of the ball milled melamine. As for material MWCNT_P10, the small decrease of S_{BET} may be related with some degree of aggregation between nanotubes promoted by triphenylphosphine.

For the graphene flake materials, there was a decrease in the S_{BET} for all doped materials, when compared to the original GF. The specific surface areas decreased from 352 m^2 g^{-1} in GF to 267, 336, 346, 345, and 341 m^2 g^{-1}, in GF_N6, GF_N8, GF_P10, GF_B10, and GF_S6, respectively. This decrease may be due a higher degree of agglomeration within the doped graphene flake crystallites, induced by the ball milling procedures. The more pronounced S_{BET} decrease observed in material GF_N6 follows the same rationale of that of material MWCNT_N6 and hence justify the higher surfaces areas obtained for the counterpart materials treated at 800 ˚C. The specific surfaces areas obtained for the GF materials allow the estimation of the average number of layers per crystallite, when comparing them the theoretical value of 2630 m^2 g^{-1} calculated for single layer graphene.[31] As such, the average number of layers are 7, 10, 8, 8, 8, and 8 for the GF, GF_N6, GF_N8, GF_P10, GF_B10 and GF_S6 materials, respectively.

In order to gain further insights into the structural modification introduced by the different doping procedures on the graphene flakes, these materials were further studied by XRD. All the XRD patterns collected and shown in Figure 3.9 show peaks at 2θ angle 26.1˚ and 43.1˚, corresponding to (002) and (101) planes of graphitic framework, respectively.[32,33]

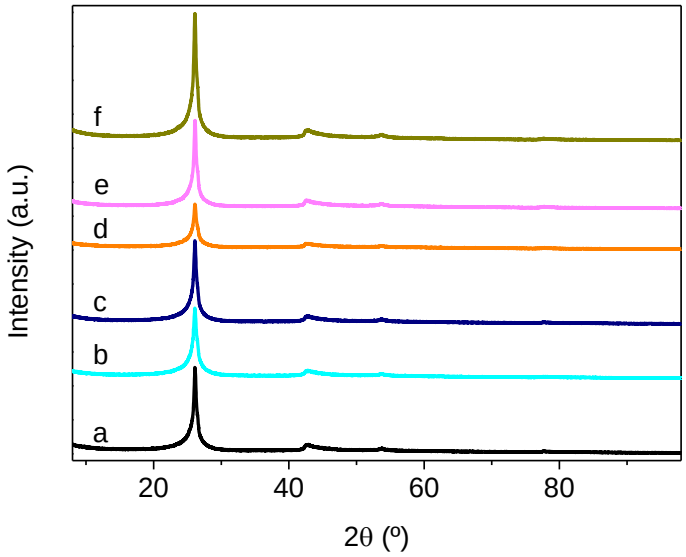

Figure 3.9 XRD patterns of: GF (a), GF_N6 (b), GF_N8 (c), GF_P10 (d), GF_B10 (e), and GF_S6 (f).

The peak at 2θ = 26.1˚ is related to the periodicity between the graphene layers and the second at 2θ = 43.1˚, to the periodicity within the graphene layer (honeycomb lattice at a single graphene sheet).[34] The intensity of XRD peaks has been associated with the extension of the corresponding domains.[35] In material GF_S6, the intensity of the (002) peak increases in comparison to original GF, indicating a gain of periodicity in the interlayer dimensions, whereas for materials GF_N6 and GF_P10, the peak intensity decreases, hence indicating a loss of interlayer periodicity. In materials GF_N8 and GF_B10, the intensity of the (002) peak remains roughly the same as in GF. Furthermore, due to the strong asymmetry observed in the (002) peaks of all XRD patterns, a Lorentzian deconvolution of the signals was performed, shown in Figure 3.10, and the deconvolution data is summarized in Table 3.7. The Bragg's equation was applied to the components of the deconvolution of the (002) peak in order to obtain the distance between graphene layers, for each crystallite type, which have different interlayer distances and a different number of graphene layers. The Scherrer's equation with a constant of 0.94 was applied to evaluate the crystallite size and number of layers per crystallite.[36]

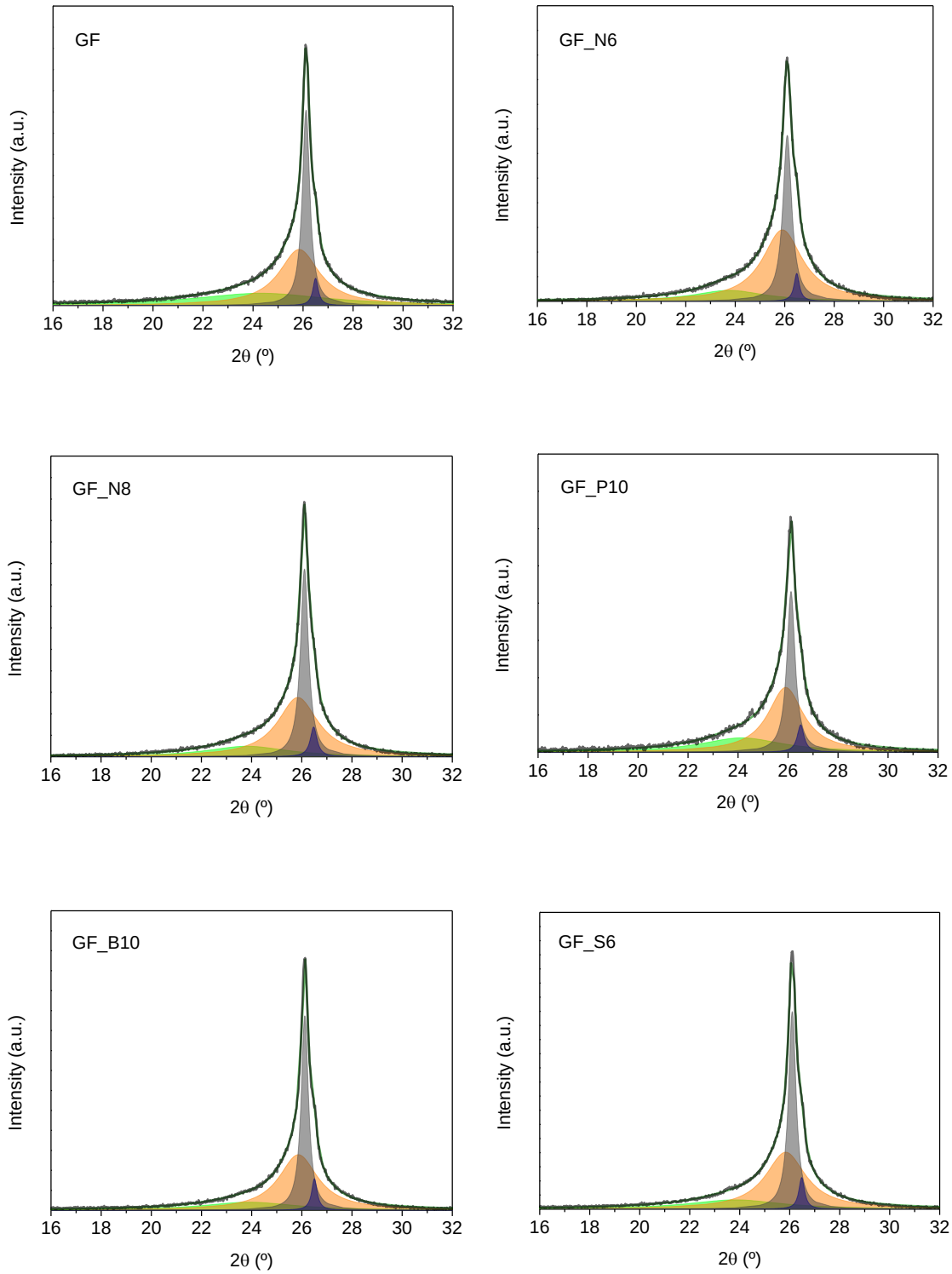

Figure 3.10 Deconvolution of the XRD (002) peak for the pristine and heretoatom-doped graphene flake materials.

Table 3.7 XRD data for pristine and heretoatom-doped graphene flake materials obtained from the deconvolution of the 002 peak.

Material	2θ / ˚	Interlayer distance / Å	Average no. layers	Peak area ratio / %	Weighted average no. layers[a]
GF	24.3	3.67	5	29.6	10
	25.8	3.46	14	41.2	
	26.1	3.42	70	26.5	
	26.5	3.37	99	2.7	
GF_N6	23.7	3.76	8	14.8	15
	25.9	3.44	14	54.7	
	26.1	3.42	59	27.7	
	26.5	3.37	99	2.8	
GF_N8	23.8	3.74	7	17.1	15
	25.9	3.44	14	48.6	
	26.1	3.42	67	30.3	
	26.4	3.38	80	4.1	
GF_P10	24.1	3.70	7	23.6	14
	25.9	3.44	15	46.2	
	26.1	3.42	63	26.5	
	26.5	3.37	78	3.7	
GF_B10	23.9	3.73	6	16.4	15
	25.9	3.44	14	48.4	
	26.1	3.42	72	31.3	
	26.5	3.37	95	3.9	
GF_S6	23.8	3.74	6	17.9	14
	25.8	3.46	4	47.4	
	26.1	3.42	67	31.0	
	26.5	3.37	95	3.7	

[a]Assuming that the areas of the XRD peaks are proportional to the no. of layers (which are stacked in different numbers to form crystallites of different sizes), the weighted average number of layers may be roughly estimated as follow: if one consider that 2.7 % of the layers are stacked as 1 crystallite of 99 layers, then the total number of layers is 3678; there will be 14 crystallites of 70 layers, 111 of 14 layers and 237 of 5 layers, which totals 363 crystallites. Thus, the average number of layers will be 3678/363 = 10 layers per crystallite.

Taking into account the peak area ratios of the different peak components, it was possible to estimate the weighted average number of layers for each material, namely 10, 15, 15, 14, 15 and 14 layers for materials GF, GF_N6, GF_N8, GF_P10, GF_B10

and GF_S6, respectively. This result is in reasonable agreement with the BET surface area analysis, which revealed 7, 10, 8, 8, 8, and 8 layers for the GF, GF_N6, GF_N8, GF_P10, GF_B10 and GF_S6 materials, respectively. Moreover, it is possible to observe a decrease in the peak areas corresponding to the highest interlayer distance to all the doped materials, indicating that the oxidation procedures induced the further stacking of the graphene flakes, which corroborates the specific surface areas obtained. It is also noteworthy that despite the existence of larger crystallites, more than 60% of the layers are not 3-D stacked since they show interlayer spacing values larger than 3.44 Å.

In order to gain some general structural information on the studied materials, Raman spectroscopy was employed. Figure 3.11 shows first and second order Raman spectra of the pristine and doped MWCNT and GF materials.

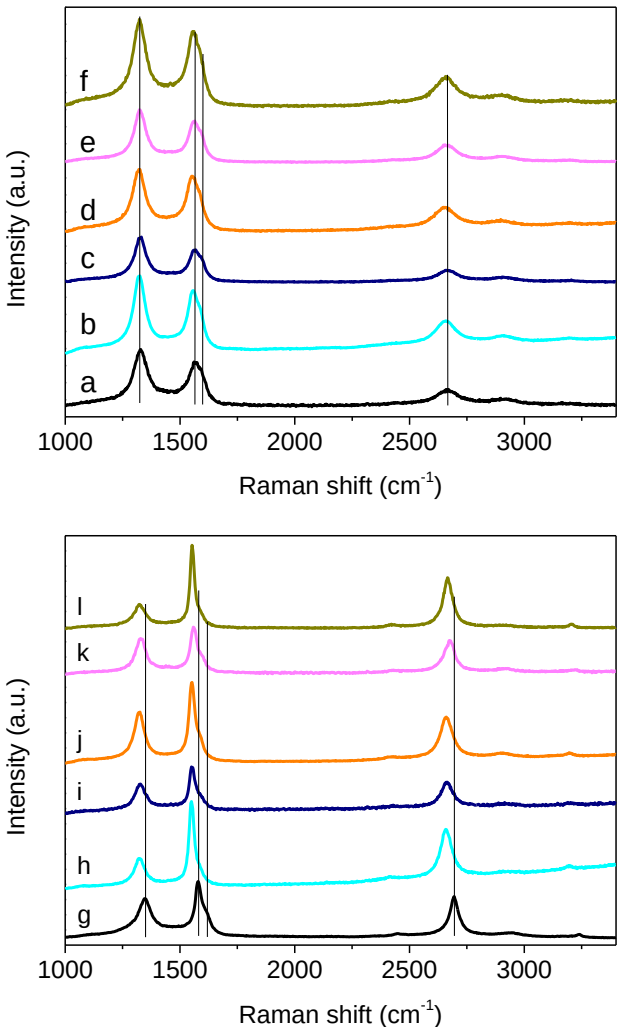

Figure 3.11 Raman spectra of MWCNT (a), MWCNT_N6 (b), MWCNT_N8 (c), MWCNT_P10 (d), MWCNT_B10 (e), MWCNT_S6 (f), GF (g), GF_N6 (h), GF_N8 (i), GF_P10 (j), GF_B10 (k), and GF_S6 (l).

The first-order Raman spectrum of all materials is characterized by strong bands at ~1350 and ~1580 cm^{-1}, known as D and G bands, respectively. Defect-free graphite would only show the G band, common to all sp^2 carbon systems, correspondent to the first-order scattering of the E_{2g} mode, whereas the D band is due to a phonon mode whose intensity is strictly connected to the presence of six-fold aromatic rings close to local lattice distortions (defects) of the graphitic network.[37] These distortions can be due, for example, to the presence of edges of graphitic planes, atomic vacancies or oxygenated groups. In the second-order spectra of original and oxidized graphene flakes, there is a strong peak at ~2700 cm^{-1}, assigned as the 2D mode and that is the overtone of the D peak. At ~1620 cm^{-1} it is also possible to identify a weak shoulder that corresponds to the D' mode.

For the doped graphene flake materials, however, a very distinct feature can be easily distinguished: a significant red shift of the D, G, and 2D bands. Figure 3.12 shows the red shift of the D, G, and 2D bands of the doped materials in comparison to the pristine GF.

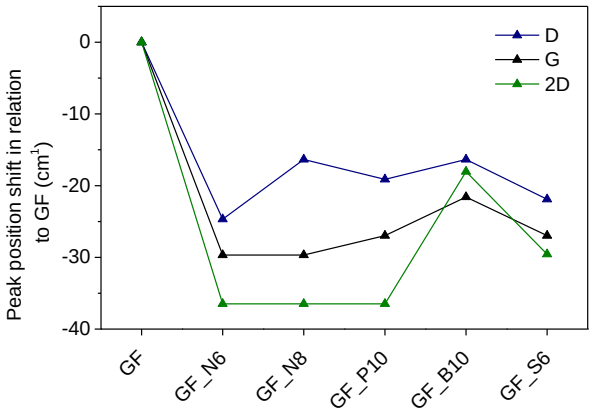

Figure 3.12 Raman red shift of the D, G, and 2D bands of the doped materials in comparison to the pristine GF.

It can be seen in Figure 3.12 that the red shift is larger for the 2D band in all doped materials, and that it is most pronounced for materials GF_N6, GF_N8, and GF_P10, with shifts of -36 cm^{-1}. This phenomenon is explained by the occurrence of tensile strain within the graphene flake materials. In fact, several authors reported red shifts in the Raman spectra of graphene materials as a result of the occurrence of tensile strain, further using Raman spectroscopy as a mapping tool for the determination of strain.[38–40] Therefore, it is possible to conclude that the ball milling treatments followed by thermal annealing, induced non-reversible strain in the prepared doped graphene flake materials, more so in materials GF_N6, GF_N8, and GF_P10.

The intensity ratio of the D and G bands is commonly used to estimate the disorder degree of graphitic materials.[41–44] Fig. 2.14 presents the I_D/I_G ratio for the pristine and modified MWCNT and GF materials, is presented in Figure 3.13.

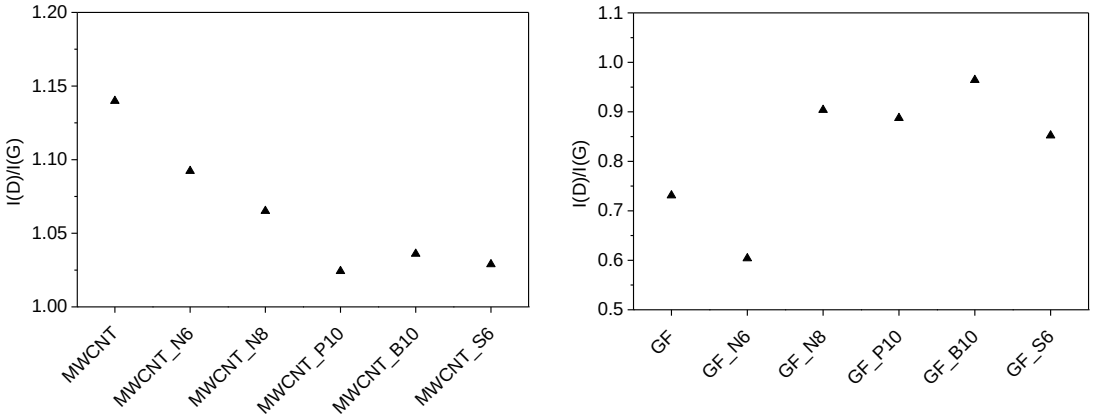

Figure 3.13 Calculated I_D/I_G ratio for the pristine and doped MWCNT and GF materials.

Notably, all the doped carbon nanotube materials presented a decrease in the I_D/I_G ratio, indicating a decrease in the number of defects on graphitic domains. Although their specific surface areas increased after the doping procedures, indicating the breaking of tubular structures during the ball milling procedures, an effect also corroborated by the TEM observations, the subsequent thermal annealing with the respective heteroatom precursors promoted the graphitization of the nanotube materials, thus reducing the overall amount of defects, as indicated by the lower I_D/I_G ratios.

As for the GF materials, with the exception of material GF_N6, all doped materials presented an increase in the I_D/I_G ratio, indicating that the doping procedures increased the amount of disorder in the doped materials. Interestingly, material GF_N6, having been subjected to the same ball milling treatment as material GF_N8, presented a lower I_D/I_G ration, when compared to pristine GF. Taking into account the obtained S_{BET} areas for GF_N6 and GF_N8, this result is related to the less efficient removal of the byproducts of the decomposition of melamine during the thermal treatment at a lower temperature (600 ˚C), suggesting that the presence of such residues inhibited the increase in the material disorder, as observed for material GF_N8.

3.3.2 Catalytic studies

The catalytic performance of the pristine and heteratom-doped carbon materials was evaluated in the reduction of 4-NP in water in the presence of $NaBH_4$, as schematized in Figure 3.14.

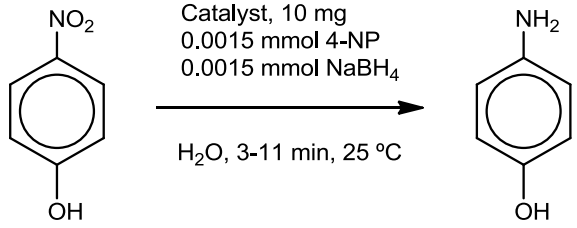

Figure 3.14 Reaction scheme of the studied catalytic experiments.

The carbocatalysts can effectively catalyze the reduction of nitro-compounds by acting as an electronic relay system, wherein the electron transfer takes place from donor BH_4^- to acceptor nitro groups. Upon the addition of $NaBH_4$, the 4-NP solution shows an absorption peak at λ = 400 nm due to the formation of the 4-nitrophenolate ion under alkaline conditions. The reactions were started with the addition of the catalyst into the solution and the peak intensity at 400 nm successively decreased and a new absorption peak appeared at 300 nm, indicating the formation of 4-AP.[45] Figure 3.15 shows a typical reaction profile obtained by UV-Vis spectrophotometry.

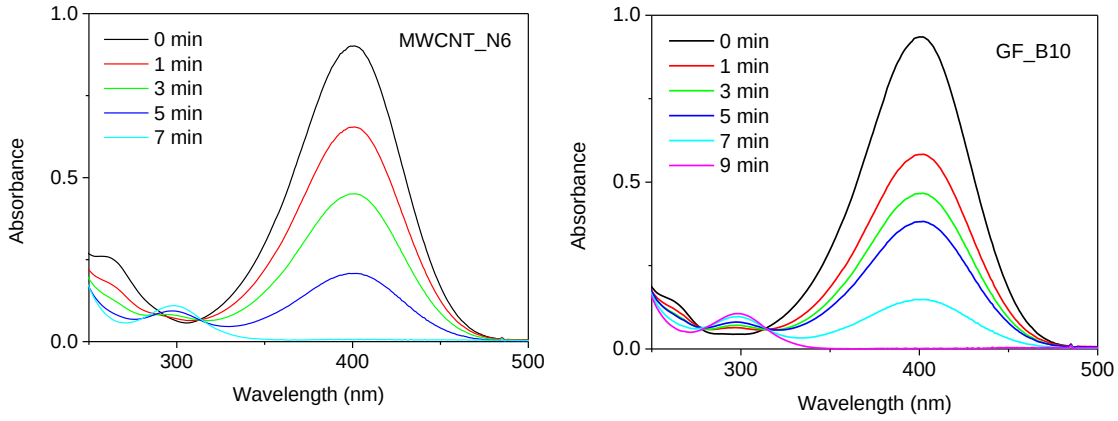

Figure 3.15 Typical UV-Vis reaction profiles for the carbon nanotube and graphene flake materials.

As can be seen in Figure 3.13, the UV-Vis spectra show an isosbestic point at 313 nm, suggesting that the catalytic reduction of 4-NP gives only 4-AP without any by-product.

Taking into account the the known adsorption capacities of the carbon materials, adsorption studies were performed, in order to establish its influence in the catalytic results obtained. Hence, the adsorption of 4-NP substrate onto the carbocatalysts was evaluated using similar catalytic reaction conditions, in the absence of $NaBH_4$ and with the addition of 100 mg of K_2CO_3 to 30 cm^3 of 0.05 mM stock solution of 4-NP, for the generation of 4-nitrophenolate ion, and the adsorption was followed.by UV-Vis. Figures

3.16 and 3.17 present the comparison between the absorbance measured in the catalytic reactions and in the adsorption experiments for the carbon nanotube materials and the graphene flake materials, respectively.

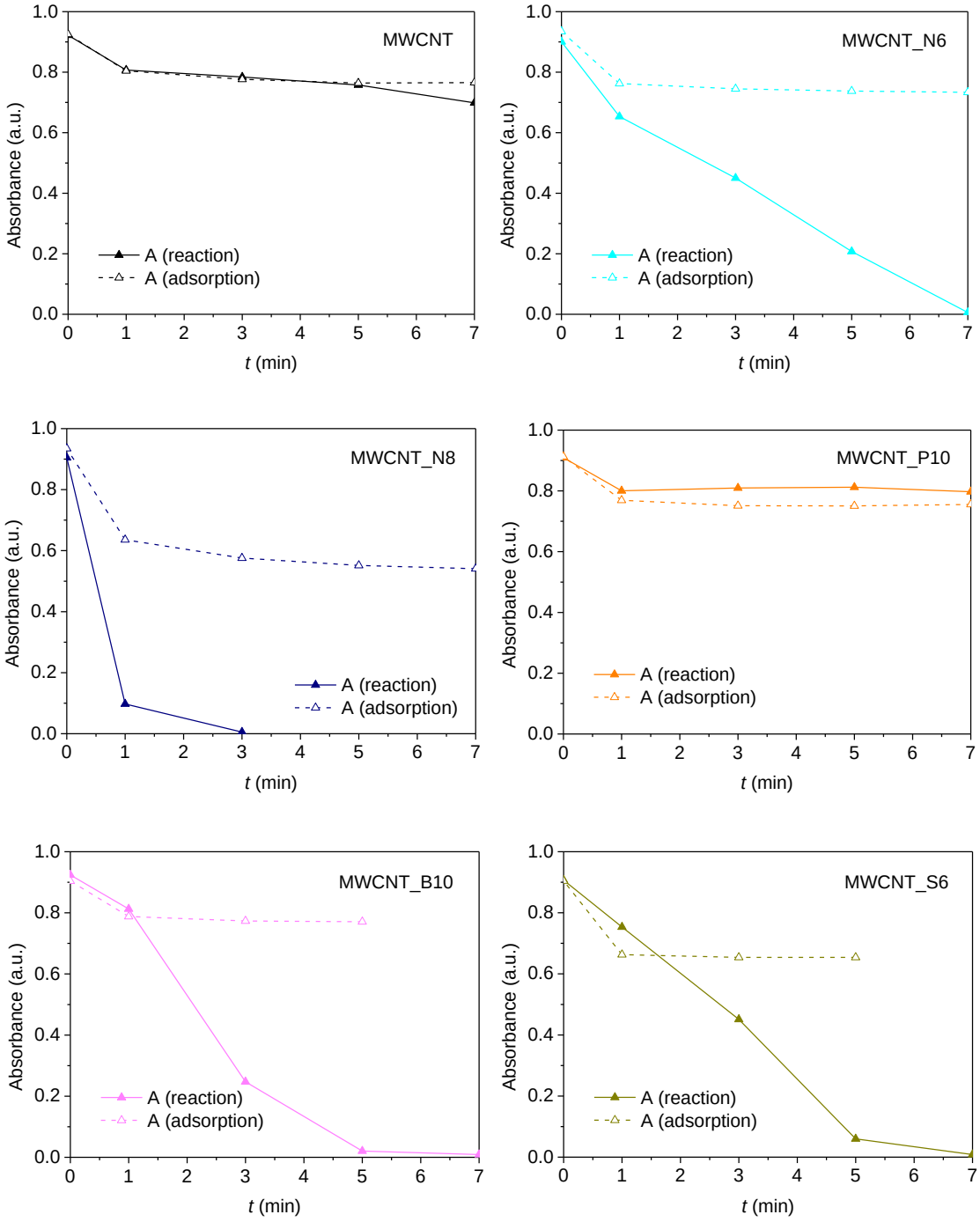

Figure 3.16 Measured absorbance in the catalytic and adsorption experiments, for the carbon nanotube materials.

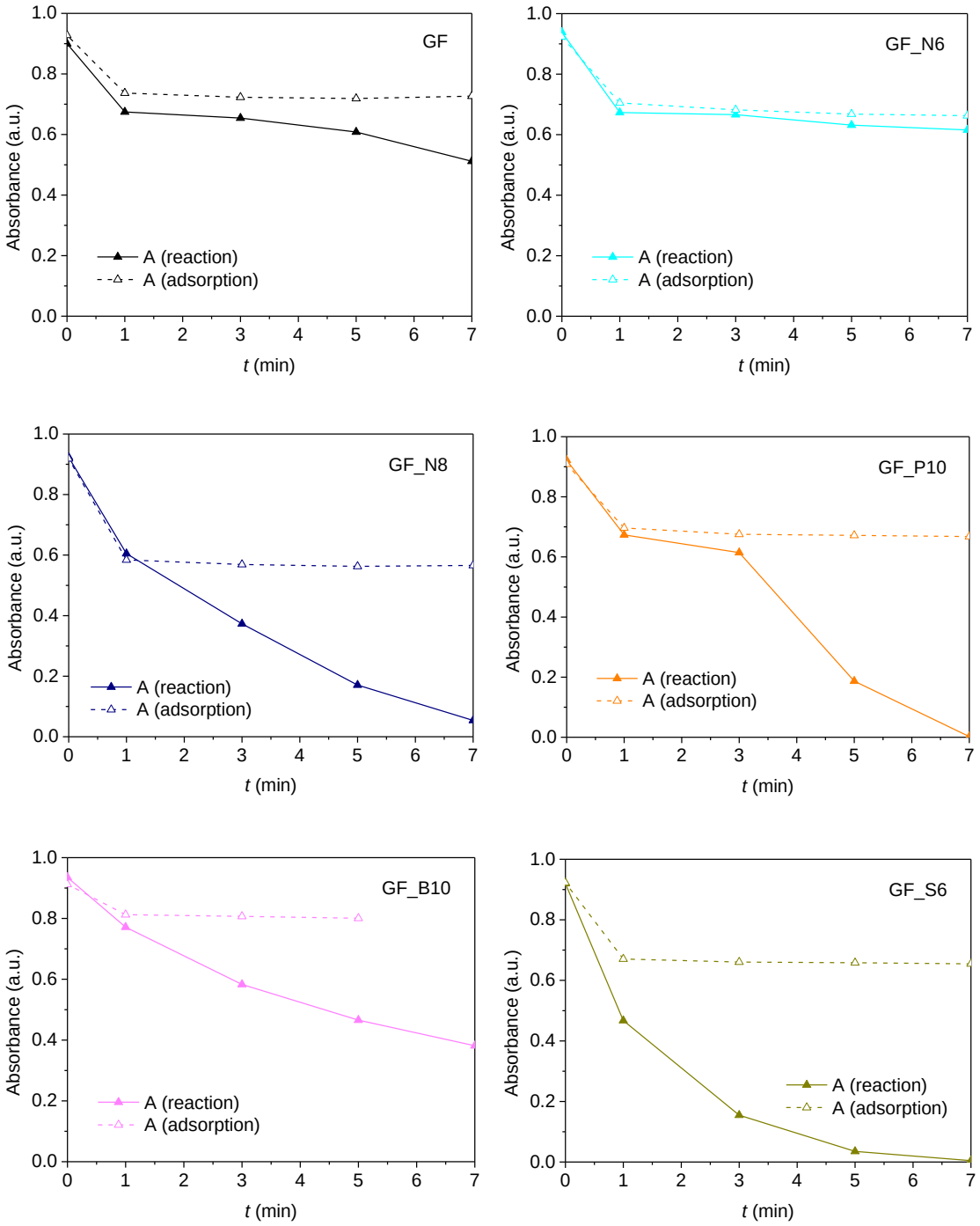

Figure 3.17 Measured absorvance in the catalytic and adsorption experiments, for the graphene flake materials.

In Figure 3.16 it is possible to observe that the absorbance measured in the reaction and in the adsorption profiles of materials MWCNT and MWCNT_P10 are almost coincident, indicating that these materials have negligible catalytic activity, and all the absorbance decrease observed is due to adsorption of 4-NP. For all other carbon nanotube materials, however, the absorbance due to adsorption reaches an equilibirum at t = 1 min, indicating that the reaction profiles obtained are due to the catalytic conversion of 4-NP to 4-AP.

For the graphene flake materials, coincident absorbance profiles for the reaction and adsorption experiments, are observed for materials GF and GF_N6. For the remaining materials, the absorvance due to adsorption reaches an equilibirum at t = 1 min.

As such, the conversion percentages were calculated based on the consumption of 4-NP, using a calibration curve for 4-NP (Appendix B), fitted with the appropriate concentrations and the calculations were performed taking into account the respective adorption data obtained. The results obtained in the reduction of 4-NP using the pristine and heteroatom-doped carbon materials are shown in Figure 3.18 and the correspondent data is summarized in Table 3.8.

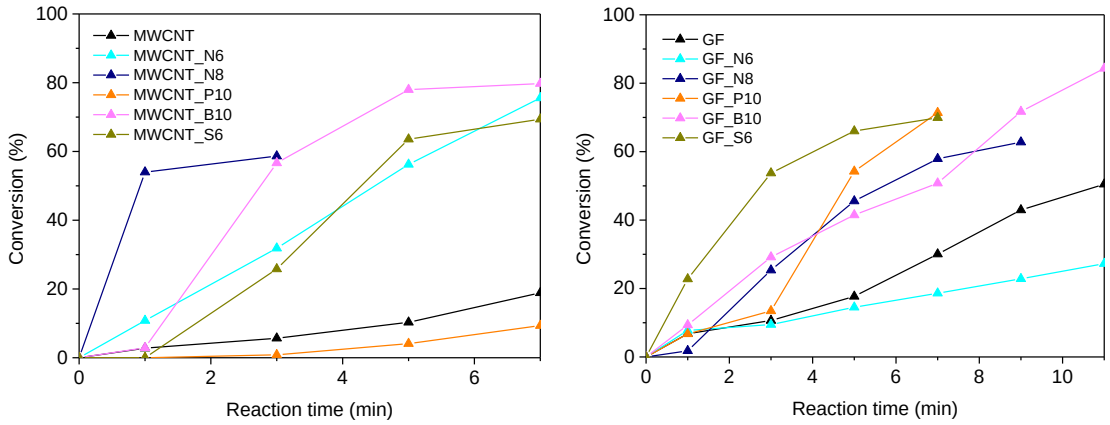

Figure 3.18 Conversions obtained for the reduction of 4-NP using the carbon materials as catalysts.

Table 3.8 Catalytic activity of the carbocatalysts in the reduction of 4-nitrophenol.

Material	Conversion (%)	Reaction time (min)	TON × 10^{-5} (mol g^{-1})	TOF × 10^{-5} (min^{-1})
MWCNT	19	7	3.0	0.4
MWCNT_N6	76	7	11.6	1.7
MWCNT_N8	59	3	9.0	3.0
MWCNT_P10	9	7	1.5	0.2
MWCNT_B10	80	7	12.9	1.8
MWCNT_S6	69	7	11.0	1.6
GF	50	11	7.8	0.7
GF_N6	27	11	4.4	0.4
GF_N8	63	9	10.0	1.1
GF_P10	71	7	11.5	1.6
GF_B10	84	11	13.7	1.2
GF_S6	70	7	11.1	1.6

As can be seen in Figure 3.18, both the pristine and doped carbon materials catalyse the reduction of 4-NP, acting as effective electronic relay systems. It can be immediately seen that, overall, the reaction times are lower for the carbon nanotube materials in regard to the graphene flake counterparts. The reaction times were chosen for appropriate comparison within each material type.

Analysis of Table 3.8 reveals that the most active doped carbon nanotube material, was MWCNT_B10, with a TOF of 1.8×10^{-5} min^{-1}, reaching 80 % conversion after 7 minutes. This is a significant increase over the performance of the undoped carbon nanotube material, which presented a TOF of 0.4×10^{-5} min^{-1}, and 19 % conversion with 7 minutes of reaction time. Material MWCNT_N8 presented the higher TOF of 3.0×10^{-5} min^{-1}, but its conversion was limited to 59 %. Materials MWCNT_N6, and MWCNT_S6 showed intermediate performances, with TOFs around 1.6×10^{-5} min^{-1}, but still better catalytic performances than the pristine material. Interestingly, material MWCNT_P10 showed lower conversion and TOF than the pristine material, which can be due to its lower specific surface area, as determined by N_2 adsorption-desorption at -196 ˚C.

As for the graphene flake materials, doped materials GF_S6 and GF_P10 yielded the higher TOFs of 1.6×10^{-5} min^{-1}, and ~70 % conversion within 7 minutes of reaction time. Material GF_B10 showed a lower TOF of 1.2 10^{-5} min^{-1}, but the higher conversion amongst the graphene flake materials - 84%. Material GF_N8 presented a slightly lower TOF of 1.1×10^{-5}. These four material yielded better catalytic performances than pristine GF, which presented a TOF of 0.7×10^{-5} min^{-1}, and 50 % conversion within 11 minutes of reaction time. Material GF_N6, however, showed a deterioration of catalytic activity, when compared to GF, with a TOF of 0.4×10^{-5} min^{-1} and 27 % conversion in 11 minutes of reaction time. Like its carbon nanotube counterpart, this material also showed a decrease S_{BET} area, thus corroborating the hypothesis that the lower temperature (600 ˚C) of the thermal treatment subsequent to the ball milling with melamine, yielded materials not free of residues resultant from the precursor decomposition, which in its turn, hindered their catalytic activity. Moreover, the materials ball milled with melamine and annealed at 800 ˚C, MWCNT_N8 and GF_N8, yielded the higher TOFs, indicating that the inclusion of nitrogen functionalities like pyrrolic, pyridinic, and substitutional nitrogen onto the carbon matrices yielded highly active sites for the reduction of 4-NP with $NaBH_4$.

In fact, all heteroatom doping procedures yielded carbocatalysts with enhanced catalytic activity towards the reduction of 4-NP, with the exception of the P-doped carbon nanotubes and the N-doped graphene flakes annealed at 600 ˚C . Sulphur and

phosphorous doping, however, yielded the best performing graphene flake carbocatalysts in terms of TOFs, while nitrogen doping with annealing at 800 ˚C, resulted in the carbon nanotube material with the higher TOF. Boron-doped carbon materials presented the higher calculated conversions, which can be due to the observed lower adsorption contribution to the reaction profiles.

The kinetic profiles of the 4-NP reduction using both nanocatalysts are presented in Figure 3.19, through the representation of $\ln(A_t/A_0)$ as a function of the reaction time, where A_t and A_0 are the absorbance of 4-NP at times t and 0 min, respectively.

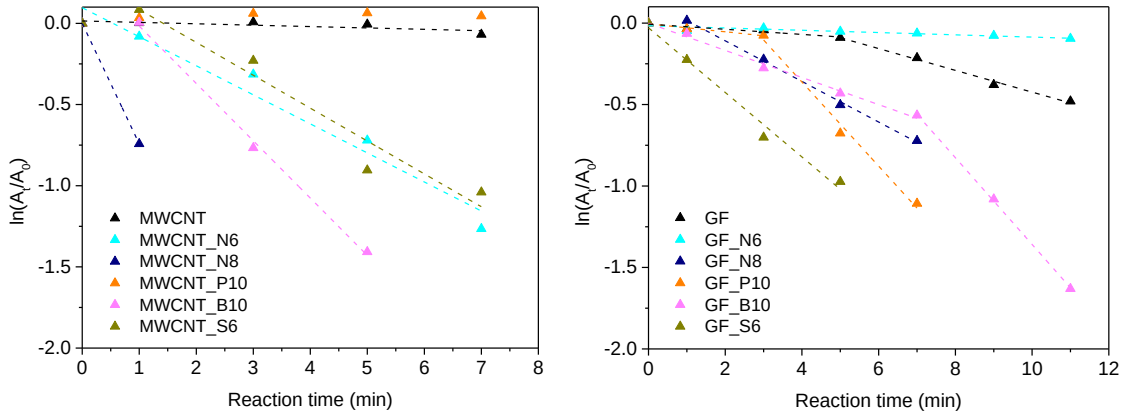

Figure 3.19 Pseudo-first order plots of 4-NP reduction catalyzed by the carbocatalysts.

In the experimental conditions used, the reduction rate is independent of $NaBH_4$ concentration (excess amount of $NaBH_4$ was used) and, consequently, the reduction reactions can be considered as being of pseudo-first-order. In this context, the pseudo-first-order rate constants, *k*, were calculated from the slopes of the linear ranges of the $\ln(A_t/A_0) = -kt$ plots and are summarized in Table 3.9. As can be seen in Figure 3.19, materials MWCNT, MWCNT_P10, and GF_N6 showed negligible catalytic activity. For the carbon nanotube materials, an induction period of 1 min is observed for materials MWCNT_B10 and MWCNT_S6, and the highest pseudo-first-order reaction rate calculated was for material MWCNT_N8, with a value of 0.742 min^{-1}.

For the graphene flake materials, an induction period of 1 min was observed for material GF_N8, and materials GF, GF_P10, and GF_B10 presented two reaction rates. The lower reaction rate (k_1) in the first minutes can be due to a competition between substrate reduction versus substrate/$NaBH_4$ adsorption in the carbon surface. Interestingly, material GF_S6, with a reaction rate of 0.198 min^{-1}, did not present neither an induction period or a second reaction rate.

Table 3.9 Kinetic parameters for the 4-NP reduction catalyzed by the carbocatalysts.

Material	Reaction time (min)	Induction period (min)	k_1 (min^{-1})	k_2 (min^{-1})
MWCNT	7		0.008	
MWCNT_N6	7		0.170	
MWCNT_N8	3		0.742	
MWCNT_P10	7		(~0)[a]	
MWCNT_B10	7	1	0.353	
MWCNT_S6	7	1	0.202	
GF	11		0.016	0.067
GF_N6	11		0.007	
GF_N8	9	1	0.125	
GF_P10	7		0.024	0.258
GF_B10	11		0.083	0.266
GF_S6	7		0.198	

[a]For material MWCNT_P10, the calculation of *k* was not possible due to the error introduced by the adsorption correction, which yielded a positive slope in the $\ln(A_t/A_0) = -kt$ plot; however this value is close to 0, as can be confirmed by its conversion % and TOF.

Furthermore, the carbocatalysts were recovered, washed with ultrapure water, vacuum dried, and reused in a new reaction under identical experimental conditions, without changing the molar ratios and reaction concentrations. Figure 3.20 and Table 3.10 show the results obtained in the catalysts recycling experiments. As can be seen in Figure 3.20 and Table 3.10, the conversion % remained practically inaltered for the active carbon nanotube materials, indicating that these doped carbocatalyst maintained their catalytic activity after 3 consecutive catalytic cycles.

As for the graphene flake materials, an overall decrease in catalytic activity was observed upon recycling, with the most promising materials, GF_P10 and GF_S6, presenting catalytic conversions for the 3rd cycle, of 44 and 39 %, respectively. We further attribute this decrease to an increase in adsorbed species from the reactional mixture on the graphene flakes, upon recycling. This indicates that the catalyst washing with ultrapure water solely, was not effective in the removal of such species, thus hindering catalytic active sites for the following cycle. Interestingly, this was not observed for the carbon nanotube materials, in which the same washing procedure was applied, and no loss of catalytic activity was observed, indicating that the washing was effective on its purpose.

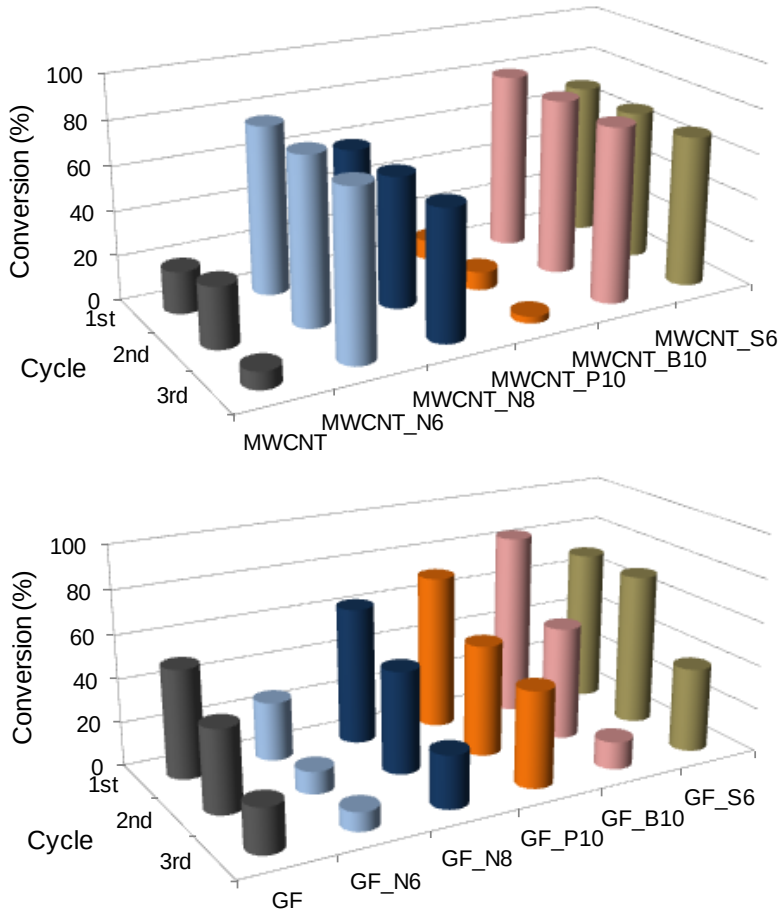

Figure 3.20 Recycling experiments for the carbocatalysts in the reduction of 4-NP.

Table 3.10 Catalytic activity in the recycling experiments of the carbocatalysts in the reduction of 4-nitrophenol.

Material	Conversion (%)		
	1st cycle	2nd cycle	3rd cycle
MWCNT	19	27	8
MWCNT_N6	76	75	74
MWCNT_N8	59	59	58
MWCNT_P10	9	8	3
MWCNT_B10	80	79	78
MWCNT_S6	69	68	68
GF	50	38	20
GF_N6	27	10	9
GF_N8	63	47	24
GF_P10	71	51	44
GF_B10	84	52	13
GF_S6	70	70	39

3.4 Conclusions

Multi-walled carbon nanotubes and graphene flakes were successfully doped with heteroatoms, namely N, P, B, and S, through a simple ball milling procedure followed by thermal treatment in an inert atmosphere.

The carbon materials characterization through XPS showed that: the nitrogen doping proceeded through the introduction of pyrrolic, pyridinic and quaternary N atoms on the graphitic structure; phosphorous atoms are bound to graphitic carbon in the prepared P-doped materials through R-O-$PO(OH)_2$ functionalities; B-doped materials showed the presence of boronic groups (C-BO_2) and B atoms in B_2O_3; and sulphur atoms found in S-doped materials were mainly tiophene-S type, while having a small percentage of S atoms in thiol groups.

TEM observations revealed some loss of the nanotubes structural integrety in material MWCNT_N8, probably due to breaking of the nanotubes during the milling process, and observation of materials GF and GF_S6 did not show any apparent significant structural changes in the doped material, as it was possible to observe large wrinkled few-layer graphene sheet domains coexisting with smaller crystallites in both materials.

Textural characterization through N_2 adsorption-desorption isotherms revealed that the doping procedures increased the carbon nanotubes specific surface areas, due to a higher access to the nanotubes inner cavities, achieved throught the breaking of the tubular structures. The doped graphene flakes presented an overall decrease in S_{BET}, probably due to a higher degree of agglomeration within the doped graphene flake crystallites, induced by the ball milling procedures, which was confirmed through XRD analysis. Notable exceptions to these trends were found for materials MWCNT_N6 and GF_N6, which showed an anomalous decrease in S_{BET}, indicating that the thermal treatment at 600 ˚C was not effective in the removal of the residues originated from the decomposition of the ball milled melamine.

Raman spectroscopy revealed that the doping procedures promoted the reduction of the overall amount of disorder in the carbon nanotube materials, whereas for all the doped graphene flake materials, the amount of disorder increased with the doping treatments.

The catalytic studies showed that all the doped carbon materials were active catalysts in reduction of 4-NP in the presence of $NaBH_4$, and that the modifications introduced by doping the carbon nanotubes and graphene flakes with heteroatoms, overall yielded catalysts with superior activity in regard to their pristine counterparts. The only exceptions were P-doped MWCNT and GF_N6, which present inferior

catalytic activity. Reusability experiments revealed no loss of catalytic activity up to three catalytic cycles for the doped carbon nanotubes, whereas the graphene flake materials showed some deterioration of catalytic performance due to ineffective washing between catalytic cycles. These results indicate that the doping of the carbon materials with heteroatoms (N, P, B and S), is a convenient and facile way to obtain metal-free carbocatalysts with superior performance in the reduction of 4-NP.

References

[1] S. Bawaked, N. F. Dummer, D. Bethell, D. W. Knight, G. J. Hutchings, *Green Chem.* **2011**, *13*, 127–134.

[2] Y. Mikami, A. Noujima, T. Mitsudome, T. Mizugaki, K. Jitsukawa, K. Kaneda, *Chem. Lett.* **2010**, *4*, 223–225.

[3] S. Go, M. A. Keane, *Catal. Commun.* **2008**, *9*, 475–481.

[4] T. Tsukinoki, H. Tsuzuki, *Green Chem.* **2001**, *3*, 37–38.

[5] Y. Guo, J. Li, F. Zhao, G. Lan, L. Li, Y. Liu, Y. Si, Y. Jiang, B. Yang, R. Yang, *RSC Adv.* **2016**, *6*, 7950–7954.

[6] V. Mohan, C. V Pramod, M. Suresh, K. H. P. Reddy, B. D. Raju, K. S. R. Rao, *Catal. Commun.* **2012**, *18*, 89–92.

[7] H. K. Kadam, S. G. Tilve, *RSC Adv.* **2015**, *5*, 83391–83407.

[8] A. Corma, P. Concepción, P. Serna, *Angew. Chemie - Int. Ed.* **2007**, *46*, 7266–7269.

[9] L. Gong, Y. Cai, X. Li, Y. Zhang, J. Su, J. Chen, *Green Chem.* **2014**, *16*, 3746–3751.

[10] P. M. Reis, B. Royo, *Tetrahedron Lett.* **2009**, *50*, 949–952.

[11] P. Serp, J. L. Figueiredo, *Carbon Materials for Catalysis*, John Wiley & Sons, **2008**.

[12] P. Trogadas, T. F. Fuller, P. Strasser, *Carbon* **2014**, *75*, 5–42.

[13] W. Y. Wong, W. R. W. Daud, A. B. Mohamad, A. A. H. Kadhum, K. S. Loh, E. H. Majlan, *Int. J. Hydrog. Energ.* **2013**, *38*, 9370–9386.

[14] Z. Yang, H. Nie, X. Chen, S. Huang, *J. Power Sources* **2013**, *236*, 238–249.

[15] U. N. Maiti, W. J. Lee, J. M. Lee, Y. Oh, J. Y. Kim, J. E. Kim, *Adv. Mater.* **2014**, *26*, 40–67.

[16] W. Shen, W. Fan, *J. Mater. Chem. A* **2013**, *1*, 999–1013.

[17] X. Kong, Z. Sun, M. Chen, C. Chen, Q. Chen, *Energy Environ. Sci.* **2013**, *6*, 3260–3266.

[18] S. Fujita, H. Watanabe, A. Katagiri, H. Yoshida, M. Arai, *J. Mol. Catal. A* **2014**, *393*, 257–262.

[19] M. Huang, H. Teng, *Carbon* **2003**, *41*, 951–957.

[20] F. Kapteijn, J. A. Moulijn, S. Matzner, H. Boehm, *Carbon* **1999**, *37*, 1143–1150.

[21] Y. Shao, S. Zhang, M. H. Engelhard, G. Li, G. Shao, Y. Wang, J. Liu, I. A. Aksay, Y. Lin, *J. Mater. Chem.* **2010**, *20*, 7491–7496.

[22] Y. Barbaux, M. Dekiouk, *App. Catal. A* **1992**, *90*, 51–60.

[23] H. S. Ghan, T. S. A. Hor, K. Tan, *Inorg. Chem. Acta* **1991**, *184*, 23–26.

[24] X. Zheng, X. Yang, J. Wu, C. Jin, J. Tian, R. Yang, *RSC Adv.* **2016**, *6*, 64155–64164.

[25] M. Cattelan, S. Agnoli, M. Favaro, D. Garoli, F. Romanato, M. Meneghetti, A. Barinov, P. Dudin, G. Granozzi, *Chem. Mater.* **2013**, *25*, 1490–1495.

[26] S. Agnoli, M. Favaro, *J. Mater. Chem. A* **2016**, *4*, 5002–5025.

[27] S. Yang, L. Zhi, K. Tang, X. Feng, J. Maier, K. Müllen, *Adv. Funct. Mat.* **2012**, 1–7.

[28] Y. Wang, B. Zhang, M. Xu, X. He, *RSC Adv.* **2015**, *5*, 86746–86753.

[29] L. Zhang, L. Ji, P. Glans, Y. Zhang, *Phys. Chem. Chem. Phys.* **2012**, *14*, 13670–13675.

[30] M. Thommes, K. Kaneko, A. V Neimark, J. P. Olivier, F. Rodriguez-reinoso, J. Rouquerol, K. S. W. Sing, *Pure Appl. Chem.* **2015**, *87*, 1051–1069.

[31] S. Park, R. S. Ruoff, *Nat. Nanotechnol.* **2009**, *4*, 217–224.

[32] A. B. Fuertes, S. Alvarez, *Carbon* **2004**, *42*, 3049–3055.

[33] T. Kim, I. Park, R. Ryoo, *Angew. Chemie - Int. Ed.* **2003**, *42*, 4375–4379.

[34] D. Reznik, C. H. Olk, D. A. Neumann, J. R. D. Copley, *Phys. Rev. B* **1995**, *52*, 116–124.

[35] J. P. Novais, S. L. H. Rebelo, B. Bachiller-baeza, M. E. Lipin, I. Rodríguez-ramos, A. Guerrero-ruiz, C. Freire, *Polyhedron* **2014**, *81*, 475–484.

[36] B. K. Saikia, R. K. Boruah, P. K. Gogoi, *J. Chem. Sci.* **2009**, *121*, 103–106.

[37] A. C. Ferrari, J. Robertson, *Phys. Rev. B* **2000**, *61*, 95–107.

[38] H. Zhou, F. Yu, D. Tang, M. Chen, H. Yang, G. Wang, Y. Guo, L. Sun, *Nanoscale* **2010**, *5*, 124–127.

[39] Z. H. Ni, T. Yu, Y. H. Lu, Y. Y. Wang, Y. P. Feng, Z. X. Shen, *ACS Nano* **2008**, *2*, 2301–2305.

[40] T. Yu, Z. Ni, C. Du, Y. You, Y. Wang, Z. Shen, *J. Phys. Chem. C* **2008**, *112*, 12602–12605.

[41] S. Stankovich, D. a. Dikin, R. D. Piner, K. a. Kohlhaas, A. Kleinhammes, Y. Jia, Y. Wu, S. T. Nguyen, R. S. Ruoff, *Carbon* **2007**, *45*, 1558–1565.

[42] J. I. Paredes, P. Sol, A. Mart, J. M. D. Tasc, *Langmuir* **2009**, *25*, 5957–5968.

[43] H. Kang, A. Kulkarni, S. Stankovich, R. S. Ruoff, S. Baik, *Carbon* **2009**, *47*, 1520–1525.

[44] M. S. Dresselhaus, A. Jorio, M. Hofmann, G. Dresselhaus, *Nano Lett.* **2010**, *10*, 751–758.

[45] Y. Lin, S. Wu, W. Shi, B. Zhang, J. Wang, Y. A. Kim, M. Endo, D. S. Su, *Chem. Commun.* **2015**, *51*, 13086–13089.

Chapter 4

Graphene flakes as dopants in perovskite-based solar cells

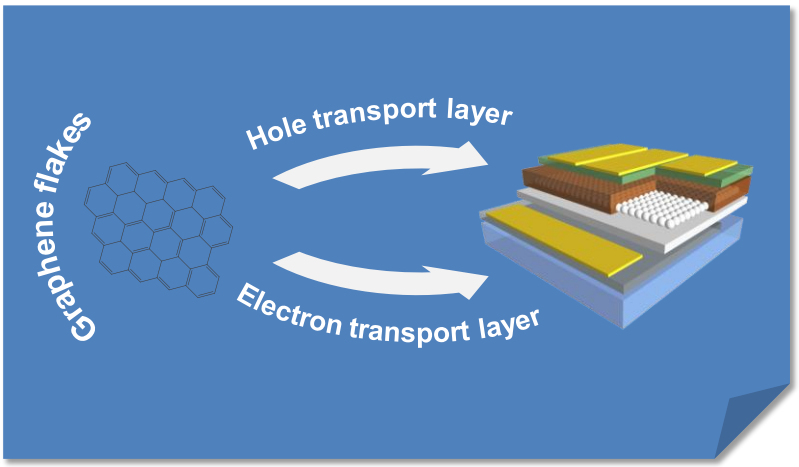

4

Graphene flakes as dopants in perovskite-based solar cells

Abstract

In this Chapter it is described the preparation and characterization of mesoscopic mixed halide perosvkite-based solar cells doped with commercial graphene flakes in the electron transport layer (ETL) and in the hole transport layer (HTL). Pristine devices with an average 4.88 % power to current efficiency (PCE) were successfully prepared, and their *I-V* measurements were used as a benchmark for the doped devices. Graphene flakes were characterized through TEM observations, N_2 adsorption-desorption at -196 ˚C, and XRD, and introduced in the ETL through two different strategies: by mixing different percentages of GF with the mesosporous TiO_2 precursor dispersion (method A), and by consecutively spin coating GF dispersions on top of the sintered TiO_2 layer (method B). The doping of the ETL through method A resulted in devices with efficiencies below 1 %, which was attributed to extensive exciton quenching promoted by GF within the mesoporous TiO_2 layer, as indicated by the concomitant decrease in the shunt resistance with the increase in GF amount. This may be due to the large agglomerates of GF observed by TEM, and/or to the high number of layers of the GF crystallites, as evidenced by TEM, N_2 adsorption-desorption, and XRD. Method B resulted in devices that revealed an overall inferior PCE, with averaged efficiencies of 3.24, 2.39, 3.68, and 3.55 % for devices spin coated with GF dispersion one, two, three, and four times, respectively. Strong hysterese was observed in the *I-V* plots of the doped devices, and its intensity increased with the amount of GF doping. This was atrributed to changes in charge carrier extraction efficiency at the carrier-selective contact, introduced by GF doping. The device doped with GF in the HTL showed a strongly decreased PCE, with an efficiency of 0.89 %. A decrease which was attributed to the overextension of the oxidized state of spiro-OMeTAD caused by the presence of GF, leading to a detrimental effect on its hole transport ability and loss of efficiency. Stability studies of the pristine solar cells were carried out, regarding the aging of the devices in a dry and dark environment, during 100 days, and an increase from 4.88 to 6.89 % PCE was observed after 100 days of

desiccant exposure in the dark, which can be related to absorption of residual solvent molecules and enhancement of the settling of the spiro-OMeTAD layer, and crystallization of the perovskite layer.

4.1 Introduction

It is widely accepted that direct conversion of the sun's energy into electricity is an unlimited clean and renewable resource that has great potential to address increasing energy demands and environmental pollution issues.[1,2] The big challenge for renewable solar energy conversion is to reduce production costs and maximize the efficiency. Although almost 90% of the commercial photovoltaic (PV) production is based on crystalline silicon (Si) solar cells which can deliver a power conversion almost ~90% of the commercial photovoltaic (PV) production is based on crystalline silicon (Si) solar cells which can deliver a power conversion efficiency (PCE) of approximately 20% under full-sun illumination.[3] Perovskite based solar cells have attracted great attention from the PV research community due to their extraordinary light-harvesting characteristics. Since the pioneering work by Kojima *et al.*[4] in 2009, the implementation of organic–inorganic lead halide perovskite based light absorbers into solid-state solar cells has brought significant breakthroughs in low-cost PVs. Remarkably, the progress of state of the art PSCs has been astounding and the highest energy conversion efficiency of 22.1 % was recently reached in early 2016.[5]

Graphene has gathered tremendous interest both in fundamental science and potential applications due to its unique structure and remarkable properties such as excellent conductivity, high electron mobility, superior chemical stability and large surface to volume ratio.[6–11] Moreover, the application of graphene in combination with semiconductor materials presents the possibility to possess simultaneously excellent adsorptivity, transparency, conductivity, and controllability, which could enhance the photoelectrochemical performance. In fact, lots of impressive results have been reported, where graphene and its derivatives were used as dopants in the different solar cells components, such as the electrodes, catalytic counter electrodes, light harvesting material, Schottky junction, electron transport layer, and hole transport layer.[12–14] Herein, we will focus on the doping of the electron transport layer of perovskite solar cells, specifically the perovskite/electron acceptor interface, and hole transport layer.

Zhu *et al.* synthesized single/few layer graphene quantum dots and inserted them between the layers of perovskite and TiO_2 nanoparticles, yielding mesoscopic solar cells with PCE of 10.15 %, which was considerably higher than that of pristine cells

(8.81 %).[15] This improvement in the cell performance was associated with the much faster electron injection upon graphene quantum dots doping.

Luo *et al.* prepared perovskite based solar cells with reduced graphene oxide (RGO) combined with spiro-OMeTAD as HTL, achieving a PCE of 10.6 %, greatly outperforming the undoped devices (PCE = 6.5 %).[16] Li *et al.* demonstrated the use of graphene oxide as an amphiphilic modifier to enhance the interface contact between perovskite and the HTL, which lead to an efficiency increase of 45.5 %, and an overall efficiency of 15.1 %, attributed to an enhanced charge collection efficiency resulting from improved contact between the perovskite and HTL and restrained charge recombination. [17]

In this Chapter, we present the study of the effect of doping the ETL of mesoscopic perovskite solar cells with commercial graphene flakes, at the perovskite/TiO_2 interface, and the doping of the HTL based on spiro-OMeTAD.

4.2 Experimental section

4.2.1 Materials and solvents

All of the reagents and solvents used during the experimental execution of this work were used without further purification. Commercial graphene flakes were from Graphene Technologies (Lot #GTX-7/6-10.4.13). TiO_2 paste (19% wt. TiO_2) was obtained from Dyesol, Ref. 18NR-T (20 nm average particle size). Lead(II) chloride (98%), titanium(IV) chloride (≥98%), hydroiodic acid (57% wt. in water, 99.99%), bis(trifluoromethane)sulfonimide lithium salt (LiTFSI, 99.95%), 4-*tert*-butylpyridine (t-BP, 96%), and FTO glass TCO22-15 (2.2 mm thick, sheet resistivity of 15 Ω/sq), were from Sigma-Aldrich. 2,2',7,7'-Tetrakis-(N,N-di-4-methoxyphenylamino)-9,9'-spirobifluorene (spiro-OMeTAD, >99.5%) was from Lumtec. Methylamine (40% in methanol) was from TCI Europe. Dimethylformamide (99.99%), chloroform (99.99%) and ethanol (absolute, 99.99%) were from Fisher. Zinc powder was from Merck. Gold wire (99.99%) was from Kurt J. Lesker.

4.2.2 Preparation of the pristine perovskite-based solar cells

CH_3NH_3I was synthesized by reacting 27.86 cm^3 of methylamine and 30 cm^3 of hydroiodic acid in a 250 cm^3 round bottom flask at 0 ˚C for 2 h with stirring. The precipitate was recovered by evaporation at 50 ˚C for 2 h. The product, methylammonium iodide CH_3NH_3I, was washed with diethyl ether by stirring the solution for 30 min, which was repeated three times, and then finally dried at 60 ˚C in a

vacuum oven for 24 h (η = 91.5 %; Anal. Calc. for CH_3NH_3I: C 7.56, H 3.80, N 8.81; Found: C 7.56, H 5.11, N 9.17).

A 2.356 M stock solution of $TiCl_4$ was prepared by adding liquid titanium tetrachloride reagent (~11 cm^3), drop-wise, under magnetic stirring to an approximate volume of 39 cm^3 ultrapure water, maintained at 0 °C, in an icewater bath. The drop-wise addition of $TiCl_4$ was controlled by using a hypodermic syringe fitted in a KD Scientific KDS 200CE infusion pump, at a rate of 1 cm^3 min^{-1}. The final concentration of Ti in the prepared stock solution was measured by a gravimetric method. The stock solution was stored at 3 °C.

The FTO layer of the TCO glass (2.5 × 2.5 cm) was first etched with Zn(0)/HCl to the desired geometry and then a compact hole-blocking layer of TiO_2 was formed on top of the FTO layer by spin coating a 2.356 M $TiCl_4$ solution at 5000 rpm (2000 rpm s^{-1}) for 60 s, followed by heating the substrates at 70 ˚C for 30 min; a second layer was deposited by coating a 2M $TiCl_4$ solution at 5000 rpm (2000 rpm s^{-1}), followed by heating the substrates at 70 ˚C for 30 min and sintering at 500 ˚C (10 ˚C min^{-1}) for 30 min.

Afterwards, a mesoporous TiO_2 layer deposition was deposited by spin coating a Dyesol 18NR-T suspension (1:4 wt.% in ethanol) at 2000 rpm (2000 rpm s^{-1}) for 60 s, followed by sintering the substrates at 500 ˚C (10 ˚C min^{-1}) for 1 h.

The $CH_3NH_3PbI_{(3-x)}Cl_x$ precursor solution was prepared by dissolving CH_3NH_3I and $PbCl_2$ in DMF (3:1 molar ratio, 40% wt.) at 60 °C for 12 h. This solution was then dripped on top of the TiO_2 film, left to soak for 20 s and then spun at 2000 rpm for 30 s (2000 rpm s^{-1}). The substrates were placed on a hot plate at 100 °C for 1 h to form crystalline $CH_3NH_3PbI_{(3-x)}Cl_x$.

A hole transport material precursor solution was prepared by dissolving 46 mg of spiro-OMeTAD in 0.5 cm^3 $CHCl_3$, and adding 14.4 µL 4-*tert*-butylpyridine and 8.75 µL of a LiTFSI solution (520 mg cm^{-3}) in ACN. The solution was spin coated onto the substrates at 2000 rpm (2000 rpm s-1) for 30 s, and the substrates were kept in a dry atmosphere in the dark overnight.

Finally, 60 nm of gold were thermally evaporated on the top of the cells through a shadow mask, under a vacuum level of ~1 × 10^{-6} torr. The prepared solar cells (SC_P1, SC_P2, and SC_P3) were stored in a 500 cm^3 hermetic container with 250 g silica gel inside, and in the dark.

All spin coating operations were performed at “Unidade de Micro e Nanofabricação do Centro de Materiais da Universidade do Porto” (MNTEC, Porto, Portugal) in a ISO7 10000 class Clean Room, using a Laurell WS-650 spin-coater.

Gold evaporation was performed in a Edwards Auto 306 thermal evaporator, also in the Clean Room.

It should be noted that the procedure optimization for the fabrication of efficient and stable mesoscopic solar cells, involved more than 50 device preparations, in which several parameters were varied, such as spin-coating speeds, type of TiO_2 precursor, composition of perovskite, molar ratios in the hole transport layer, etc.

4.2.3 Preparation of the doped perovskite-based solar cells

Graphene flakes (GF) have been introduced as dopants in the electron transport layer (ETL) through two different strategies, and as dopants in the hole transport layer (HTL). The procedures used in the preparation of the doped devices are as described for the pristine solar cells, unless stated otherwise.

GF as dopants in the ETL – method A: GF dispersions in ethanol were prepared and used in the preparation of the Dyesol 18NR-T suspension (1:4 wt% in GF dispersion in ethanol), to yield final mass percentages of 0.1, 0.5, 1.0, and 2.0 % wt. GF/TiO_2, and the dispersions were used in the preparation of the mesoporous TiO_2 layer of the doped solar cells SC_A0.1, SC_A0.5, SC_A1.0, and SC_A2.0, respectively. The dispersions were sonicated in an ultrasonic bath at 37 kHz for 1 h prior to the spin-coating procedures. The mesoporous layer was deposited by spin-coating the prepared dispersions at 2000 rpm (2000 rpm s^{-1}) for 60 s, followed by sintering the substrates at 500 ˚C (10 ˚C min^{-1}) for 1 h.

GF as dopants in the ETL – method B: a 0.1 mg cm^{-3} GF dispersion in DMF was prepared, sonicated for 1 h in an ultrasonic bath at 37 kHz, and spin-coated one, two, three, and four times on top of the sintered mesoporous TiO_2 layer, in the preparation of solar cells SC_B1, SC_B2, SC_B3, SC_B4, respectively. After each spin coating deposition, the substrates were placed on a hot plate at 100 ˚C for 45 min, cooled to room temperature, and spin coated again.

GF as dopant in the HTL: a 0.1 mg cm^{-3} GF dispersion in $CHCl_3$ was prepared, sonicated for 1 h in an ultrasonic bath at 37 kHz, and used in the preparation of the hole transport material solution by dissolving 46 mg of spiro-OMeTAD in 0.5 cm^3 of GF dispersion in $CHCl_3$, and adding 14.4 µL 4-*tert*-butylpyridine and 8.75 µL of a LiTFSI solution (520 mg cm^{-3}) in ACN. The solution was further sonicated for 1 h in an ultrasonic bath at 37 kHz, and spin-coated onto the substrates at 2000 rpm (2000 rpm s-1) for 30 s. The substrate was kept in a dry atmosphere in the dark overnight, and 60 nm of gold were thermally evaporated through a shadow mask to form the cathodes (SC_HTL).

4.2.4 Characterization of GF and the perovskite-based solar cells

Elemental analysis (C, N, H) were performed at “Unidade de Análisis Elemental – Universidade de Santiago de Compostela”

Transmission electron microscopy (TEM) images were collected at “Universidade de Trás-os-Montes e Alto Douro”, with a Zeiss LEO 906 microscope operating at an accelerating voltage of 120 kV. The material was dispersed in dimethylformamide under sonication, after which a carbon-coated 400 mesh copper grid was immersed in the suspension and then air-dried.

Textural characterization of material GF was carried out by N_2 adsorption–desorption at -196 ˚C in a Quantachrome NOVA 4200e apparatus. The apparent surface area (S_{BET}) was determined by applying the Brunauer–Emmett–Teller (BET) equation.[18]

X-ray diffraction (XRD) profile was collected at room temperature in a continuous scanning mode (step 0.02 and time 10 s) on a Rigaku D/Max-B, Cu K diffractometer in the 2θ range from 7˚ to 100˚, in a Bragg-Brentano $\theta/2\theta$ configuration. A Lorentzian deconvolution of the (002) peak observed in the GF XRD profile was performed and the crystallite sizes were estimated from the Scherrer equation [$L = 0.94 \times \lambda / (\beta_{1/2} \times \cos\theta)$], where L = average crystallite size, $\beta_{1/2}$ = line broadening at FWHM in radians, θ = Bragg angle and λ = X-ray wavelength (1.544 Å), and considering the interlayer distances. The area ratio was considered to measure the percentage of layers that are stacked as crystallites composed by the corresponding number of layers and although layers with interlayer spacing larger than 3.44 Å (2θ lower than 26.1º) are non 3-D stacked, they were considered only to estimate the weighted average number of layers in the materials and should not be regarded as crystallites.

Scanning electron microscopy (SEM) and energy-dispersive X-ray spectroscopy (EDS) studies were performed at “CEMUP – Centro de Materiais da Universidade do Porto”, using a high resolution environmental scanning electron microscope (FEI Quanta 400 FEG ESEM) equipped with an energy-dispersive X-ray spectrometer (EDAX Genesis X4M). The EDS maps were obtained after 32 accumulation cycles.

The performance of the solar cells was measured at “INL – International Iberian Nanotechnology Laboratory”, in a Newport PVIV test station, consisting of a class 3A solar simulator, a Keithley 2420 source meter and a NIST-calibrated reference cell. Current-voltage (*I*-*V*) plots were taken by applying voltage at a scan rate of 0.01 V s^{-1}, in 0.05 V steps, which corresponds to a 5 s delay time between each data point. When applicable, the cells were first measured in reverse bias (from 1 to 0 V) and afterwards in forward bias (from 0 to 1 V). All measurements were performed using calibrated AMG 1.5 reference spectrum throught a 0.0897 cm^2 shadow mask, and the solar cells

were illuminated at open circuit voltage during 3 s prior to each sweep. All I-V measurements were performed 24 h after gold evaporation, unless stated otherwise. The data obtained from the *I-V* plots was extracted with PVIV 2.0 software suite.

4.3 Results and discussion

4.3.1 Characterization of the graphene flakes (GF)

The morphology of the graphene flakes was analyzed by TEM and some examples of the obtained TEM micrographs are shown in Figure 4.1.

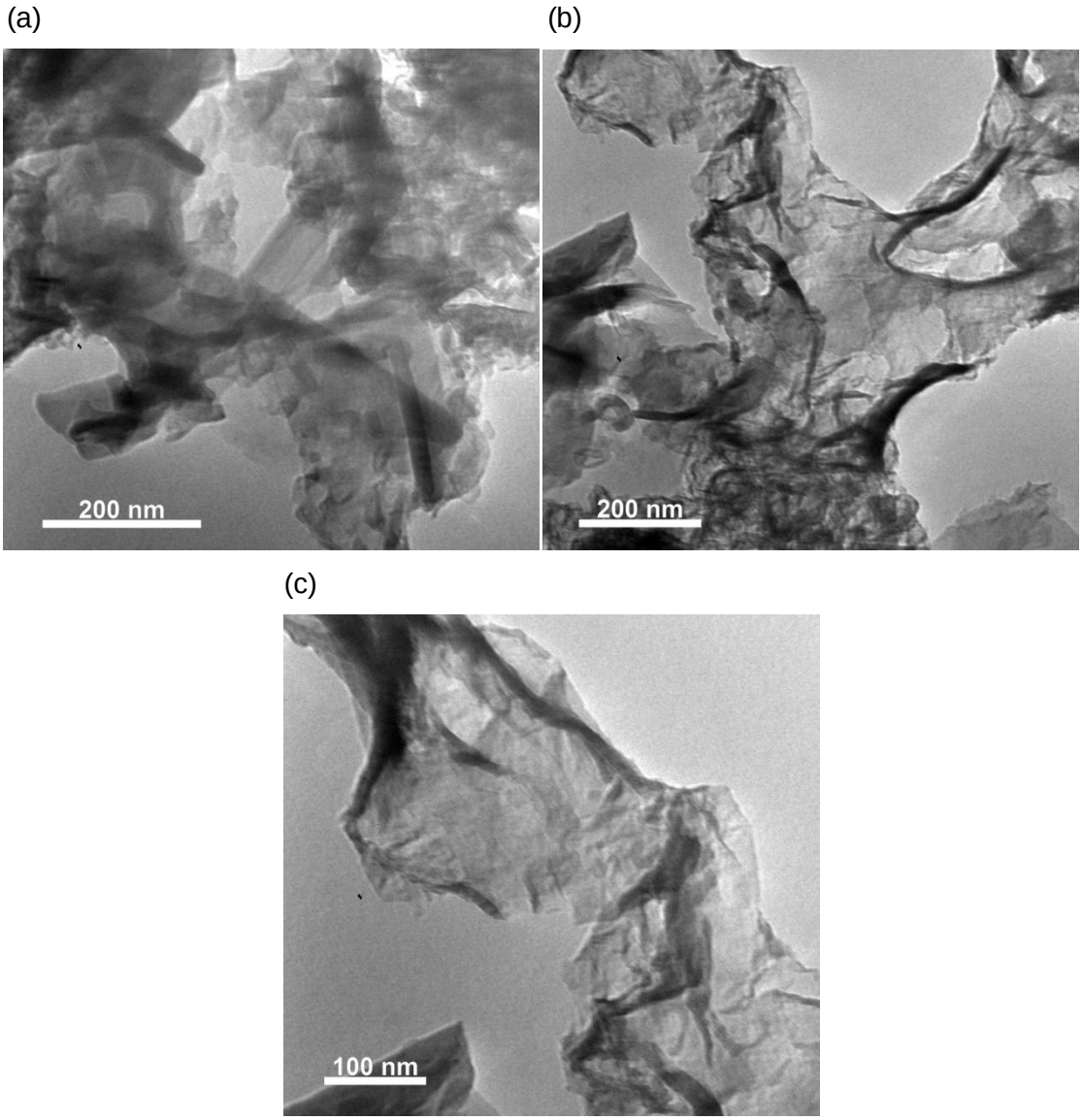

Figure 4.1 TEM micrographs of the commercial graphene flakes (GF).

The TEM images of GF (Figure 4.1) indicate that it is composed by wrinkled few-layer graphene sheets, whose sizes are in the range of hundreds of nanometres to one

micrometre. It is possible to observe large wrinkled few-layer graphene sheet domains coexisting with bundles of smaller crystallites.

The textural properties of the GF material were evaluated by the corresponding N_2 adsorption–desorption isotherm performed at -196 ˚C, shown in Figure 4.2.

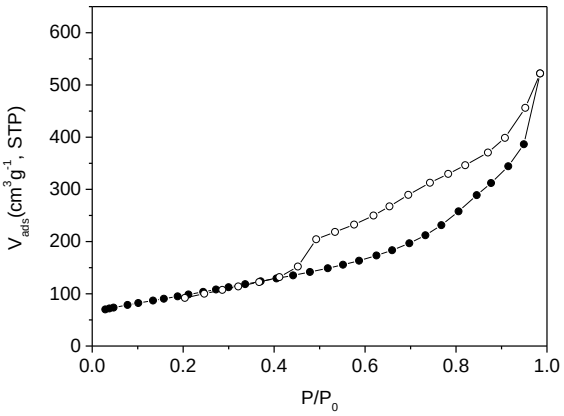

Figure 4.2 N_2 adsorption–desorption isotherm of GF at −196 ˚C (filled and unfilled symbols represent the adsorption and desorption processes, repectively).

The N_2 adsorption isotherm of GF is typically of type II, accordingly to IUPAC classification,[19] which is characteristic of non-porous materials and represents unrestricted monolayer-multilayer adsorption. A distinct hysteresis loop is observed, which is characteristic of non-rigid aggregates of plate-like particles. The calculated specific surface area obtained for GF was 352 m^2 g^{-1}. Taking into account the theoretical value of 2630 m^2 g^{-1} calculated for single layer graphene,[20] it is possible to estimate an average number of layers per crystallite of 7.

In order to gain further insights into the structure of the graphene flakes, they were studied by X-ray diffraction (XRD). The XRD diffractogram of GF, shown in Figure 4.3 presents peaks at 2θ angle 26.1˚ and 43.1˚, corresponding to (002) and (101) planes of graphitic framework, respectively.[21,22]

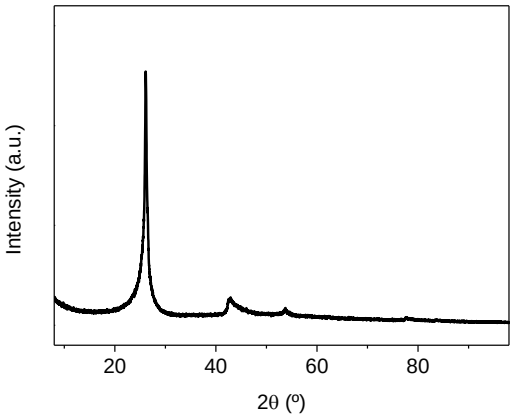

Figure 4.3 XRD diffractogram of GF.

The first peak is related to the periodicity between the graphene layers and the second within the graphene layer (honeycomb lattice at a single graphene sheet).[23] Due to the strong asymmetry observed in the (002) peak, a Lorentzian deconvolution of the signal was performed, shown in Figure 4.4, and the deconvolution data is summarized in Table 4.1. The Bragg's equation was applied to the components of the deconvolution of the (002) peak in order to obtain the distance between graphene layers, for each crystallite type, which have different interlayer distances and a different number of graphene layers. The Scherrer's equation with a constant of 0.94 was applied to evaluate the crystallite size and number of layers per crystallite.[24]

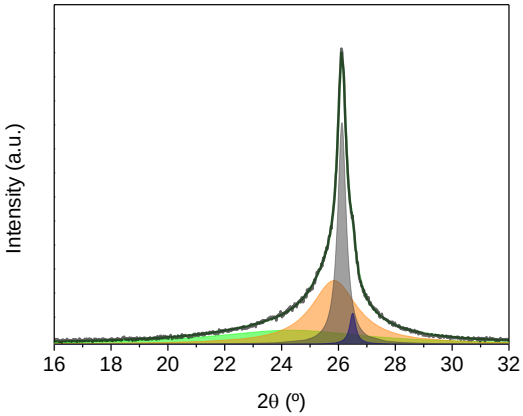

Figure 4.4 Deconvolution of the XRD (002) peak for GF.

Table 4.1 XRD data for GF obtained from the deconvolution of the 002 peak.

Material	2θ / ˚	Interlayer distance / Å	Average no. layers	Peak area ratio / %	Weighted average no. layers[a]
GF	24.3	3.67	5	29.6	10
	25.8	3.46	14	41.2	
	26.1	3.42	70	26.5	
	26.5	3.37	99	2.7	

[a]Assuming that the areas of the XRD peaks are proportional to the no. of layers (which are stacked in different numbers to form crystallites of different sizes), the weighted average number of layers may be roughly estimated as follow: if one consider that 2.7 % of the layers are stacked as 1 crystallite of 99 layers, then the total number of layers is 3678; there will be 14 crystallites of 70 layers, 111 of 14 layers and 237 of 5 layers, which totals 363 crystallites. Thus, the average number of layers will be 3678/363 = 10 layers per crystallite.

Taking into account the peak area ratios of the different peak components, it was possible to estimate a weighted average number of layers of 10, which is in reasonable agreement with the S_{BET} analysis, which allowed an estimation of 7 layers per crystallite. It is also noteworthy that despite the existence of larger crystallites, roughly

70% of the layers are not 3-D stacked since they show interlayer spacings larger than 3.44 Å.

4.3.2 Characterization of the pristine perovskite-based solar cells

Mesoscopic mixed halide perosvkite based solar cells were prepared as described earlier, and their structure is shown in Figure 4.5.

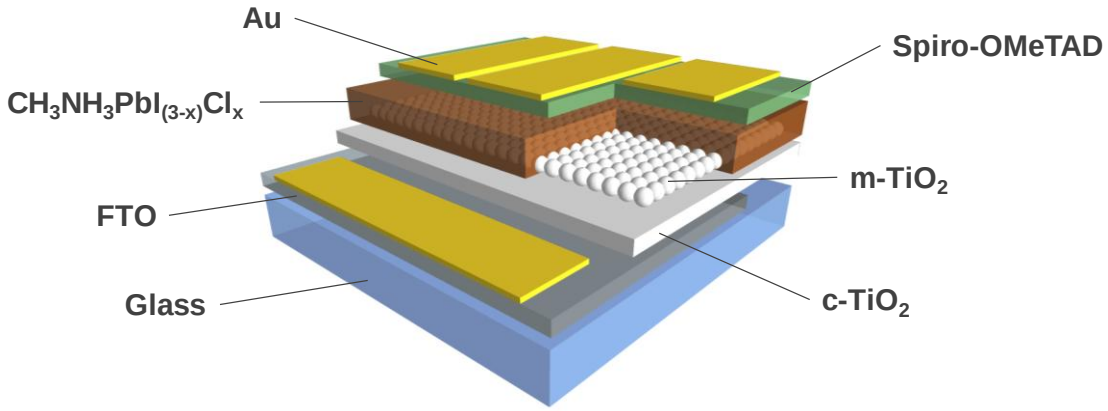

Figure 4.5 Scheme of the prepared mesoscopic mixed halide perovskite solar cells.

The prepared devices were composed by a double compact layer of TiO_2 (c-TiO_2) formed on top of a fluoride tin oxide (FTO) coated glass, to prevent direct contact between the perovskite layer and the FTO. A mesoscopic layer of TiO_2 (m-TiO_2) was deposited on top of c-TiO_2, and the $CH_3NH_3PbI_{(3-x)}Cl_x$ crystals were formed on top of the mesoporous layer, filling the pores and creating an overlayer. The HTL was deposited on top of the perovskite layer, followed by gold deposition to form the cathodes.

Figure 4.6 shows the SEM image of the pristine solar cell SC_P2 cross-section, and Figure 4.7 depicts the corresponding EDS maps.

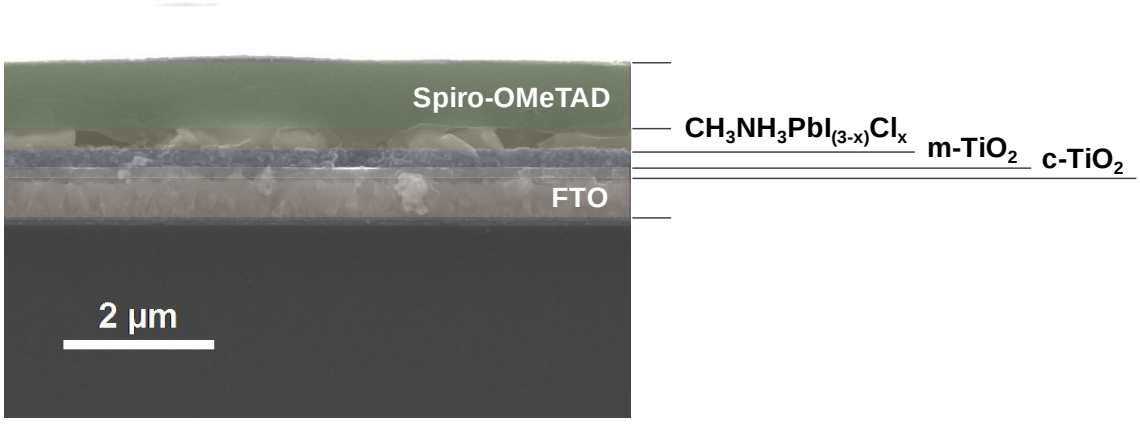

Figure 4.6 SEM micrograph of solar cell SC_P2 (cross-section).

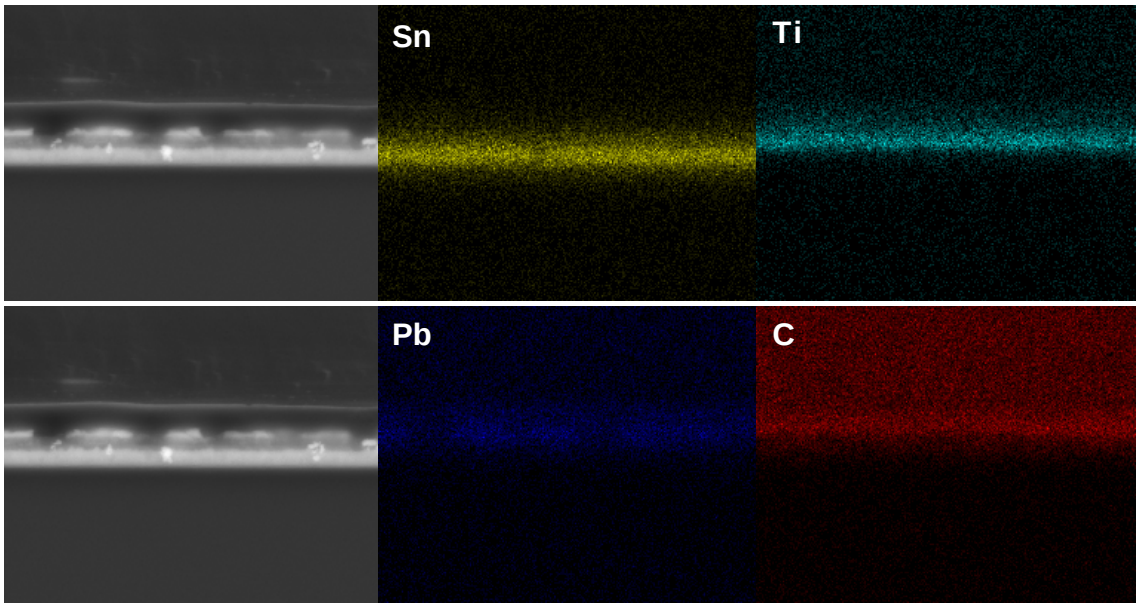

Figure 4.7 EDS maps of solar cell SC_P2 (cross-section).

From Figures 4.6 and 4.7, it is possible to confirm the undoped perovskite solar cells structure, having a ~150 nm thick TiO_2 compact layer, with a mesoporous TiO_2 layer measuring ~260 nm in cross-section. The mixed halide perovskite layer had an overlayer ~330 nm thick, and the HTL had a thickness of 900 nm. Detailed measurements are shown in Appendix B.

The *I-V* plots obtained for the prepared solar cells are shown in Figure 4.8 and the calculated performance data is presented in Table 4.2.

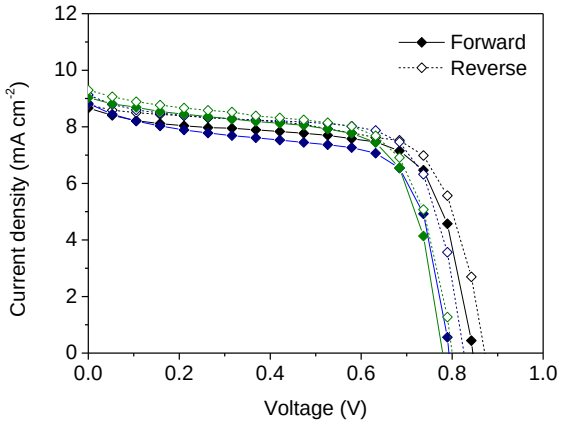

Figure 4.8 I-V plots for the pristine solar cells SC_P1 (black), SC_P2 (blue), and SC_P3 (green).

Table 4.2 Performance data obtained from the *I-V* plots for the pristine solar cells.

Device	Scan bias	V_{oc} (V)	I_{sc} (mA cm^{-2})	FF	R at V_{oc} (Ω)	R at I_{sc} (Ω)	PCE (%)
SC_P1	Forward	0.84	8.59	0.67	84	3807	4.90
	Reverse	0.87	8.73	0.68	122	6227	5.21
SC_P2	Forward	0.79	8.77	0.65	65	2230	4.50
	Reverse	0.83	8.89	0.70	114	4529	5.11
SC_P3	Forward	0.78	8.99	0.67	114	4072	4.70
	Reverse	0.80	9.25	0.66	93	3755	4.86
Average		0.82	8.87	0.67	99	4103	4.88
SD		0.04	0.23	0.02	22	1297	0.26

It possible to observe in Figure 4.8 that the prepared solar cells presented similar *I-V* profiles, indicating that the preparation method was effective in the fabrication of stable and reproducible devices. The hysteresis observed for all devices was acceptable for this type of mesoscopic solar cells, indicating that the conditions used in the *I-V* measurements were appropriate, as the delay time, and light and voltage bias conditions prior to measurement can all have a significant impact upon the shape of the measured *I-V* light curves and the apparent power-to-current efficiency (PCE).[25] Nevertheless, the average of the forward and reverse scans of all devices will be considered. From Table 4.2, it is possible to observe that the pristine solar cells have a V_{oc} of 0.82 V, which is characteristic of $CH_3NH_3PbI_{(3-x)}Cl_x$ perovskite based devices,[26] a current density I_{sc} of 8.87 mA cm^{-2}, and a fill factor of 0.67, yielding an average 4.88 % PCE.

4.3.3 Characterization of the doped perovskite-based solar cells

In an effort to study the effects of doping of the ETL with graphene, perovskite based solar cells with GF as dopants in the ETL, were prepared through method A, dispersing the graphene flakes in the mesoporous TiO_2 precursor, according to the scheme shown in Figure 4.9.

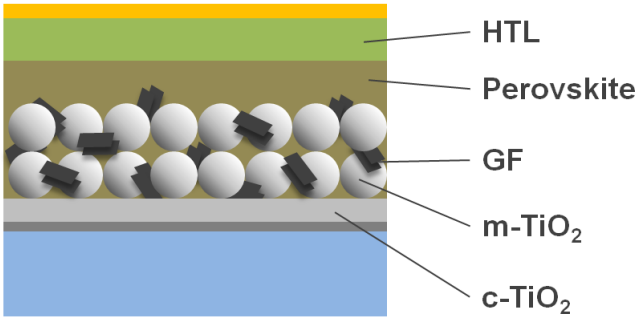

Figure 4.9 Structure of the solar cells doped with GF in the ETL, prepared through method A.

In order to study the distribution of GF within the TiO_2 mesoporous layer of the devices doped in the ETL through method A, two samples were prepared with identical conditions of those of devices SC_A0.1 and SC_A2.0, but without perovskite and the following layers, and analyzed through SEM-EDS. Figure 4.10 and 4.11 shows the SEM image and EDS maps for SC_A0.1 and SC_A2.0, respectively.

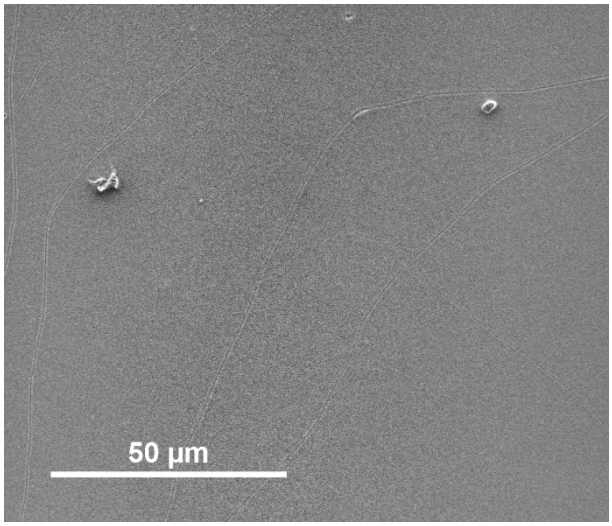

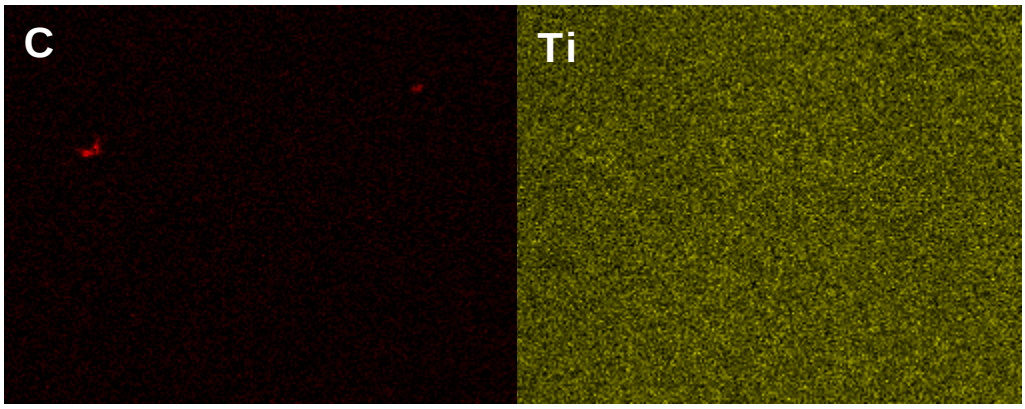

Figure 4.9 SEM micrograph and correspondent EDS maps for SC_A0.1.

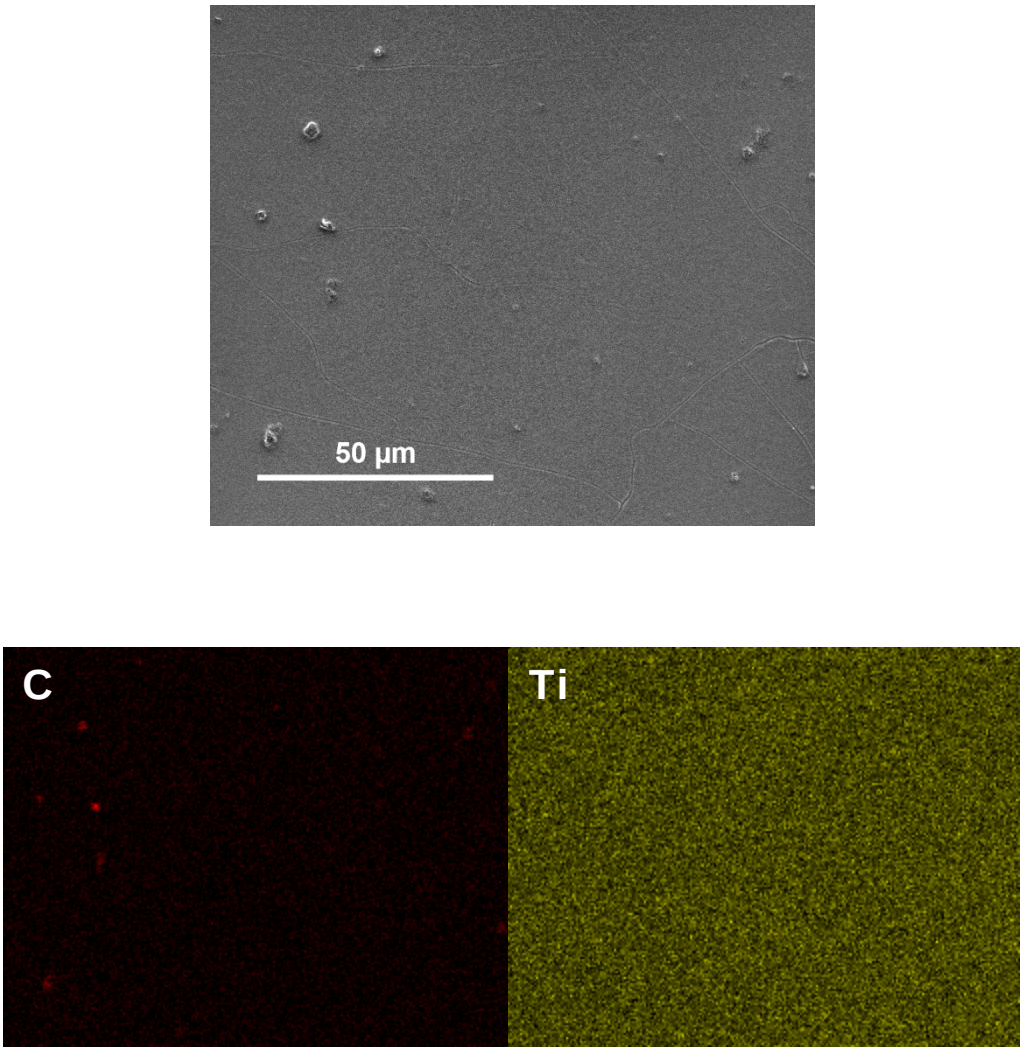

Figure 4.10 SEM micrograph and correspondent EDS maps for SC_A2.0.

It can be seen from Figure 4.9 and 4.10, the existence of graphene flake agglomerates at the surface of the mesoporous TiO_2, partially or completely covered with TiO_2 nanoparticles, with sizes up to several micrometers. Substrate SC_A2.0 presented a greater number of these carbon clusters, than substrate SC_A0.1, as expected. Furthermore, the size of the agglomerates shows that the used sonication procedure was not effective in the fabrication of a good GF dispersion.

The *I-V* plots obtained for the solar cells with GF as dopant in the ETL, prepared through method A, are shown in Figure 4.11 and the performance data is presented in Table 4.3.

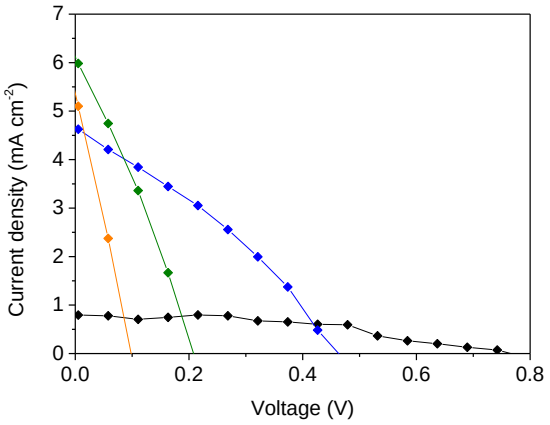

Figure 4.11 I-V plots for the ETL doped solar cells through method A: SC_A0.1 (black), SC_A0.5 (blue), SC_A1.0 (green), and SC_A2.0 (orange).

Table 4.3 Performance data obtained from the *I-V* plots for the solar cells doped with GF in the ETL through method A.

Device	Scan bias	V_{oc} (V)	I_{sc} (mA cm^{-2})	FF	R at V_{oc} (Ω)	R at I_{sc} (Ω)	PCE (%)
SC_A0.1	Reverse	0.77	0.62	0.59	3702	14717	0.28
SC_A0.5	Reverse	0.46	4.67	0.32	852	1378	0.69
SC_A1.0	Reverse	0.21	6.13	0.29	300	10	0.37
SC_A2.0	Reverse	0.10	5.37	0.26	189	11	0.14

From Figure 4.11 and Table 4.3 it is possible to verify that the doping of the ETL through method A severely affected the solar cells performance, resulting in devices with efficiencies below 1 %. A large decrease was observed in all three parameters that characterize the *I-V* profiles, V_{oc}, I_{sc}, and fill factor, when compared to the pristine devices. We attribute this result to extensive exciton quenching promoted by the incorporated GF within the mesoporous TiO_2 layer. In fact, with the increase of GF content in the ETL, from SC_A0.1 to SC_A2.0, it is possible to observe a decrease in V_{oc}, and a decrease in R at I_{sc}, which is proportional to R_{SH}, thus indicating the large decrease in the shunt resistance promoted by the introduction of a large amount of localized shunts. These introduced shunts may be due the large agglomerates of GF, and/or to the high number of layers of the GF crystallites, as confirmed by TEM, N_2 adsorption-desorption, and XRD.

The structure of the solar cells prepared doped with GF in the ETL, prepared through method B, is shown schematically in Figure 4.13. With this approach, we attempted to settle the graphene flakes on top of the TiO_2 nanoparticles, whilst keeping most of their surface available for contact with the subsequent perovskite layer.

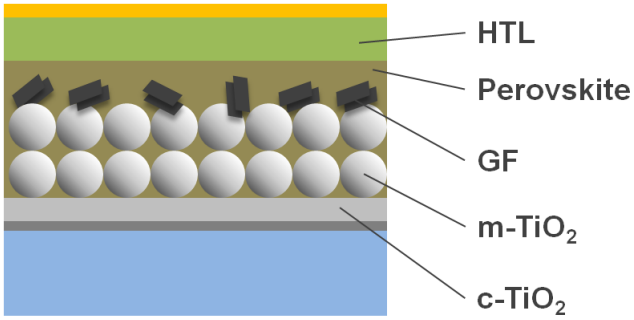

Figure 4.13 Structure of the solar cells doped with GF in the ETL, prepared through method B.

To assess the distribution of GF in the TiO_2 mesoporous layer of the devices doped in the ETL through method B, two substrates were prepared with equal conditions of those of devices SC_B1 and SC_B4, but without perovskite and the following layers, and analyzed through SEM-EDS. Figure 4.14 and 4.15 shows the SEM micrograph and EDS maps for SC_B1 and SC_B4, respectively.

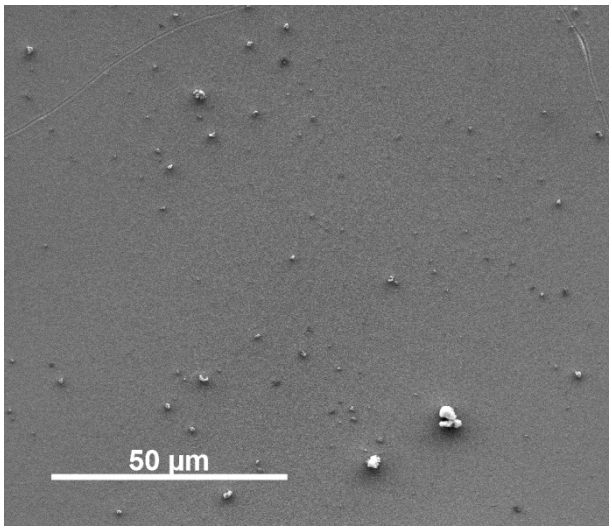

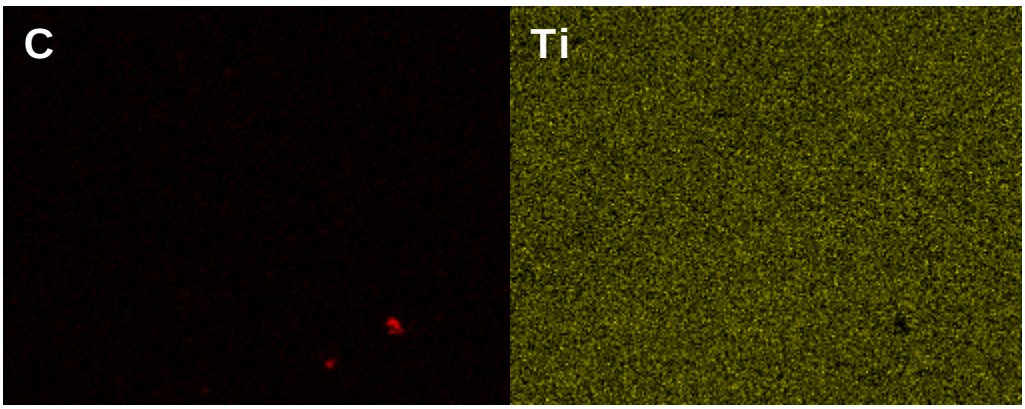

Figure 4.14 SEM micrograph and correspondent EDS maps for SC_B1.

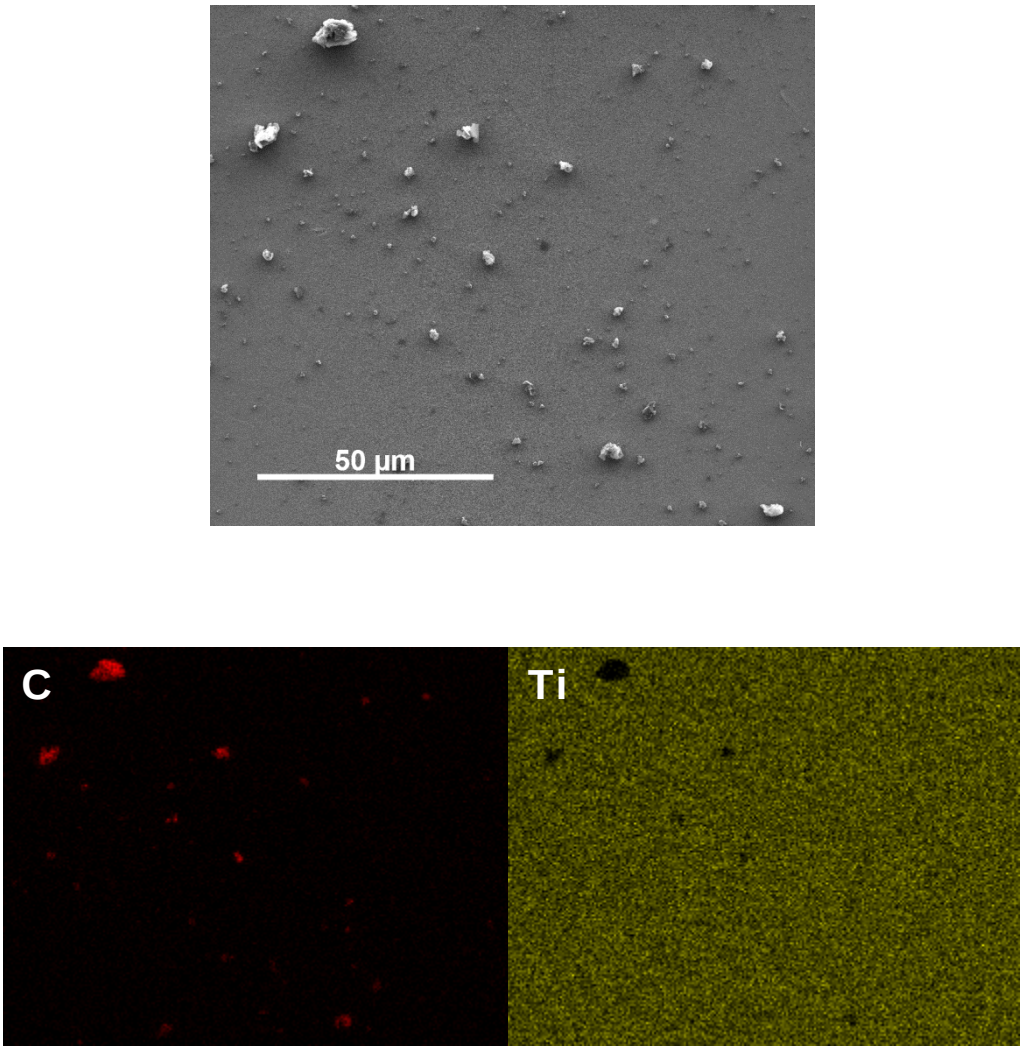

Figure 4.15 SEM micrograph and correspondent EDS maps for SC_B4.

It can be seen from Figure 4.14 and 4.15, the existence of graphene flake agglomerates with sizes up to several micrometers, settled at the surface of the mesoporous TiO_2. It is also possible to observe that these bundles of GF are exposed, as expected. Substrate SC_B4 presents a higher amount of GF bundles than substrate SC_B1, indicating that GF content increased with the number of consecutive spin coating procedures.

The *I-V* plots obtained for the solar cells with GF as dopant in the ETL, prepared through method B, are shown in Figure 4.16 and the performance data is presented in Table 4.4.

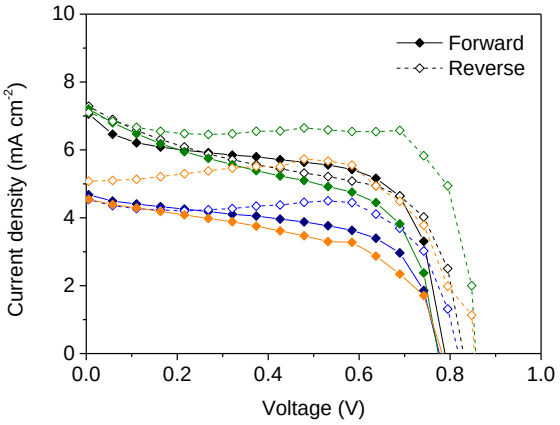

Figure 4.15 I-V plots for the ETL doped solar cells through method B: SC_B1 (black), SC_B2 (blue), SC_B3 (green), and SC_B4 (orange).

Table 4.4 Performance data obtained from the *I-V* plots for the solar cells doped with GF in the ETL through method B.

Device	Scan bias	V_{oc} (V)	I_{sc} (mA cm^{-2})	FF	*R* at V_{oc} (Ω)	*R* at I_{sc} (Ω)	PCE (%)
SC_B1	Forward	0.79	7.06	0.59	157	730	3.29
	Reverse	0.83	7.31	0.53	154	1649	3.20
SC_B2	Forward	0.78	4.66	0.60	205	5161	2.17
	Reverse	0.82	4.40	0.73	200	11467	2.62
SC_B3	Forward	0.77	7.23	0.51	149	1609	2.84
	Reverse	0.86	6.95	0.76	50	4873	4.53
SC_B4	Forward	0.78	4.55	0.54	264	4677	1.93
	Reverse	0.85	5.15	0.74	59	6336025	3.24

From Table 4.4, it is clear that the doping procedure resulted in an overall inferior PCE, when compared to the pristine devices, with averaged efficiencies of 3.24, 2.39, 3.68, and 2.58 % for devices SC_B1, SC_B2, SC_B3, and SC_B4, respectively. It is also noteworthy that the obtained efficiencies do not present a direct relation with the doping amount, although more assays would be required to assess this particular aspect. In Figure 4.15 it is possible to observe a very distinct feature of the doped devices *I-V* profiles, which is the occurrence of hysteresis between the forward and reverse scans. Moreover, the hysteresis intensity increases gradually from SC_B1 to SC_B4, indicating that it increases with the amount of GF introduced on top of the mesoporous TiO_2 layer. Hysteretic effects in *I-V* measurements have been observed in this type of mesoscopic devices and have been speculated to originate from trapping/de-trapping of charge carriers, changes in absorber or contact conductivity, ferroelectricity and ion migration.[25,27,28]

Moreover, contacts can influence the size and direction of the transient effects and hysteresis. In this context, the presence of GF in the doped devices at the perovskite/TiO_2 interface is consistent with a mechanism where transient polarization of the perovskite absorber results in changes in charge carrier extraction efficiency at the carrier-selective contact, which is consistent with the observed hysteresis in the *I-V* plots. Nevertheless, the presence of GF at the perovskite/TiO_2 interface resulted in poorer device performances.

In order to study the potential enhancement of the hole transport mechanism introduced by GF doping, a solar cell was prepared with GF in the HTL, and its structure is shown schematically in Figure 4.17.

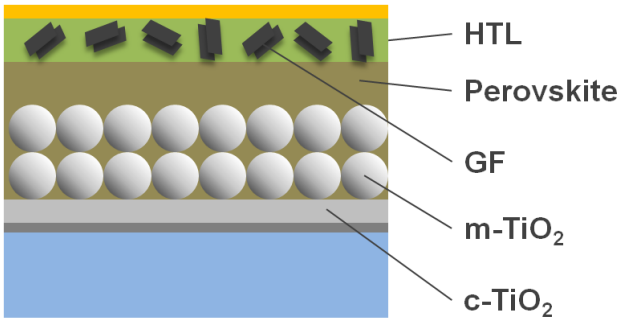

Figure 4.17 Structure of the solar cell doped with GF in the HTL (SC_HTL).

The morphology of the HTL layer doped with GF was assess by SEM observations. A substrate was prepared with equal conditions to device SC_HTL, but without Au, and analyzed through SEM. Figure 4.18 shows the SEM micrograph for SC_HTL.

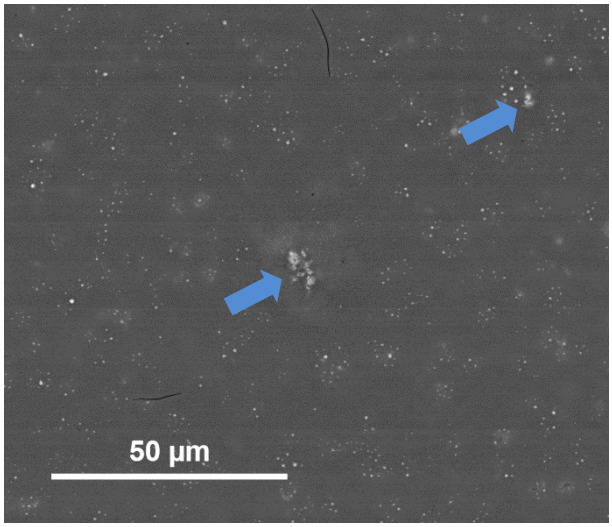

Figure 4.18 SEM micrograph for SC_HTL.

In Figure 4.17 it is possible to observe a relatively uniform surface with small bubble-like structures, resultant from the deposition procedure. No large agglomerates of GF were found at the surface, as in the ETL doped substrates, instead, small protrusions of GF are observed (marked with blue arrows) emerging at the HTL surface, showing that the graphene flakes were almost completely surrounded by the HTL after the spin coating deposition.

The *I-V* plot obtained for the solar cell with GF as dopant in the HTL is shown in Figure 4.19 and the performance data is presented in Table 4.5.

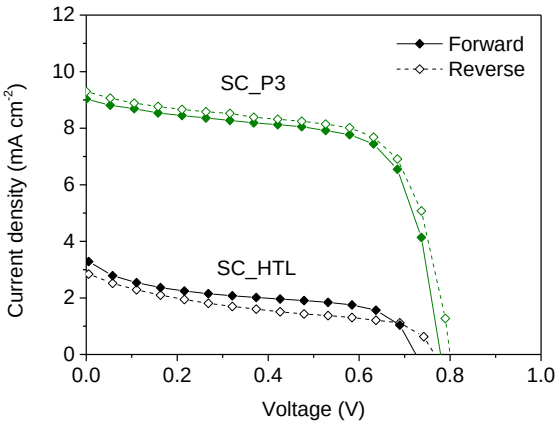

Figure 4.19 I-V plots for the pristine solar cell SC_P3 and HTL doped solar cell SC_HTL.

Table 4.5 Performance data obtained from the *I-V* plots for the solar cells doped with GF in the HTL.

Device	Scan bias	V_{oc} (V)	I_{sc} (mA cm^{-2})	FF	R at V_{oc} (Ω)	R at I_{sc} (Ω)	PCE (%)
SC_HTL	Forward	0.72	3.38	0.42	381	769	1.02
	Reverse	0.77	2.89	0.35	422	1189	0.77

As can be seen in Figure 4.18 and Table 4.5, the device doped with GF in the HTL showed a strongly decreased PCE, when compared to the undoped devices, presenting an averaged efficiency of 0.89 %. Although this decrease has contribution from the decrease of all three parameters listed in Table 4.5, V_{oc}, I_{SC}, and fill factor, the *I-V* profile is similar in shape to those the pristine devices (the *I-V* plot of SC_P3 is shown in Figure 4.18 for comparison), indicating that the lower performance is mainly due to an increase in series resistance. Spiro-OMeTAD present in the HTL is known to have an certain ratio of spiro-OMeTAD^{+}/ spiro-OMeTAD for optimized hole transport, and hence the addition of the LiTFSI and t-BP additives, which promote its oxidation.[29] We speculate that the presence of GF in the HTL promotes an overextension of the oxidation of spiro-OMeTAD, resulting in poorer hole transport hability, which is in agreement with the general trend previously reported that affirms that low

concentrations of spiro-OMeTAD$^+$ are beneficial for the device functioning, whereas higher concentrations leads to abrupt photocurrent drops, accompanied with a strong loss of efficiency.[27]

4.3.4 Stability of the perovskite-based solar cells

Stability studies regarding the effect of aging on the medium term performance of the pristine solar cells were performed by storing the prepared devices, without encapsulation, in 500 cm^3 hermetic container with 250 g silica gel inside, and in the dark, for 100 days. Figure 4.20 shows the evolution of the *I-V* plots for devices SC_P1, SC_P2, and SC_P3.

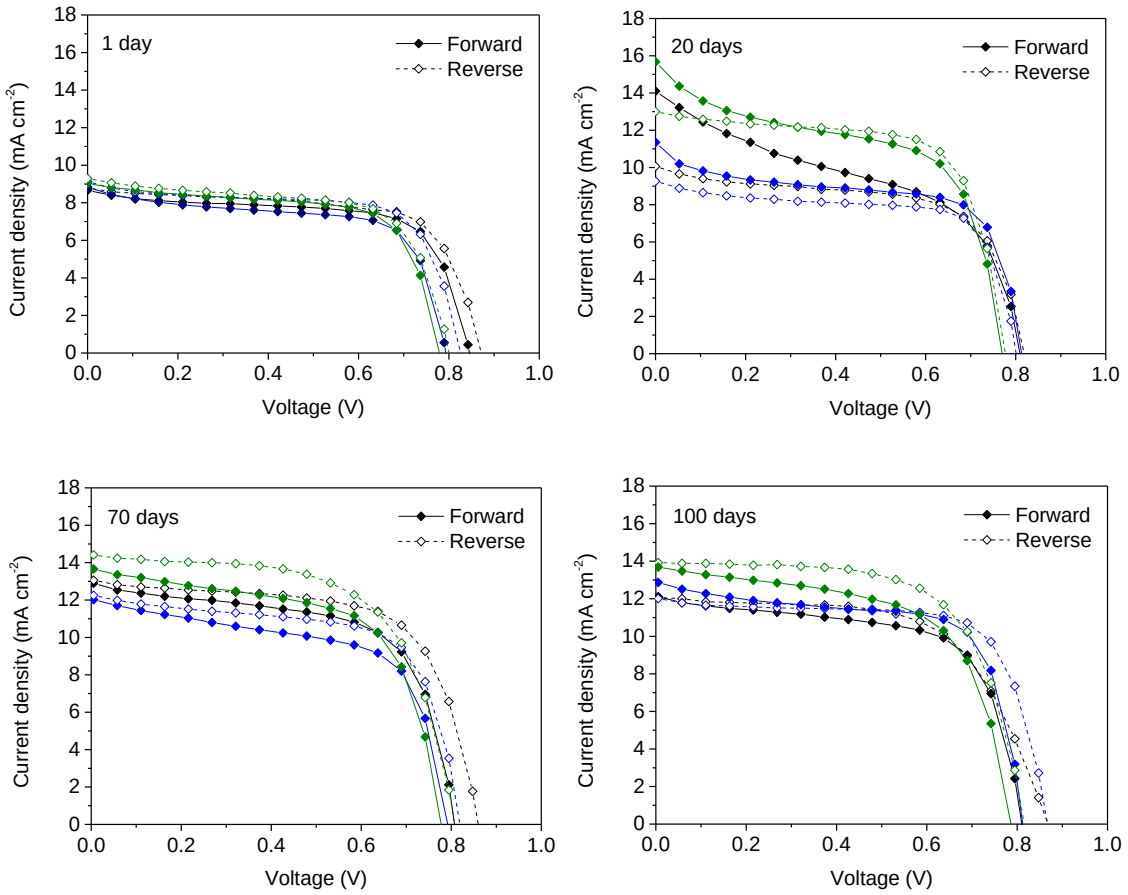

Figure 4.19 *I-V* plotsof the pristine solar cells SC_P1 (black), SC_P2 (blue), and SC_P3 (green), exposed to desiccant during 1, 20, 70, and 100 days.

It can be seen in Figure 4.20 that there is an increase in the overall solar cells performance upon storage with desiccant, mainly due to an increase in I_{sc}. It is also possible to observe significant changes in the *I-V* plots shape after 20 and 70 days, and to a lesser extent, after 100 days, suggesting the occurrence of structural changes in the $CH_3NH_3PbI_{(3-x)}Cl_x$ layer and/or in the HTL. Figure 4.21 shows the evolution of the PCE with desiccant exposure time, and Table 4.6 summarizes the data obtained from

the *I-V* plots, averaged for the forward and reverse sweeps of the 3 studied devices. The detailed data obtained for each device is shown in Appendix B.

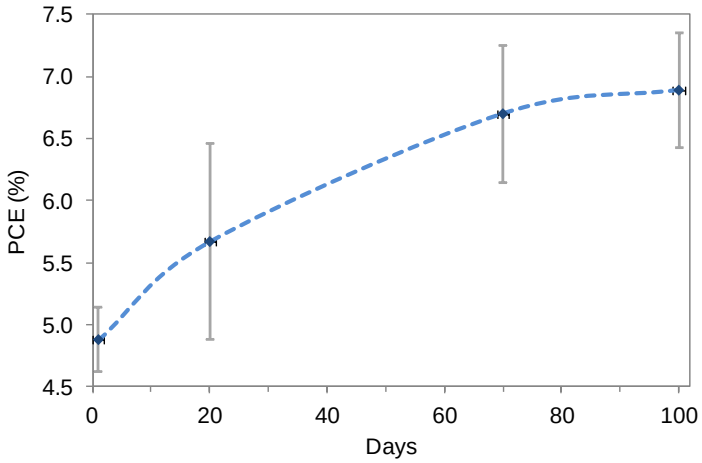

Figure 4.21 Evolution of PCE of the pristine solar cells with desiccant exposure (the error bars correspond to the standard deviation of the forward and reverse scans of the three pristine devices).

Table 4.6 Averaged performance data obtained from the *I-V* plots for the pristine solar cells after desiccant exposure..

Days	V_{oc} (V)	I_{sc} (mA cm^{-2})	FF	R at V_{oc} (Ω)	R at I_{sc} (Ω)	PCE (%)
1	0.82	8.87	0.67	99	4103	4.88 (±0.26)
20	0.80	11.87	0.61	76	2234	5.67 (±0.79)
70	0.81	13.11	0.63	81	2894	6.70 (±0.55)
100	0.83	12.82	0.65	92	4225	6.89 (±0.46)

From Figure 4.20 and Table 4.6, it is possible to observe and increase from 4.88 to 6.89 % PCE in the pristine solar cells, after 100 days of desiccant exposure, which is roughly a 40 % increase in efficiency. We attribute these results to the presence of desiccant, which absorbs residual solvent molecules, enhancing the aging of the spiro-OMeTAD layer, and the further crystallization of the perovskite layer.[30] However, further studies of aging without the presence of desiccant are required to assure these statements. Nevertheless, these results indicate that the storage of the freshly prepared mesoscopic devices in a dry atmosphere and in the dark, for at least 100 days, greatly improves their PCE.

4.4 Conclusions

Mesoscopic mixed halide perosvkite based solar cells were successfully prepared, yielding stable and reproducible pristine devices with an average 4.88 % PCE. The *I-V* measurements were found to be appropriate, as they can all have a

significant impact upon the apparent power-to-current efficiency (PCE), and were used as a benchmark for the doped devices.

Doped solar cells were prepared with GF in the ETL through the integration of graphene flakes in the mesoporous TiO_2 layer (method A), and TEM images showed large graphene flake agglomerates at the surface of the mesoporous layer, partially or completely covered with TiO_2 nanoparticles. The doping of the ETL through method A severely affected the solar cells performance, resulting in devices with efficiencies below 1 %. This result is attributed to extensive exciton quenching promoted by GF within the mesoporous TiO_2 layer, as indicated by the large decrease in the shunt resistance, which accompanies the increase in GF amount, promoted by the large agglomerates of GF, and/or to the high number of layers of the GF crystallites, as confirmed by TEM, N_2 adsorption-desorption, and XRD.

Solar cells doped with GF in the ETL, specifically in the perovskite/TiO_2 interface were prepared (method B), and TEM images revealed the existence of several micrometers sized graphene flake agglomerates, settled at the surface of the mesoporous TiO_2. The doping procedure resulted in an overall inferior PCE, with averaged efficiencies of 3.24, 2.39, 3.68, and 3.55 % for devices SC_B1, SC_B2, SC_B3, and SC_B4, respectively. The occurrence of hysteresis in the *I-V* plots of the doped devices was observed, and its intensity increases with the amount of GF doping. The presence of hysteresis is due to changes in charge carrier extraction efficiency at the carrier-selective contact, introduced by GF doping.

A device with HTL doped with GF was prepared and showed a relatively uniform surface with small protrusions of GF, showing that the graphene flakes were almost completely surrounded by the HTL. The doped device showed a strongly decreased PCE, with an efficiency of 0.89 %. This decrease was attributed to the overextension of the oxidized state of spiro-OMeTAD caused by the presence of GF, leading to a detrimental effect on its hole transport ability and subsequent loss of the device efficiency.

Stability studies of the pristine solar cells were carried out, regarding the aging of the devices in a dry and dark environment, during 100 days. An increase from 4.88 to 6.89 % PCE was observed after 100 days of desiccant exposure in the dark, which may be due to the absorption of residual solvent molecules, enhancing the settling of the spiro-OMeTAD layer, and crystallization of the perovskite layer.

4.5 References

[1] R. F. Service, *Science* **2005**, *309*, 548–551.

[2] L. M. Gonçalves, V. Z. Bermudez, H. A. Ribeiro, A. M. Mendes, *Energy Environ. Sci.* **2008**, *1*, 655–667.

[3] L. Wang, H. Liu, R. M. Konik, J. A. Misewich, S. S. Wong, *Chem. Soc. Rev.* **2013**, *42*, 8134–8156.

[4] A. Kojima, K. Teshima, Y. Shirai, T. Miyasaka, *J. Am. Chem. Soc.* **2009**, *131*, 6050–6051.

[5] Y. Zhou, K. Zhu, *ACS Energy Lett.* **2016**, *1*, 64–67.

[6] K. S. Novoselov, A. K. Geim, S. V. Morozov, D. Jiang, Y. Zhang, S. V. Dubonos, I. V. Grigorieva, A. A. Firsov, *Science* **2004**, *306*, 666–669.

[7] Y. Zhang, Y. Tan, H. L. Stormer, P. Kim, *Nature* **2005**, *438*, 201–204.

[8] K. S. Novoselov, Z. Jiang, Y. Zhang, S. V Morozov, H. L. Stormer, U. Zeitler, J. C. Maan, G. S. Boebinger, P. Kim, A. K. Geim, *Science* **2007**, *315*, 1379.

[9] A. A. Balandin, S. Ghosh, W. Bao, I. Calizo, D. Teweldebrhan, F. Miao, C. N. Lau, *Nano Lett.* **2008**, *8*, 902–907.

[10] J. S. Bunch, S. S. Verbridge, J. S. Alden, A. M. Van Der Zande, J. M. Parpia, H. G. Craighead, P. L. Mceuen, *Nano Lett.* **2008**, *8*, 2458–2462.

[11] C. Lee, X. Wei, J. W. Kysar, J. Hone, *Science* **2008**, *321*, 385–388.

[12] R. D. Costa, F. Lodermeyer, R. Casillas, D. M. Guldi, *Energy Environ. Sci.* **2014**, *7*, 1281–1296.

[13] Z. Yin, J. Zhu, Q. He, X. Cao, C. Tan, H. Chen, *Adv. Energy Mater.* **2014**, *4*, 1300574.

[14] D. W. Chang, H.-J. Choi, A. Filer, J.-B. Baek, *J. Mater. Chem. A* **2014**, *2*, 12136–12149.

[15] Z. Zhu, J. Ma, Z. Wang, C. Mu, Z. Fan, L. Du, Y. Bai, L. Fan, H. Yan, D. L. Phillips, et al., *J. Am. Chem. Soc.* **2014**, *136*, 3760–3763.

[16] Q. Luo, Y. Zhang, C. Liu, J. Li, H. Lin, *J. Mater. Chem. A* **2015**, *3*, 15996–16004.

[17] W. Li, H. Dong, X. Guo, N. Li, J. Li, G. Niu, *J. Mater. Chem. A* **2014**, *2*, 20105–20111.

[18] S. Brunauer, P. H. Emmett, E. Teller, *J. Am. Chem. Soc.* **1938**, *60*, 309–319.

[19] M. Thommes, K. Kaneko, A. V Neimark, J. P. Olivier, F. Rodriguez-reinoso, J. Rouquerol, K. S. W. Sing, *Pure Appl. Chem.* **2015**, *87*, 1051–1069.

[20] S. Park, R. S. Ruoff, *Nat. Nanotechnol.* **2009**, *4*, 217–224.

[21] A. B. Fuertes, S. Alvarez, *Carbon* **2004**, *42*, 3049–3055.

[22] T. Kim, I. Park, R. Ryoo, *Angew. Chemie - Int. Ed.* **2003**, *42*, 4375–4379.

[23] D. Reznik, C. H. Olk, D. A. Neumann, J. R. D. Copley, *Phys. Rev. B* **1995**, *52*, 116–124.

[24] B. K. Saikia, R. K. Boruah, P. K. Gogoi, *J. Chem. Sci.* **2009**, *121*, 103–106.

[25] E. L. Unger, E. T. Hoke, C. D. Bailie, W. H. Nguyen, A. R. Bowring, M. G. Christoforo, M. D. Mcgehee, *Energy Environ. Sci.* **2014**, *7*, 3690–3698.

[26] T. Ng, C. Chan, M. Lo, Q. Guan, C. Lee, *J. Mater. Chem. A* **2015**, *3*, 9081–9085.

[27] A. Dualeh, T. Moehl, N. Tétreault, J. Teuscher, P. Gao, M. Nazeeruddin, M. Grätzel, *ACS Nano* **2014**, *8*, 362–373.

[28] R. S. Sanchez, V. Gonzalez-Pedro, J. W. Lee, N. G. Park, Y. S. Kang, I. Mora-Sero, J. Bisquert, *J. Phys. Chem. Lett.* **2014**, *5*, 2357–2363.

[29] R. S. Sanchez, E. Mas-Marza, *Sol. Energ. Mat. Sol. Cells* **2016**, *158*, 189–194.

[30] A. E. Williams, P. J. Holliman, M. J. Carnie, M. L. Davies, D. A. Worsley, T. M. Watson, *J. Mater. Chem. A* **2014**, *2*, 19338–19346.

Chapter 5

Final conclusions and future perspectives

5

Final conclusions and future perspectives

The final chapter of the thesis provides a general overview of the main conclusions and summarizes the most relevant achievements. Moreover, new perspectives for future work are proposed.

5.1 Conclusions

Regarding the modification of MWCNTs and GF, the results obtained in Chapter 2 showed the successful modification of the carbon materials through three different oxidation procedures, namely nitric acid treatment, nitric acid followed by thermal treatment, and gas phase oxidation with O_2. The materials characterization through XPS, TPD, and FTIR showed an overall increase in the materials oxygen content upon the different oxidation procedures and revealed that they induced different superficial chemical compositions, namely: (i) nitric acid treated materials MWCNTh and GFh, presented increased amounts of carboxylic acids, anhydrides and phenols; (ii) nitric acid followed by thermal treatment at 400 ˚C induced the removal of carboxylic acids and an in crease in anhydrides content; (iii) gas phase oxidation promoted the introduction of phenols, carbonyls/quinones, and lactones. Textural characterization revealed that the oxidation procedures promoted an increase in the carbon nanotube materials specific surface area, through the increase in the inner cavities access, while the graphene flake materials present lower surface areas upon the oxidation procedures, indicating a higher degree of agglomeration, which was confirmed through XRD analysis. Raman spectroscopy revealed that the oxidation procedures promoted an overall increase in the materials disorder through the introduction of defects onto their original structure.

The catalytic studies showed that all the materials were active catalysts in the selective oxidation of *cis*-cyclooctene and that the modifications introduced in the carbon nanotubes and graphene flakes, through nitric acid followed by thermal treatment at 400 ˚C, originated catalysts with superior activity and selectivity in regard to their pristine counterparts, with MWCNTht yielding a conversion of 47 % and 74 % selectivity, and GFht presenting a conversion of 57 % and 85.% selectivity. Reusability experiments revealed no loss of catalytic activity up to three catalytic cycles. The

results obtained clearly indicate that the fine tuning of the carbon materials morphology and surface chemistry, concerning amount of defects and types and amounts of oxygen surface groups, respectively, is of most importance in pursuing the generation of metal-free carbocatalysts with superior performance and selectivity.

The results obtained in Chapter 3, reveal that MWCNT and GF were successfully doped with heteroatoms, namely N, P, B, and S, through a simple ball milling procedure followed by thermal treatment in an inert atmosphere. The carbon materials characterization through XPS showed that: the nitrogen doping proceeded through the introduction of pyrrolic, pyridinic and quaternary N atoms on the graphitic structure; phosphorous atoms are bound to graphitic carbon in the prepared P-doped materials through R-O-$PO(OH)_2$ functionalities; B-doped materials showed the presence of boronic groups (C-BO_2) and B atoms in B_2O_3; and sulphur atoms found in S-doped materials were mainly tiophene-S type, while having a small percentage of S atoms in thiol groups. TEM observations revealed some loss of the nanotubes structural integrity in material MWCNT_N8, probably due to breaking of the nanotubes during the milling process, and observation of materials GF and GF_S6 did not show any apparent significant structural changes in the doped material, as it was possible to observe large wrinkled few-layer graphene sheet domains coexisting with smaller crystallites in both materials. Textural characterization revealed that the doping procedures increased the carbon nanotubes specific surface areas, due to a higher access to the nanotubes inner cavities, achieved through the breaking of the tubular structures. The doped graphene flakes presented an overall decrease in S_{BET}, probably due to a higher degree of agglomeration within the doped graphene flake crystallites, induced by the ball milling procedures, which was confirmed through XRD analysis. Notable exceptions to these trends were materials MWCNT_N6 and GF_N6, which showed an anomalous decrease in S_{BET}, indicating that the thermal treatment at 600 ˚C was not effective in the removal of the residues originated from the decomposition of the ball milled melamine. Raman spectroscopy revealed that the doping procedures promoted the reduction of the overall amount of disorder in the carbon nanotube materials, whereas for all the doped graphene flake materials, the amount of disorder increased with the doping treatments.

The catalytic studies showed that all the doped carbon materials were active catalysts in reduction of 4-NP in the presence of $NaBH_4$, and that the modifications introduced by doping the carbon nanotubes and graphene flakes with heteroatoms, overall yielded catalysts with superior activity in regard to their pristine counterparts, with material MWCNT_B10 reaching 80 % conversion after 7 minutes. The only exceptions were P-doped MWCNT and GF_N6, which present inferior catalytic activity.

Reusability experiments revealed no loss of catalytic activity up to three catalytic cycles for the doped carbon nanotubes, whereas the graphene flake materials showed some deterioration of catalytic performance due to ineffective washing between catalytic cycles. These results indicate that the doping of the carbon materials with heteroatoms (N, P, B and S), is a convenient and facile way to obtain metal-free carbocatalysts with superior performance in the reduction of 4-NP.

Within the perovskite solar cells framework, Chapter 4 presents the results obtained from the preparation of pristine and GF-doped mesoscopic mixed halide perosvkite based solar cells. Pristine devices were successfully prepared and characterized, yielding stable and reproducible pristine devices with an average 4.88 % PCE. The *I-V* measurements were found to be appropriate, as they can all have a significant impact upon the apparent power-to-current efficiency (PCE), and were used as a benchmark for the doped devices. Doped solar cells were prepared with GF in the ETL through the integration of graphene flakes in the mesoporous TiO_2 layer (method A), and TEM observations showed large graphene flake agglomerates at the surface of the mesoporous layer, partially or completely covered with TiO_2 nanoparticles. The doping of the ETL through method A severely affected the solar cells performance, resulting in devices with efficiencies below 1 %, which was attributed to extensive exciton quenching promoted by GF within the mesoporous TiO_2 layer, as indicated by the large decrease in the shunt resistance, which parallels the increase in GF amount, promoted by the large agglomerates of GF, and/or to the high number of layers of the GF crystallites, as confirmed by TEM, N_2 adsorption-desorption, and XRD. Devices doped with GF in the ETL, specifically in the perovskite/TiO_2 interface were prepared - method B - and TEM observations revealed the existence of several micrometers sized graphene flake agglomerates, settled at the surface of the mesoporous TiO_2. The doping procedure resulted in an overall inferior PCE. The occurrence of hysteresis in the I-V plots of the doped devices was observed, and its intensity increased with the amount of GF doping. The presence of hysteresis is due to changes in charge carrier extraction efficiency at the carrier-selective contact, introduced by GF doping. The device with HTL doped with GF showed a relatively uniform surface with small protrusions of GF, showing that the graphene flakes were almost completely surrounded by the HTL. The doped device showed a strongly decreased PCE, with an efficiency of 0.89 %. This decrease was attributed to the overextension of the oxidized state of spiro-OMeTAD caused by the presence of GF, leading to a detrimental effect on its hole transport ability and subsequent loss of the device efficiency. Stability studies of the pristine solar cells were carried out, regarding the aging of the devices in a dry and dark environment, during 100 days. An increase from 4.88 to 6.89 % PCE

was observed after 100 days of desiccant exposure in the dark, which may be due to the absorption of residual solvent molecules, enhancing the settling of the spiro-OMeTAD layer, and crystallization of the perovskite layer.

5.2 Future perspectives

The results obtained in this thesis provide new insights on the modification of carbon materials through surface oxidation and heteroatom doping, and their respective effect on their catalytic performance in selective oxidation and reduction reactions. The results are encouraging to further study the catalytic performance of the prepared materials with different oxidation substrates and catalytic systems. Furthermore, different oxididants and procedures should be involved in the preparation of new modified carbon nanotubes and graphene flakes, in order to promote a more extensive oxidation, which could them be tuned with appropriate subsequent thermal treatments, and foster the preperation of optimized carbocatalysts for oxidation reactions.

Regarding the carbon materials heteroatom doping, the results obtained encourage the use of the prepared materials in different catalytic systems, and the experimentation different heteroatom precursors for ball-milling procedures and optimized experimental conditions for the preparation of materials with more extensive heteroatom doping, which could then be tested, not only in the 4-NP reduction reaction, but also in other catalytic reduction or even oxidation reactions.

In the perovskite solar cells framework, the results obtained have shown that the strategies employed in this thesis did not enhance the devices efficiency. However, the realized work paves the way to the systematic study of the effect of carbon doping in perovskite based solar cells, and the exploration of different doping strategies and device architectures. The use of new carbon nanomaterials with appropriate properties (such as graphene quantum dots), as dopants in these remarkable systems can thus be explored.

Appendices

Appendix A

A1: Physico-chemical characterization of the heteroatom-doped carbocatalysts

X-ray photoelectron spectroscopy (XPS) was performed at ‘‘Centro de Materiais da Universidade do Porto’’ (CEMUP, Porto, Portugal) in a VG Scientific ESCALAB 200A spectrometer using non-monochromatised Al K_α radiation (1486.6 eV). The powdered samples were pressed into pellets prior to the XPS studies. To correct possible deviations caused by electric charge of the samples, the C1s band at 284.6 eV was taken as internal standard.[1,2] The XPS spectra were deconvoluted with the XPSPEAK 4.1 software, using non-linear least squares fitting routine after a Shirley-type background subtraction. The surface atomic percentages were calculated from the corresponding peak areas and using the sensitivity factors provided by the manufacturer.

Transmission electron microscopy (TEM) images were collected at “Universidade de Trás-os-Montes e Alto Douro”, with a Zeiss LEO 906 microscope operating at an accelerating voltage of 120 kV. The samples were dispersed in dimethylformamide under sonication, after which a carbon-coated 400 mesh copper grid was immersed in the suspension and then air-dried.

Textural characterization of the samples was carried out by N_2 adsorption–desorption at -196 ˚C in a Quantachrome NOVA 4200e apparatus. The apparent surface area (S_{BET}) was determined by applying the Brunauer–Emmett–Teller (BET) equation.[3]

X-ray diffraction (XRD) profiles were collected at room temperature in a continuous scanning mode (step 0.02 and time 10 s) on a Rigaku D/Max-B, Cu K diffractometer in the 2θ range from 7˚ to 100˚, in a Bragg-Brentano $\theta/2\theta$ configuration. A Lorentzian deconvolution of the (002) peak observed in the carbon material XRD profiles was performed and the crystallite sizes were estimated from the Scherrer equation [$L = 0.94 \times \lambda / (\beta_{1/2} \times \cos\theta)$], where L = average crystallite size, $\beta_{1/2}$ = line broadening at FWHM in radians, θ = Bragg angle and λ = X-ray wavelength (1.544 Å), and considering the interlayer distances. The area ratio was considered to measure the percentage of layers that are stacked as crystallites composed by the corresponding number of layers and although layers with interlayer spacings larger than 3.44 Å (2θ lower than 26.1º) are non 3-D stacked, they were considered only to estimate the weighted average number of layers in the materials and should not be regarded as crystallites.

The Raman spectra were measured directly on the materials using a Labram Dilor–Jobin-Yvon–Spex spectrometer, with the monochromatic green light at 532 nm of the Nd:YAG laser as the excitation source, at a power of 25 mW. Once the D band is a resonant mode and exhibits dispersive behavior, both its position and shape can vary with different excitation laser frequencies. Therefore, the excitation laser frequency was maintained for all measurements. A density filter was used to avoid thermal decomposition of samples by the laser. The ×50 objective lens of an Olympus optical microscope was used to focus the laser beam on the sample and to collect the scattered radiation. A highly sensitive CCD camera was used to collect the Raman spectra. Each Raman spectrum presented in this study corresponds to the accumulation of 10 spectra recorded from 1000 to 3400 cm^{-1} over 10 s.

References

[1] J. F. Moulder, W. F. Stickle, P. E. Sobol, K. D. Bomben, *Handbook of X-Ray Photoelectron Spectroscopy*, Perkin-Elmer, **1992**.

[2] Y. Xie, P. M. A. Sherwood, *Chem. Mater.* **1990**, *2*, 293–299.

[3] S. Brunauer, P. H. Emmett, E. Teller, *J. Am. Chem. Soc.* **1938**, *60*, 309–319.

Appendix B

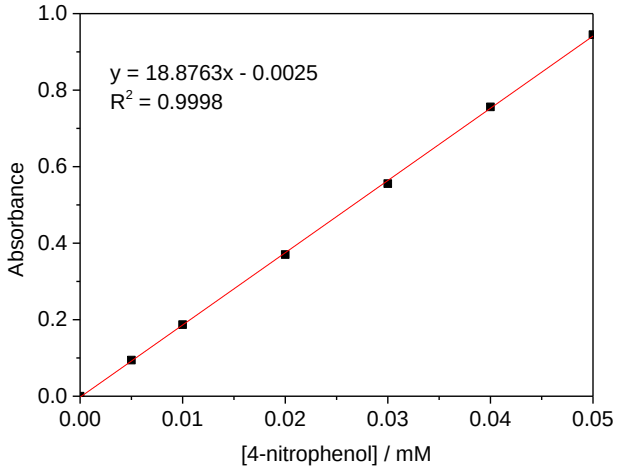

Figure B.1 Calibration curve of 4-NP.

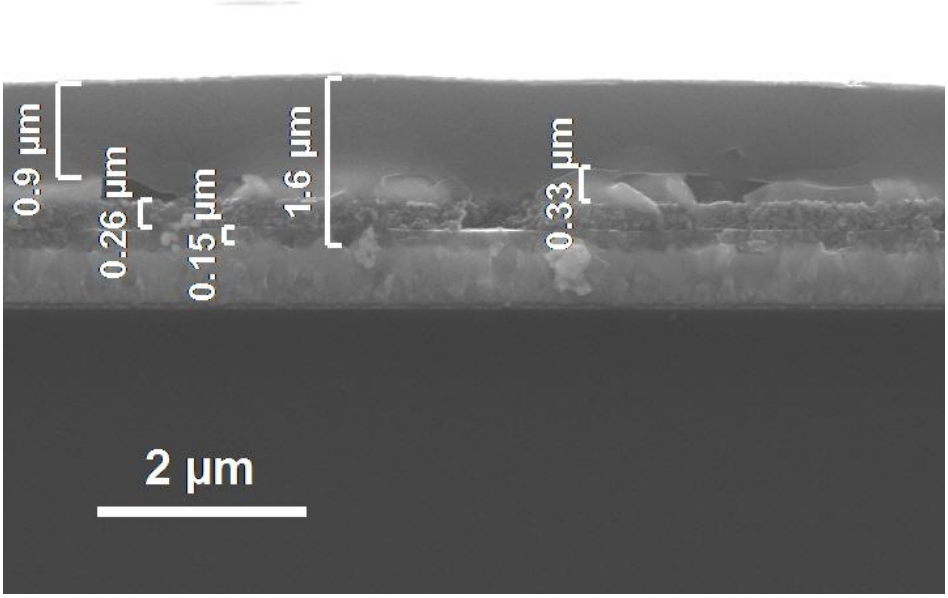

Figure B.2 SEM micrograph of solar cell SC_P2 (cross-section), with measurements.


U.PORTO
FACULDADE DE CIÊNCIAS
UNIVERSIDADE DO PORTO